

**GEOSAT/ERM ALTIMETER DATA ANALYSIS FOR THE  
DETERMINATION OF GLOBAL OCEANIC  
MESOSCALE VARIABILITY**

**APPROVED BY  
SUPERVISORY COMMITTEE:**

*B D Tapley*

---

B.D. Tapley

*B E Schutz*

---

B.E. Schutz

*CK Shum*

---

C.K. Shum

*Daniel T. Sandwell*

---

D.T. Sandwell

*Gary Wise*

---

G.L. Wise

**GEOSAT ALTIMETER DATA ANALYSIS FOR THE  
DETERMINATION OF GLOBAL OCEANIC  
MESOSCALE VARIABILITY**

**by**

**Bohai Zhang**

**DISSERTATION**

**Presented to the Faculty of the Graduate School of**

**The University of Texas at Austin**

**in Partial Fulfillment**

**of the Requirements**

**for the Degree of**

**Doctor of Philosophy**

**THE UNIVERSITY OF TEXAS AT AUSTIN**

**December 1988**

## ACKNOWLEDGMENTS

I am grateful to my supervisor Dr. Byron D. Tapley for his guidance, encouragement and full support through out the entire study and for his effort in reviewing this work. My special thanks must also go to Dr. David.T Sandwell and Dr. C.K. Shum. Their valuable scientific insights, comments and suggestions are greatly appreciated. Without their support, I would never have learned enough to complete this research. I would like to thank other members of my committee: Dr. Bob E. Schutz and Dr. Gary L. Wise for their interest in my work. My thanks are also extended to my colleagues and friends John C. Ries, Dahning Yuan and Cheng Huang for their helpful discussions, and to Steve Nerem for his assistance in producing the color graphics.

I am deeply indebted to my parents Mrs. Hu Xiaofeng and Mr. Zhang Jingfu for their encouragement and support. Finally, I wish to thank my wife Yaqun and my daughter Wanlin. All this would have been impossible without their love and understanding through out the five years of my graduate study.

December, 1988

Austin, Texas

U.S.A.

**GEOSAT ALTIMETER DATA ANALYSIS FOR THE  
DETERMINATION OF GLOBAL OCEANIC  
MESOSCALE VARIABILITY**

Bohai Zhang, Ph. D

The University of Texas at Austin, 1988

Supervising Professor: Byron D. Tapley

**ABSTRACT**

Obtaining a basic description of the global mesoscale variability is fundamental to an improved understanding of ocean dynamics. Satellite altimetry which measures the distance between the spacecraft and the sea surface is becoming an important tool for acquiring global, synoptic measurements of the dynamic topography of the oceans. The radial orbit error for the satellite has been the major limitation to the application of satellite altimetry oceanographic studies. The goal of this research is to develop methods for reducing radial orbit error and to apply these methods to study oceanic mesoscale variability using Geosat altimeter data.

The conventional crossing arc technique has been widely applied to satellite geodesy and oceanography. An efficient and generalized method has been developed for the computation of altimeter crossover measurements which is applicable to both single and dual satellites. Evaluations of the radial orbit error show that the operational Geosat Exact Repeat Mission (ERM) orbits have 3~4 m crossover rms residuals and the predominating radial orbit error occurs at the frequency of once per revolution (40,000



km wavelength).

As a result from the orbit error analysis, a new technique has been developed for extracting global mesoscale variability from collinear satellite altimeter profiles which have large radial orbit error. Long wavelength radial orbit error is suppressed by taking the derivative of each altimeter profile. The resulting mean sea surface slope profile, averaged from 22 repeat slope profiles, has a precision about 0.1 microradians ( $\mu\text{rad}$ ). Slopes due to mesoscale dynamic topography are typically 1  $\mu\text{rad}$ . Root mean square slope variability as low as 0.2  $\mu\text{rad}$  are found in the Southeast Pacific and maximum slope variations up to 6-8  $\mu\text{rad}$  are found in major western boundary currents (e.g. Gulf Stream, Kuroshio, Falkland and Agulhas) and in the Antarctic Circumpolar Current (ACC) systems.

The global rms variability map shows previously unknown spatial details that are highly correlated with sea floor topography. At mid-latitudes, the variability is generally high in deep water ( $> 3000$  m) and low in shallow water ( $< 3000$  m). Eddy kinetic energy associated with the Gulf Stream and Kuroshio Current is also examined. Good agreement with previous altimeter results is obtained in both magnitude and spatial distribution.

## TABLE OF CONTESTS

Acknowledgments		iii
Abstract		iv
Chapter 1	Introduction	1
1.1	Observing the Ocean from Space	1
1.2	Geosat Exact Repeat Mission (ERM)	4
1.3	Geometry of Satellite Altimeter Measurements	8
1.4	Geosat Radar Altimeter	13
1.5	Study Objectives	17
Chapter 2	Altimeter Crossover Methods for Satellite Oceanography	19
2.1	Introduction	19
2.2	Crossover Measurement Geometry	22
2.3	Crossover Measurement Computation	26
2.4	Gravity Solution Methodology Using Altimeter Crossovers	29
2.5	Sensitivity of Geopotential Coefficients Using Crossover Data	34
2.6	Orbit Determination Experiments Using Altimeter Crossover Data	38
2.7	Summary	40
Chapter 3	Precision Orbit Determination for Geosat ERM	44
3.1	Introduction	44
3.2	A General Statement of the Orbit Determination Problem	45
3.3	Dynamical Equations of Motion and Force Models	46

3.4	The Doppler Observation	49
3.5	Orbit Determination Process	51
3.6	Tranet Tracking System for Geosat ERM	54
3.7	Orbit Determination	60
3.8	Geosat ERM Ephemerides Evaluation	62
3.9	Summary	66
Chapter 4	Global Mesoscale Variability From Geosat ERM	77
4.1	Introduction	77
4.2	Data Processing and Analysis	83
4.2.1	Pre-processing	83
4.2.2	Orbit Error Analysis	84
4.2.3	Averaging, Differencing and Filtering	88
4.3	Slope Variability	90
4.3.1	Slope Difference Profiles	90
4.3.2	RMS Slope Variability	94
4.3.3	Correlation of Variability with 3000 m Depth	96
4.3.4	Variability Due to Tide Model Error	99
4.4	Summary	100
Chapter 5	Eddy Kinetic Energy	119
5.1	Introduction	119
5.2	Theoretical Basis	119
5.3	Eddy Kinetic Energy for the Northwest Atlantic and the	

	Northwest Pacific	126
5.4	Comparisons With Geos-3, Seasat and Shipboard Results	128
5.5	Summary	129
Chapter 6	Conclusions	135
	Appendix	138
	Bibliography	144

# Chapter 1

## Introduction

### 1.1 Observing the Ocean From Space

The structure of the ocean surface topography consists of two components: the marine geoid and the dynamic topography. The larger of the two components (the marine geoid) is an equipotential surface of the Earth's gravity field. Undulations in the geoid reflect variations in the density structure of the solid Earth. At the shortest wavelengths, the topography of the sea surface mimics the topography of the sea floor. Superimposed on these larger geoid undulations are smaller variations in sea surface topography caused by ocean tides, ocean currents, eddies and other meteorologically related phenomena. The dynamic ocean topography consists of a quasi-stationary component associated with seasonal and long term current movement and a component associated with shorter time scale fluctuations.

Ocean currents, in association with the influence of the atmosphere, move the Earth's heat from one latitude to another, delivering warm water to the colder climates and cold water from the polar regions to the warm equatorial regions. They moderate temperature and weather fluctuations on the continent and ultimately determine their climates.

Observing the large scale ocean circulations and studying ocean dynamics have been the primary interest of physical oceanographers for the past century. However, over the last ten years, oceanographers have realized the importance of fluctuating currents in ocean dynamics. Thus, much of their attention has been shifted from the

study of mean motion of the current to the variability of the current. This shift in emphasis has resulted from studies [e.g. Wyrski, 1976] showing that fluctuating currents contain far more kinetic energy than does the mean motion (Figure 1.1). Recent variability studies have classified wavelike and turbulent motions, assessed their role in ocean dynamics, estimated the importance of the various instabilities of the mean motion of the currents, and calculated the interactions among wave fields of the major currents [Stewart, 1985].

As storms are important to meteorologists, eddies are important to physical oceanographers. Eddies transport energy on a local scale, contribute to the large currents, and move the bulk of the Earth's absorbed energy. Understanding and parameterizing these motions requires repeated observations of large areas of the ocean under many different conditions, with spatial resolution on order of tens of kilometers.

For centuries, oceanography has depended on sparse measurements which were made from surveying ships or were collected from tide gauges. However, because of the vastness and inaccessibility of the oceans, the current shipboard data sets are insufficient for the development of detailed models of the oceans and for the understanding of oceanic dynamics. Since the launch of Geos-3 satellite in 1975, satellite-borne radar altimetry has promised nearly total coverage of the world oceans with the ability to resample the surface at periods of a few weeks. The combination of satellite altimetry and wind measurements, made from satellite scatterometer together with *in situ* measurements, can significantly enhance our ability to observe the oceans globally and synoptically.

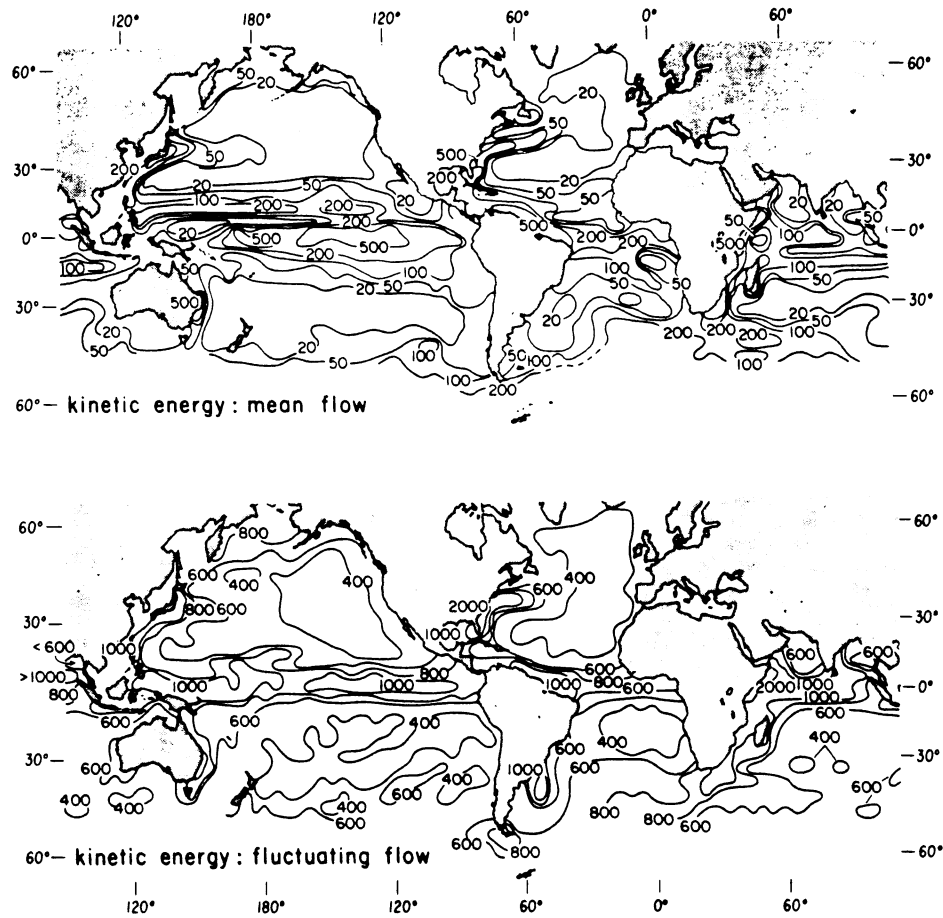


Figure 1.1 Kinetic energy of sea surface currents averaged over 5° squares. Upper: kinetic energy of the mean flow. Lower: kinetic energy of fluctuating currents (from Wyrki, 1976).

## 1.2 Geosat Exact Repeat Mission (ERM)

Experience with Geos-3 and Seasat during the 1970's has demonstrated the enormous potential of satellite altimetry, but neither mission provided a data set that was both long term and global in coverage. On March 12, 1985, the United States Navy altimetric satellite, Geosat, was launched into an orbit of 800 km altitude and 108° inclination and began generating a new data set with unprecedented spatial and temporal coverage of the global oceans [Cheney et al., 1987]. The primary purpose of the satellite mission was the improvement of the marine gravity field. Data collected from the first 18 months during the primary (geodetic) mission are classified. However, the geodetic mission ended on September 30, 1986 and on October 1 the Geosat was maneuvered into an orbit in which the ground track repeats itself within 1 km after 17 days (244 revolutions). This orbit produces altimeter data within 10 km of the ground track for the previously released Seasat data, and the mission is now referred to as the Geosat Exact Repeat Mission (ERM). The ERM officially became operational on November 8, 1986. Maneuvers are performed approximately once per month to maintain the collinearity of the ground track to within  $\pm 500$  m. The ground track spacing at the equator is about 160 km (Figure 1.2), so an excellent sample of the oceans can be obtained. Since the ground track for the ERM is very close to the Seasat orbit which has released altimeter data, the new data set is unclassified. Under agreement with the U.S. Navy, National Oceanic and Atmospheric Administration (NOAA)/National Ocean Service is producing the ERM Geophysical Data Records (GDR) which have been distributed through NOAA's National Oceanographic Data Center (NODC) [Cheney et al., 1987]. So far the satellite is performing well, and the ERM will possibly continue into the early 1990s.



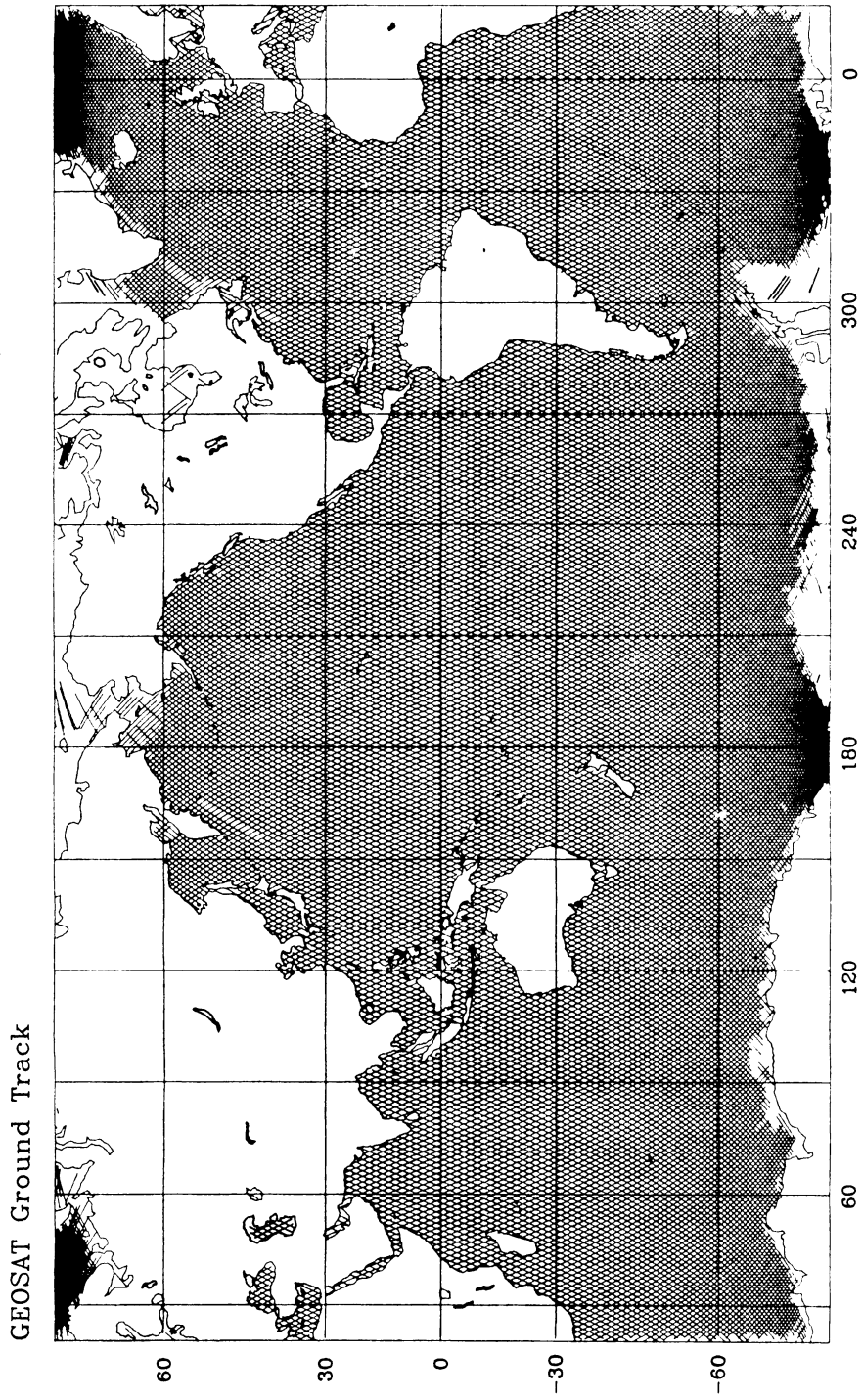


Figure 1.2 Geosat ERM Ground Track

Geosat ERM orbit characteristics are listed in Table 1.1. The ground track pattern of Geosat repeats after 244 revolutions which is approximately 17.05 days. A frozen orbit, in which the eccentricity and argument of periapsis change due to the geopotential are nearly eliminated, was selected to maintain a constant altitude history and to eliminate lateral variations in ground tracks associated with an eccentric orbit having a circulating line of apsides [Born et al., 1987]. Maneuvers have been performed at a frequency of no more than once per month to maintain the frozen orbit. A frozen orbit was also used on the Seasat mission.

Table 1.1 GEOSAT ERM Orbit Parameters

---

Semimajor Axis = 7162.6 km

Eccentricity = 0.0008

Inclination =  $108^\circ$

Longitude(East) of Node =  $1.05^\circ + n * 1.475^\circ$

where  $n = 0$  to 244 (orbit revolution number)

Periapsis Altitude = 778.7 km

Period = 6035.6 seconds (1.68 hours)

Node Rate =  $2.0^\circ/\text{day}$

Perigee Rate =  $-1.7^\circ/\text{day}$

---

The configuration of the Geosat spacecraft is shown in Figure 1.3. The long boom is used for radially decreasing the gravity gradient of the Earth to keep the spacecraft oriented in the nadir direction. The spacecraft has two redundant doppler beacons which also point in the nadir direction. Each beacon generates two coherent

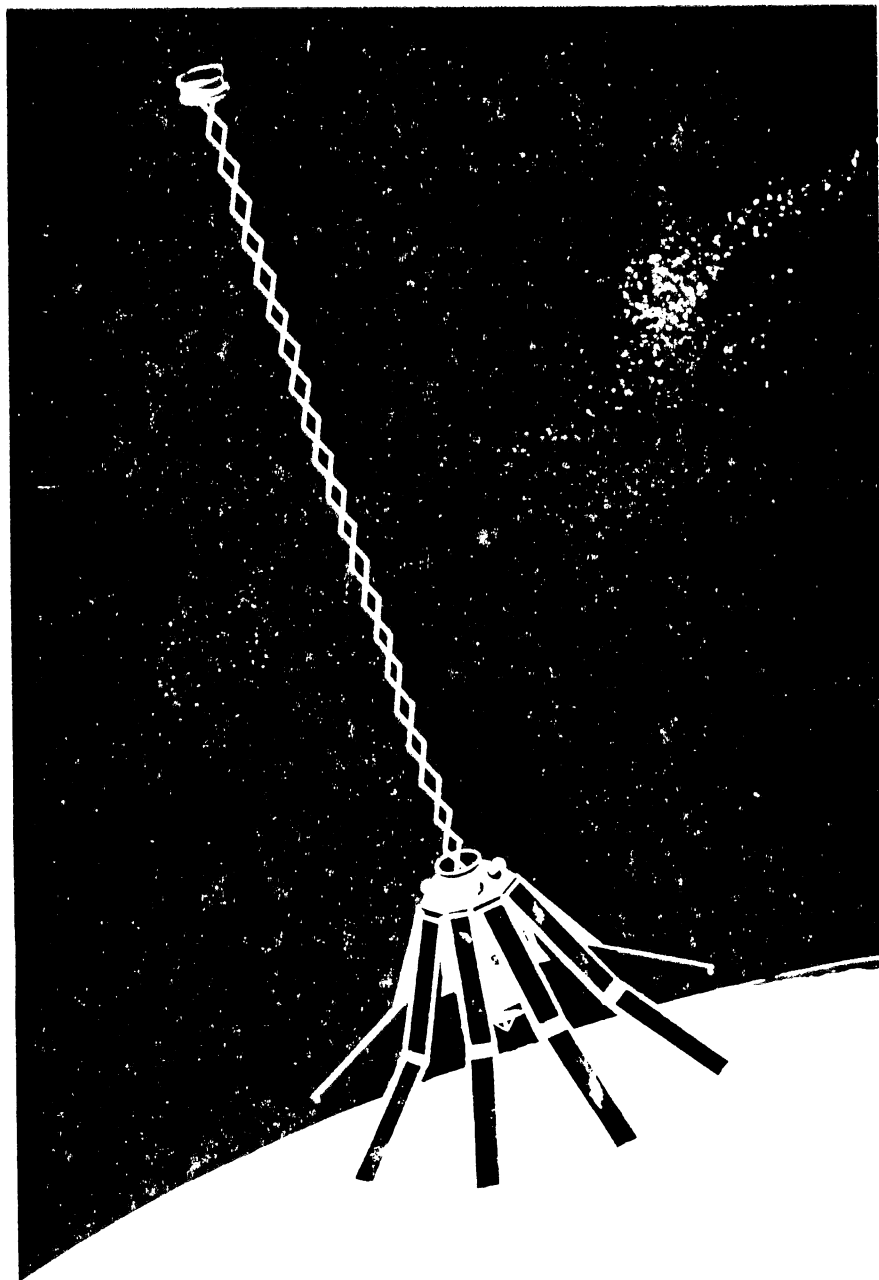


Figure 1.3 Geosat Spacecraft Configuration (from Cheney et al., 1987)

frequencies, 150 MHz and 400 MHz, that are continually broadcasting. Two frequencies are used to remove the first order ionospheric refraction effect. The Geosat transmitted frequencies are biased above the nominal frequency by 80 parts per million to help distinguish them from the Navy's Transit satellites which are also tracked by the Navy's Tranet tracking system and which broadcast at 150 MHz and 400 MHz less 80 parts per million. To date only one beacon on Geosat has been used.

In this study, the first twenty-two repeat cycles, from November 1986 to November 1987, of Geosat/ERM altimeter data were used for the determination of global oceanic mesoscale variability.

### 1.3 Geometry of Satellite Altimeter Measurements

The satellite altimeter transmits radar pulses towards the ocean. The round trip travel time  $\Delta t$  of the electromagnetic pulse transmitted from the satellite and reflected off the ocean surface back to the altimeter antenna can be converted to a height by the relation:

$$h = c \Delta t / 2 \quad (1.1)$$

where  $c$  is the speed of light and  $h$  is the radial distance from the altimeter antenna to the instantaneous ocean surface. This assumes no radial motion of the spacecraft in the period of  $\Delta t$ .

The in-orbit measurement precision of satellite altimeters have improved from the 1-meter precision accomplished by the Skylab mission to sub-decimeter precision realized by Geosat. The Geosat altimeter incorporates a number of design changes that

have resulted in improved measurement precision. Its in-orbit performance indicates a precision approaching 3 cm for moderate wave height (Figure 1.4, [McConathy, et al., 1987]).

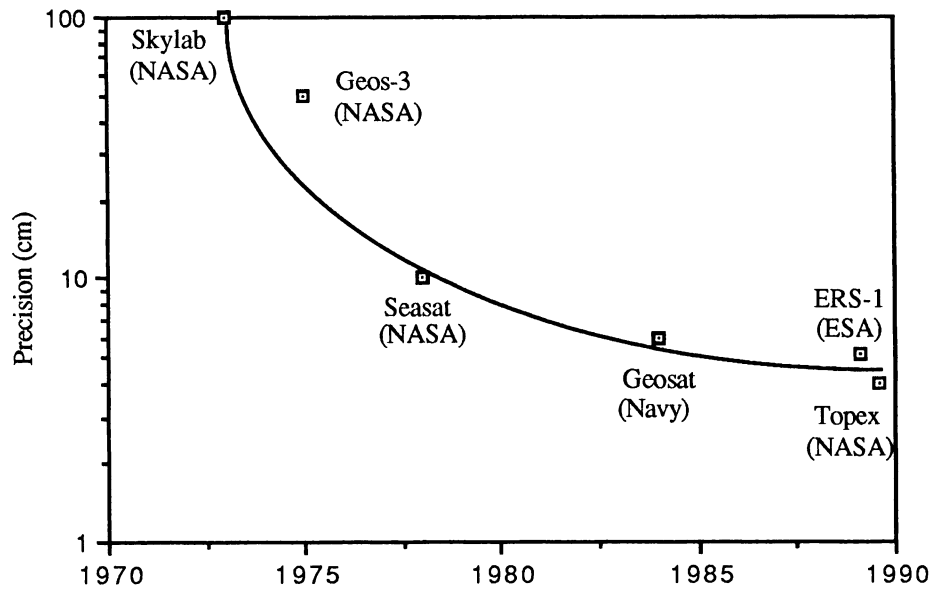


Figure 1.4 The evolution of satellite altimetry precision

Before an altimeter height model can be discussed, an understanding of the measurement geometry, as illustrated by Figure 1.5, and a brief review of some of the concepts and definitions is necessary.

#### Reference Ellipsoid:

The irregular surface of the Earth (continents and oceans) can not be represented by a simple mathematical relation. However, the Earth's surface may be closely approximated by a rotational ellipsoid with flattened poles [Torge, W., 1980]. The

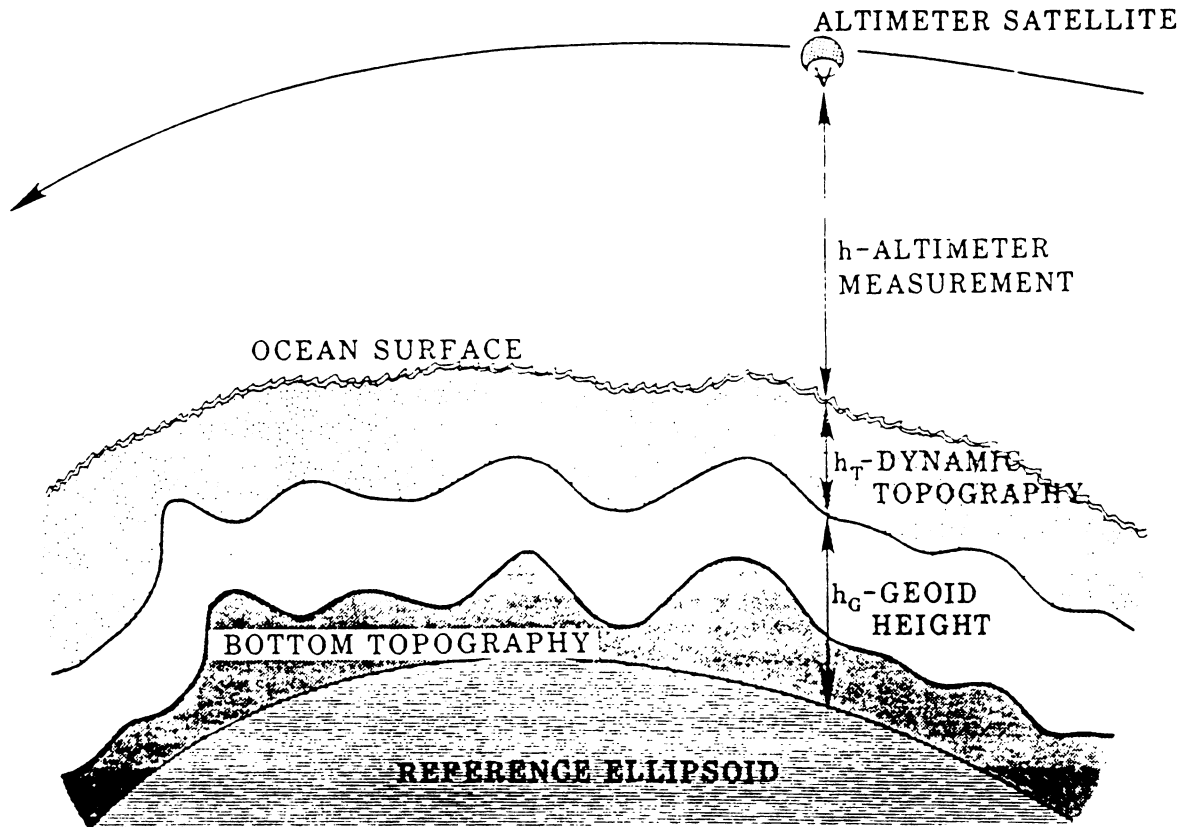


Figure 1.5 Geometry of Satellite Altimeter Measurements. The satellite's radar altimeter measures its altitude above the ocean surface. An accurate orbit is used to determine the height above the reference ellipsoid. The difference between the two heights is the sea surface topography which consists of geoid height (marine gravity variations) and dynamic topography due to geostrophic ocean currents. The geoid height mimics the sea floor topography.

shape of the ellipsoid is described by two geometric parameters; the semimajor axis,  $a$ , and the semiminor axis,  $b$ . Generally,  $b$  is replaced by the inverse of the geometrical flattening  $f$ , which is more suitable for series expansions. The reference ellipsoid used for in Geosat GDR's is defined by [Cheney et al. 1987] :

$$a = 6378137.0 \text{ m}$$

$$f = 1/298.257223563$$

where

$$f = \frac{a - b}{a} \tag{1.2}$$

#### Geoid and Sea Surface Topography :

The geoid is an equipotential surface that corresponds closely to the mean sea surface. The two surfaces differ primarily due to the effect of the tides and ocean currents. This difference is referred to as the Sea Surface Topography (SST), and it is related to the circulation of the ocean currents.

The potential which defines the geoid is:

$$W = W_g + W_a \tag{1.3}$$

where the  $W_g$  is the potential of the gravity due to the solid Earth and water plus the rotational potential of the Earth and  $W_a$  is the potential of gravity due to the Earth's atmosphere [Stewart, 1985].

The altimeter height measurement model presented by Tapley et al. [1982] is given by:

$$h_e = h_{al} + h_{sg} + h_i + h_a + h_s + h_g + h_t + h_o + \varepsilon \quad (1.4)$$

where

$h_e$  the distance from the satellite center of mass to the reference ellipsoid at the altimeter subsatellite point

$h_{al}$  the satellite height above the instantaneous ocean surface measured by the altimeter

$h_{sg}$  the effect of the spacecraft geometry, including the distance from the altimeter feed horn to the satellite center of mass and the effect of the spacecraft pointing in a nonvertical direction

$h_i$  the sum total of instrument delays

$h_a$  the sum of atmospheric path length corrections due to the troposphere (both wet and dry components), and the ionosphere

$h_s$  the correction due to surface and radar pulse interaction (EM bias)

$h_g$  the geoid height

$h_t$  the correction for solid Earth and ocean tides

$h_o$  the ocean surface topography due to ocean circulation phenomena

$\varepsilon$  random measurement noise

From the model described by Eq. (1.4), one can conclude that:

- Given the satellite position as determined from ground-based tracking data, the combined features of the ocean surface topography and the shape of the marine geoid can be inferred from the altimeter data;
- Inversely, given an accurate ocean surface model, altimeter data can be used to



improve radial orbit accuracy.

#### 1.4 Geosat Radar Altimeter

To simplify the discussion, it is assumed that the transmitter of a satellite altimeter sends out a short duration electromagnetic pulse towards the ocean. The pulse is reflected back to the satellite and a sensitive receiver records the return pulse. An accurate clock registers the time interval between transmission and reception. A height measurement then can be computed from Eq. (1.1) where the pulse travels at the speed of the light ( $\sim 3 \times 10^8$  m/sec). A measurement to an accuracy of 1 cm requires a timing accuracy of 30 picoseconds or stability in the clock of better than one part in  $10^8$ . While stringent, these accuracies are possible [Stewart, 1985].

In practice, the transmitter first generates a sharp pulse that is then sent through a dispersive filter to produce a long pulse that can carry more radio energy. After reception, the original sharp pulse shape can be recovered by passing through an inverse of the filter. A pulse-limited mode of operation is used for the Geosat altimeter [MacArthur et al., 1987]. A spherically expanding pulse of rectangular cross section striking a smooth surface at first illuminates a small spot which grows until the trailing edge of the pulse reaches the surface, during which time the scattered power increases linearly with time. Then the illuminated area becomes a spreading annulus of constant area, and the scattered power remains constant until the annulus reaches the edge of the antenna beam (Figure 1.6). The result is a waveform whose average shape is given by the double convolution of the system's point target response, the ocean surface height distribution, and the two-way antenna pattern (Figure 1.7). The sharply rising leading

edge of the waveform is the basis for the precise height estimation. The halfpower point conforms closely to mean sea level. The instrument tracks the location of that point with respect to the transmitted pulse, and the height measurement is stored on tape and finally telemetered to the ground. The diameter of the surface spot illuminated by the radar just before it becomes an annulus is given by [Stewart, 1985]:

$$d = 2\sqrt{hc\tau}$$

$$\tau^2 = \tau_p^2 + \frac{16H^2n^2}{c^2} \quad (1.5)$$

where  $h$  is the satellite height,  $c$  is the velocity of light,  $\tau_p$  is the pulse duration, and  $H$  is the standard deviation of wave height. For Geosat,  $h$  is 800 km and  $\tau$  is 3 ns, so  $d$  is 900 m for calm seas. If the surface is not smooth but is disturbed by waves, the reflected pulse is spread in time, scattering first from crests and then from troughs. This spread is measured by the radar and allows observations of significant wave height. The slope of the leading edge affects the measurement precision directly and degrades performance with increasing wave height. This is counteracted in part by adaptively increasing the width of the tracking gate that senses the location of the leading edge. The addition of adjacent high-resolution samples to form a wider gate leads to a reduction in noise.

As part of the overall height and wave-height estimation process, the amplitude of the ocean-return signal is normalized via an Automatic Gain Control (AGC) loop. The properly calibrated AGC setting is a measure of the backscatter coefficient at the surface that, in turn, is dependent on wind speed.

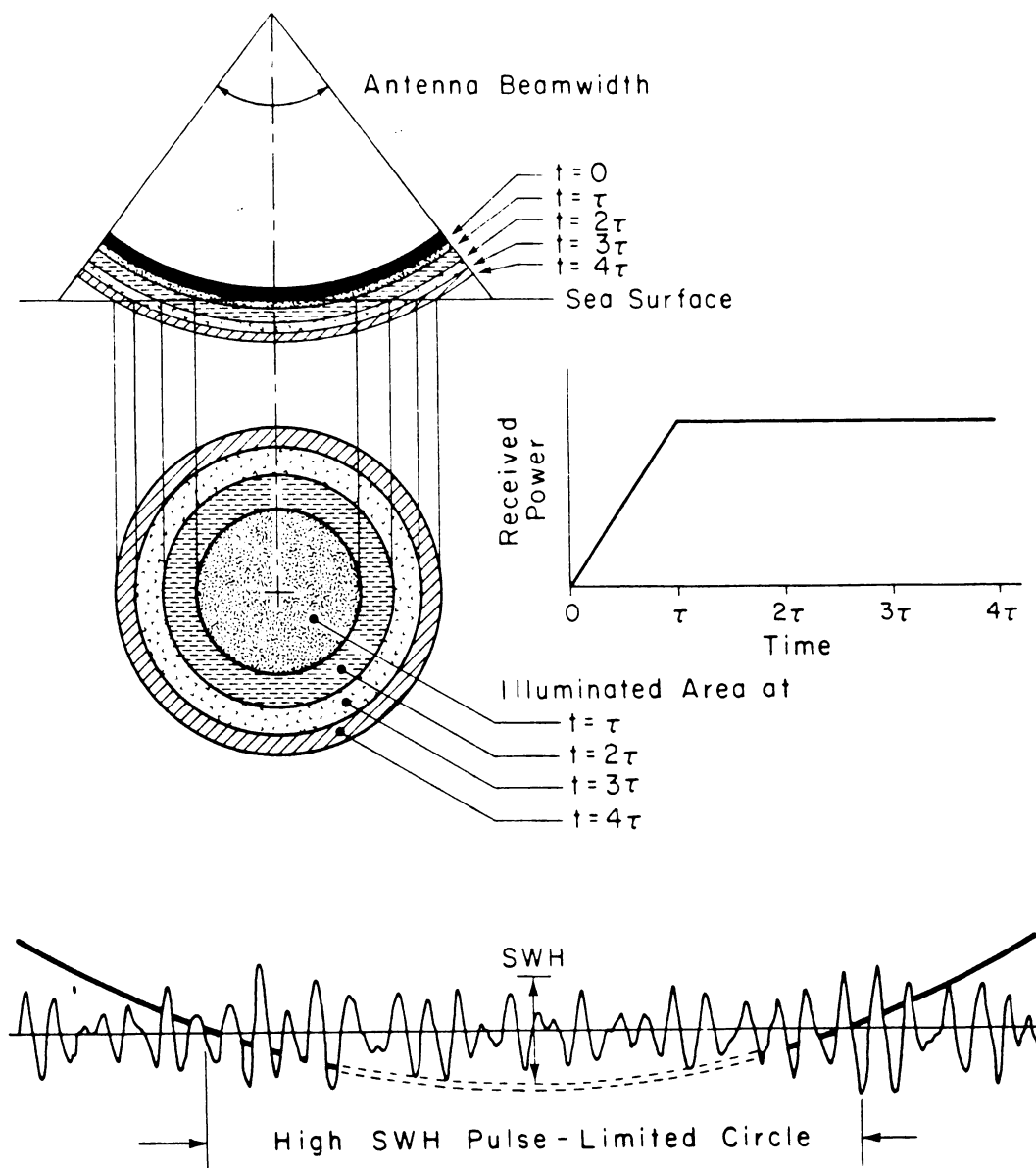


Figure 1.6 Pulse-Limited Geometry of Satellite Radar Altimeter. (from Stewart, 1985)

The length of the altimeter pulses plus the height of the waves on the sea surface determine the surface area observed by an altimeter. Two extremes are illustrated. The top and middle show a time sequence for a rectangular pulse incident on a sea surface whose wave height is very small compared with the pulse width. The Bottom shows a 3 ns pulse incident from an altitude of 840 km on a sea surface with 10 m waves and 300 m dominant wavelength (the vertical scale is magnified by a factor of 100)

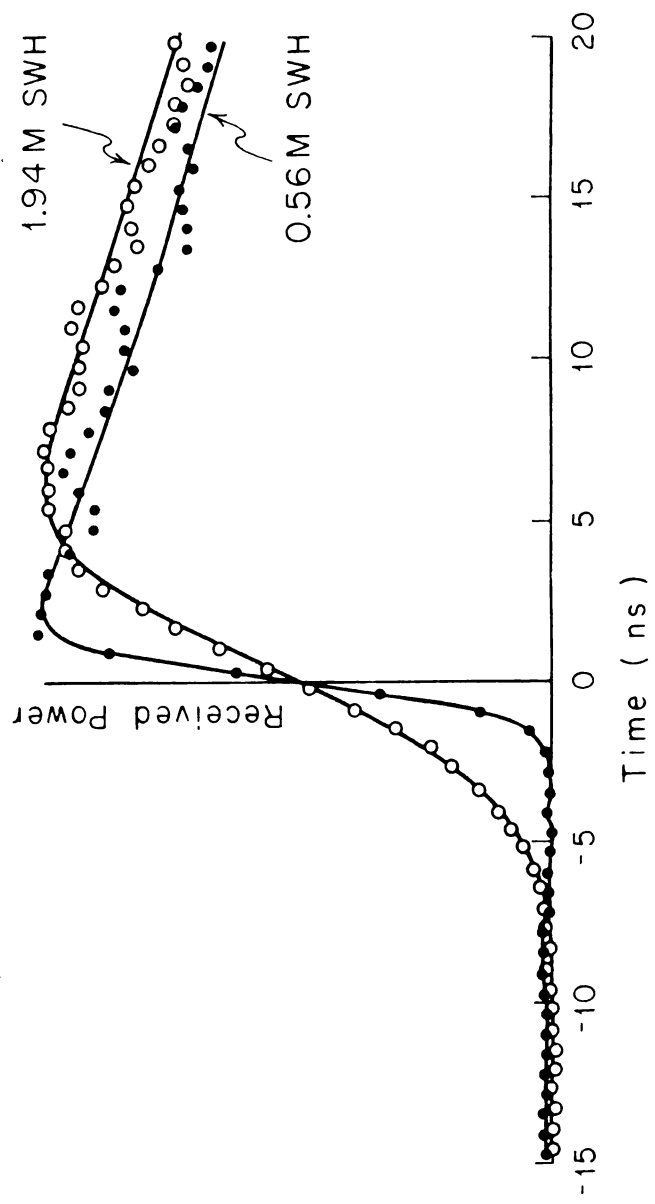


Figure 1.7 Waveform of Satellite Altimeter Signal (from Stewart, 1985)  
 In order to determine the arrival time of the altimeter pulses to within a fraction of a nanosecond, and to determine significant wave height (SWH), A smooth curve is fitted through the averaged shape of many altimeter pulses.

In summary, the Geosat radar altimeter is an improved version of the one flown on Seasat [MacArthur et al., 1987]. It provides three basic measurements with precision specified as follows:

Height: 3.5 centimeters for < 2 meters significant wave height (SWH);

SWH: 10% of the SWH or 0.5 meters (which ever is greater);

Wind speed: 1.8 m/s over the range 1 to 18 m/s.

### **1.5 Study Objectives**

The primary limitations on the accuracy of the ocean surface features that can be extracted with satellite altimetry are: (1) errors in the satellite orbit used to reduce the altimeter measurements to ocean surface heights above a reference ellipsoid, and (2) errors in the marine geoid, which is subtracted from the sea surface heights to obtain sea surface topography. The error in the model for the Earth's gravity field is the single largest contributor to both of these error sources. Single satellite crossing arc methods have been widely and successfully used to reduce the effects of these limitations [Shum, 1983]. A geometric technique using dual satellite altimeter crossovers to improve satellite radial orbit accuracy was proposed by Born et al. [1985]. In Chapter 2, a dynamic approach using dual satellite crossover data for the purpose of gravity model improvement and precision orbit determination has been developed. Also, an efficient and generalized computation system which is applicable to both single and dual satellite crossover measurements is developed. Finally, sensitivity of geopotential coefficients to the crossover data is investigated both analytically and numerically.

In order to use the Geosat altimeter data to the full extent of the instrument

precision, accurately determined Geosat ERM orbit using the best available gravity model and the Tranet doppler ground tracking data is desirable for the analysis of Geosat ERM altimeter data. The precision orbit determination procedure and orbit evaluation for Geosat ERM are presented in Chapter 3.

Geosat is the only orbiting altimetric satellite in the 1980s. It has produced valuable new data and will provide years of observations, bridging the Geos-3/Seasat and the Topex/ERS-1 eras. Its high quality ( $< 5$  cm) measurements and its excellent spatial and temporal coverage provide a unique opportunity to study the detailed and long-term geophysical and oceanographical phenomena globally and synoptically. The primary objective of this investigation is the analysis of Geosat ERM altimeter data for the determination of global oceanic mesoscale (100 ~ 1000 km) variability. A new method for extracting global mesoscale variability from collinear altimeter profiles which have large radial orbit error ( $\sim 4$  m) has been developed. Long-wavelength orbit error, as well as other long-wavelength errors were suppressed by a simple derivative filtering process. A global rms variability map was constructed which shows many previously unknown spatial details. Techniques employed for this study and results associated with oceanographic features are presented in Chapter 4.

In Chapter 5, eddy kinetic energy associated with the Gulf Stream and Kuroshio Current is examined and compared with previous altimetric results. A summary of this study is given in Chapter 6.

## Chapter 2

### Altimeter Crossover Methods for Satellite Oceanography

#### 2.1 Introduction

The ability of satellite-borne radar altimeter data to measure the global ocean surface with a few centimeter precision provides a unique data set for precision orbit determination, mapping the marine geoid and determining ocean dynamic topography [Shum, 1983]. Although satellite altimetry has a distinct advantage in its global distribution of data, consideration of possible error sources when altimeter data are used directly for orbit determination and geophysical mapping suggests several disadvantages. In particular, long wavelength oceanographic features and nontemporal ocean topography can be absorbed into orbit and geodetic parameters when altimeter data are used directly. The nontemporal ocean topography, mostly due to error in the marine geoid, currently has uncertainty at meter level and is significant when decimeter radial orbit accuracy of certain satellite orbits is desired.

A technique which eliminates the altimeter's dependence on the nontemporal ocean topography is based on the use of altimeter measurements at the points where the orbit ground tracks intersect. These points are referred to as "crossover points". A crossover measurement is defined as the difference in the altimeter measurements at the points where satellite ground tracks intersect. Since the constant part of each altimeter measurement will be due to the marine geoid and the quasi-stationary sea surface topography, the crossover or differenced altimeter measurements will be a function of the radial orbit error, the atmospheric refraction effects and the time-varying ocean

surface topography (e.g. tides and current variations). The radial orbit errors are primarily caused by mismodeling the forces which act on the satellite. The orbit error is primarily a long wavelength feature with dominant once per orbital revolution (40,000 km) and twice per orbital revolution (20,000 km) components.

Global analysis of crossover residuals can provide valuable information about radial orbit error sources. Altimeter crossover measurements have been used to evaluate the accuracy of Seasat ephemerides [Shum, 1983, Schutz et al., 1985]. Crossover residuals have also been useful for validation and estimation of the Seasat time tag accuracy [Marsh et al., 1982; Schutz et al., 1982]. Hagar and Boggs [1977] and Shum [1983] investigated the observability characteristics of single satellite crossover measurements in their application to orbit determination.

Crossover methods are also useful in recovery of geoid undulations and gravity anomalies [Rummel et al., 1977, Rapp, 1983] as well as ocean tide constituents [Parke, 1980; Brown, 1983]. Dynamic techniques, using altimeter and altimeter crossover data, have been applied to obtain the solution of a Seasat-tailored gravity field [Shum, 1983; Schutz et al., 1985]. More recently, the University of Texas has developed preliminary gravity field solutions for Topex mission which included altimeter and altimeter crossover data [Tapley et al., 1987, 1988a]. Geosat radial orbit accuracy has been improved significantly using these recent gravity fields.

Geometric techniques to remove orbit error using crossover measurements have been applied to the generation of maps of global mean sea surface [Marsh et al., 1982; Marsh et al., 1986]. By taking the difference from global crossover adjusted Seasat altimetric mean sea surface from geoid models, Tai and Wunch [1983] using GEM-9, and Engelis [1983] using GEM-L1 obtained interesting and even reasonable global sea



surface dynamic topography maps.

Time series of the sea level changes which revealed the seasonal variability of the Gulf Stream utilizing crossover techniques have been generated by Fu et al. [1987] using Seasat altimeter data. Moreover, sea level time series over a large region of the Equatorial Pacific showing the propagation of a Kelvin wave associated with the 1986-1987 El Nino were obtained from the crossover analysis of Geosat altimeter data [Cheney et al., 1986; Miller et al., 1987].

Santee [1985] and Born et al. [1985] performed a study to use geometrical techniques to improve the orbit of the proposed Navy satellite, N-ROSS, with the use of dual satellite altimeter crossover data between N-ROSS and the proposed Topex/Poseidon satellite. Shum et al. [1986, 1987] examined the observability of geopotential coefficients using dual satellite crossover data in the orbit determination procedure.

The Topex/Poseidon mission, which will be conducted jointly by the National Aeronautics and Space Administration (NASA) and France's Centre Nationale d'Etudes Spatiale (CNES), will carry high precision radar altimeter instruments in an attempt to measure oceanic topography including the mean and variable sea surface geostrophic currents and tides of the world's oceans, and to lay the foundation for a continuing program to provide long-term observations of the ocean's circulation and its variability. In the same time span, the European Space Agency (ESA) will launch another altimeter satellite, ERS-1. Since ERS-1 will cover most of the ocean surface with its 98° inclination and the Topex/Poseidon mission will provide a more accurate radial orbit (~13 cm rms) [Stewart et al., 1986], the use of crossover measurements between these

satellites will provide a significant means for precise orbit determination and the mapping of geophysical and oceanographic phenomena.

This chapter describes the techniques used to apply single and dual satellite crossover data for the purpose of precision orbit determination and the reduction of geophysical parameters. Sensitivity of geopotential coefficients to the altimeter crossover data is examined, and the contribution of crossover data to the solution of the Earth's gravity field is studied. Also, an efficient and generalized crossover computation system which is applicable to both single and dual satellite crossover measurements has been developed.

## 2.2 Crossover Measurement Geometry

The intersections of the ground track of the subsatellite point for an Earth-orbiting satellite on the surface of the Earth, referred to as the "crossover" points are caused by rotation of the Earth and, to a lesser extent, non-Keplerian perturbations of the satellite's orbit (Figure 2.1). Assuming the crossing occurs at times  $t_i$  and  $t_j$ , where  $t_i < t_j$ , and that the sea surface heights,  $h(t_i)$  and  $h(t_j)$ , are made precisely at these two times, a crossover measurement (Figure 2.2),  $\Delta h(t_i, t_j)$ , can be computed as follows :

$$\Delta h(t_i, t_j) = h(t_i) - h(t_j) \quad (2.1)$$

The altimeter measurement model, defined using the height above a reference ellipsoid has been described by Eq. (1.4).

In view of Eq. (2.1), the crossover measurement model becomes:

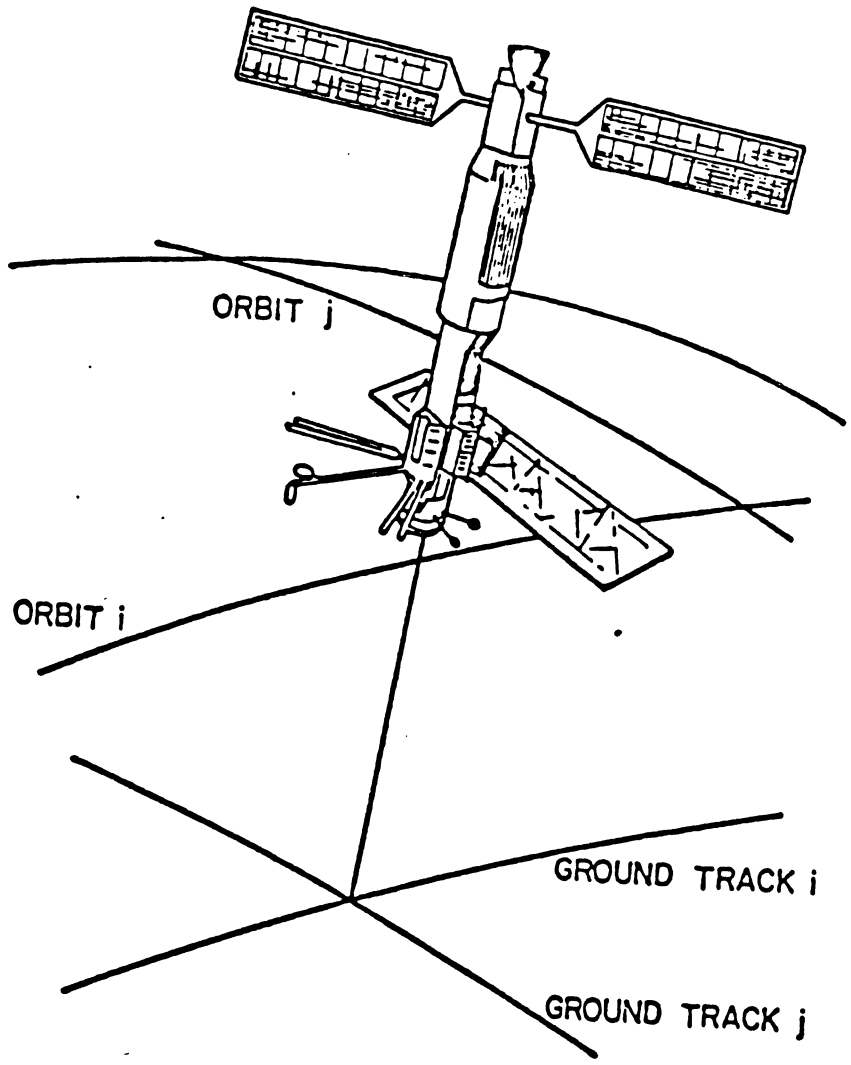
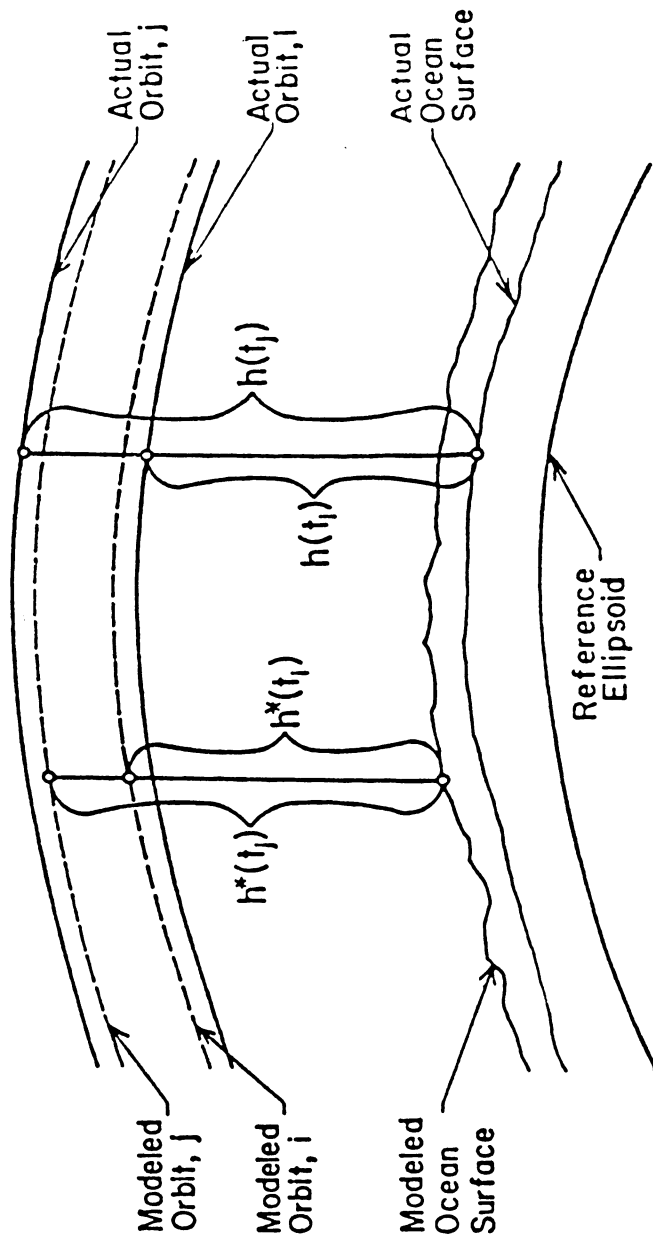


Figure 2.1 Altimeter Crossover Geometry

# SINGLE AND DUAL SATELLITE ALTIMETER CROSSOVER MODEL



crossover measurement is

$$\Delta h^*(t_i, t_j) = h^*(t_i) - h^*(t_j)$$

Figure 2.2 Altimeter Crossover Measurement Model

$$\begin{aligned}\Delta h(t_i, t_j) &= \Delta h_e - \Delta h_{al} \\ &= \Delta h_{sg} + \Delta h_i + \Delta h_a + \Delta h_s + \Delta h_g + \Delta h_s + \Delta h_o + \Delta \varepsilon\end{aligned}\quad (2.2)$$

were  $\Delta$  denotes the difference in the values defined at times,  $t_i$  and  $t_j$ . The time tags  $t_i$  and  $t_j$  can be those of a single satellite or of two difference satellites.

Note that any nontemporal or very long period ocean phenomena, that are relatively invariant during the time interval  $t_i$  to  $t_j$ , will be eliminated by the differencing procedure. In particular, the constant or quasi-stationary part of  $\Delta h_g$  and  $\Delta h_o$  will be identically zero in Eq. (2.2). Slow time-varying quantities, like  $\Delta h_{sg}$ , will also vanish. If the ocean surface is static and the orbit used to compute altimeter measurements is perfect, then the differenced altimeter height, would simply be the orbital altitude difference at  $t_i$  and  $t_j$ . Since the ocean surface is dynamic,  $\Delta h(t_i, t_j)$  includes a contribution which represents the temporal change in the ocean surface at the crossover point with respect to the geocenter.

For the case of altimeter crossovers from two different satellites carrying radar altimeters,  $t_i$  and  $t_j$  in Eq. (2.2) denotes time tags for satellites  $i$  and  $j$ , respectively. The geographically correlated contribution of  $h_e$ , which would be eliminated for single satellite crossovers, will be different at the subsatellite point for two satellite orbits with distinct altitudes and inclinations. In essence, the zonal harmonics which comprise part of the geographically correlated gravity error are not observable using crossover data collected from a single satellite with a circular orbit [Rosborough, 1986]. Dual satellite crossover data generated from two satellites, depending on their respective inclinations and altitudes, will have a sensitivity to the zonal harmonics.

It is rare, however, that measurements are actually available precisely at the crossover times. In practice, a "pseudo measurement" would must be formed by interpolating from available altimeter measurements near the vicinity of the crossover times using nominal orbits

Since the orbit and ocean model will not be perfect, the actual computed crossover measurement is

$$\Delta h^*(t_i, t_j) = h^*(t_i) - h^*(t_j) \quad (2.3)$$

where \* denotes that the altimeter measurements are computed from nominal orbits with a particular ocean surface and orbit model. Hence,  $\Delta h^*(t_i, t_j)$  in Eq. (2.3) represents also a contribution of unmodeled forces acting on the satellite in the radial component, as well as temporal changes in ocean topography due to inadequate modeling of ocean dynamics.

### 2.3 Crossover Measurement Computation

As described in the preceding section, the location of crossovers are functions of two time tags,  $t_i$  and  $t_j$ , which depends on the satellite ephemerides. Analytic theory has been used [Shum, 1983; Santee, 1985] to predict locations and time tags of single and dual satellite crossovers. One of the advantages of the analytic theory is that it provides approximate crossover locations which can be upgraded using an ephemeris determined by tracking data. However, the theory used to predict crossover solutions, especially for the case of a general dual satellite scenario, is complicated and may not yield accurate crossover locations.

A generalized single and dual satellite crossover measurement computation software system has been developed to compute single and dual satellite crossover time tags, locations and interpolated altimeter measurements at crossover locations. The details of crossover computation procedures are given below:

Step 1: Altimeter Geophysical Data Records (GDR) which consist of altimeter measurements, sea surface heights and nominal orbits predicting the location of the satellite with respect to the center of mass of the Earth are used as input to the software system. Optional input can include user supplied orbits or mean orbit elements for the satellites. If the input is mean orbit elements, then the satellite ground tracks will be generated by the dynamic equations of motion and only point mass and  $J_2$  effects of the Earth's gravity field considered. Ground tracks are grouped into passes by a complete revolution, from  $-0.5^\circ$  longitude to  $360.5^\circ$  longitude. The small extension at the ends of each pass is for the future interpolation procedures.

Step 2 Two passes are selected from either a single satellite or from two different satellites for each crossover computation. The latitudes are first modeled by a cubic spline interpolation function [IMSL, 1984] for every 15 data points during the crossover searching procedure. The smoothness and stability of the interpolation function are important for solving the crossover time with an accuracy better than one ms (millisecond). If the sign of the latitude difference between the two ground tracks has changed within a specified longitude interval (e.g.

$10^0$ ), there is a crossover point in this longitude window. Then the approximate crossover point can be solved by an iterative procedure with a  $10^{-3}$  degree convergence criterion in both latitude and longitude. This corresponds to an accuracy approximately  $10^{-2}$  second.

Step 3 Windows (10 seconds) centered at the approximate crossover point are then opened for both passes. In these windows, latitudes, satellite orbit heights and time tags are each modeled by cubic spline interpolation functions with longitude as the independent variable through every data point. The accurate crossover location (latitude and longitude), and the time tag are then solved by another iterative procedure. The iteration convergence criterion is  $10^{-5}$  degree in both longitude and latitude at this time. This convergence criterion gives a crossover time accuracy better than one ms. Generally, the convergence needs only 1 or 2 Newton-Raphson iterations. Because the orbit heights above the reference ellipsoid in a 10 seconds window are very smooth, they are modeled by a cubic spline interpolation function, but the sea surface heights measurements contain high frequency noise introduced from altimeter and geoid gradients. The sea surface heights are modeled by a least-squares cubic spline function and the crossover measurement is evaluated at the crossover time. Crossover data are rejected if the standard deviation of the least-squares fits is too large or there are not sufficient data in the windows for either one of the passes.

Step 4 If it is not the last pairs of passes, go to Step 2. Otherwise the



computation is completed.

Figure 2.3a shows a relatively good case where the least square cubic spline fit of the sea surface heights in a 10 seconds window has an rms residual of 1.51 cm. Figure 2.3b shows a worst case with a residual of 9.42 cm. For the computation of Geosat crossover measurements, crossover data with a least square cubic spline fit residual greater than 9 cm were edited. Crossover measurements are then sorted into time order and tagged with address reference indices.

Figure 2.4 shows the locations of single satellite crossovers for a 10 day ERS-1 orbit which has an inclination of  $98^{\circ}$  and an altitude of 800 km. Figure 2.5 shows the locations of dual satellite crossovers for a 10-day ERS-1 orbit and a 10-day Topex orbit which has an inclination of  $63^{\circ}.4$  and an altitude of 1300 km. Excellent geographical coverages are seen in both cases.

#### **2.4 Gravity Field Solution Methodology Using Altimeter Crossovers**

Procedures required to use single- and dual-satellite crossover measurements for orbit determination and geophysical parameters reduction are different from the processing of conventional ground based tracking data, such as laser range. Several procedures which are unique to crossover measurements must be employed. The description of these procedures given below can be adapted to most orbit determination computer programs, however, the description pertains to the University of Texas Orbit Processor (UTOPIA) described by Schutz and Tapley [1980]:

- Step 1: Crossover measurements for satellite  $i$  and  $j$  are computed from nominal orbits using the procedures described in the preceding section.

Cubic spline fit for altimeter crossovers

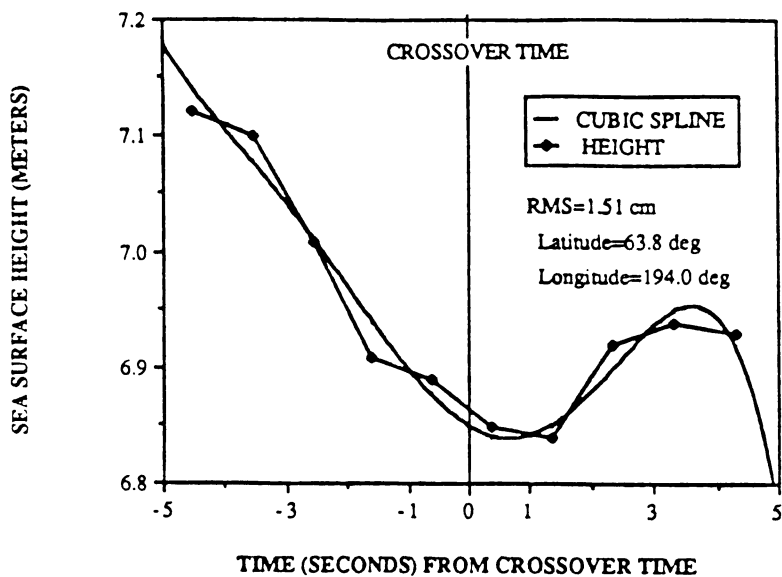


Figure 2.3a

Cubic spline fit for altimeter crossovers

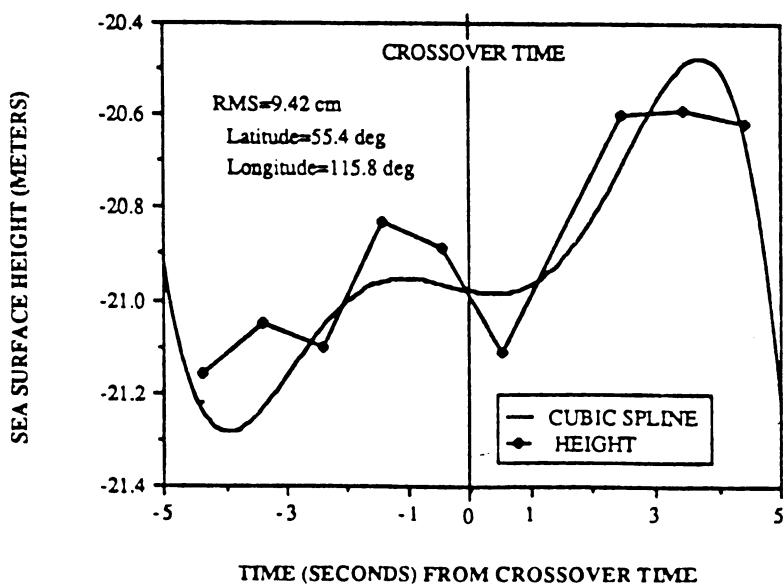


Figure 2.3b

Figure 2.3 Cubic Spline Fit for Geosat Crossovers

ERS-1 Crossovers (10 day, 9814 points)

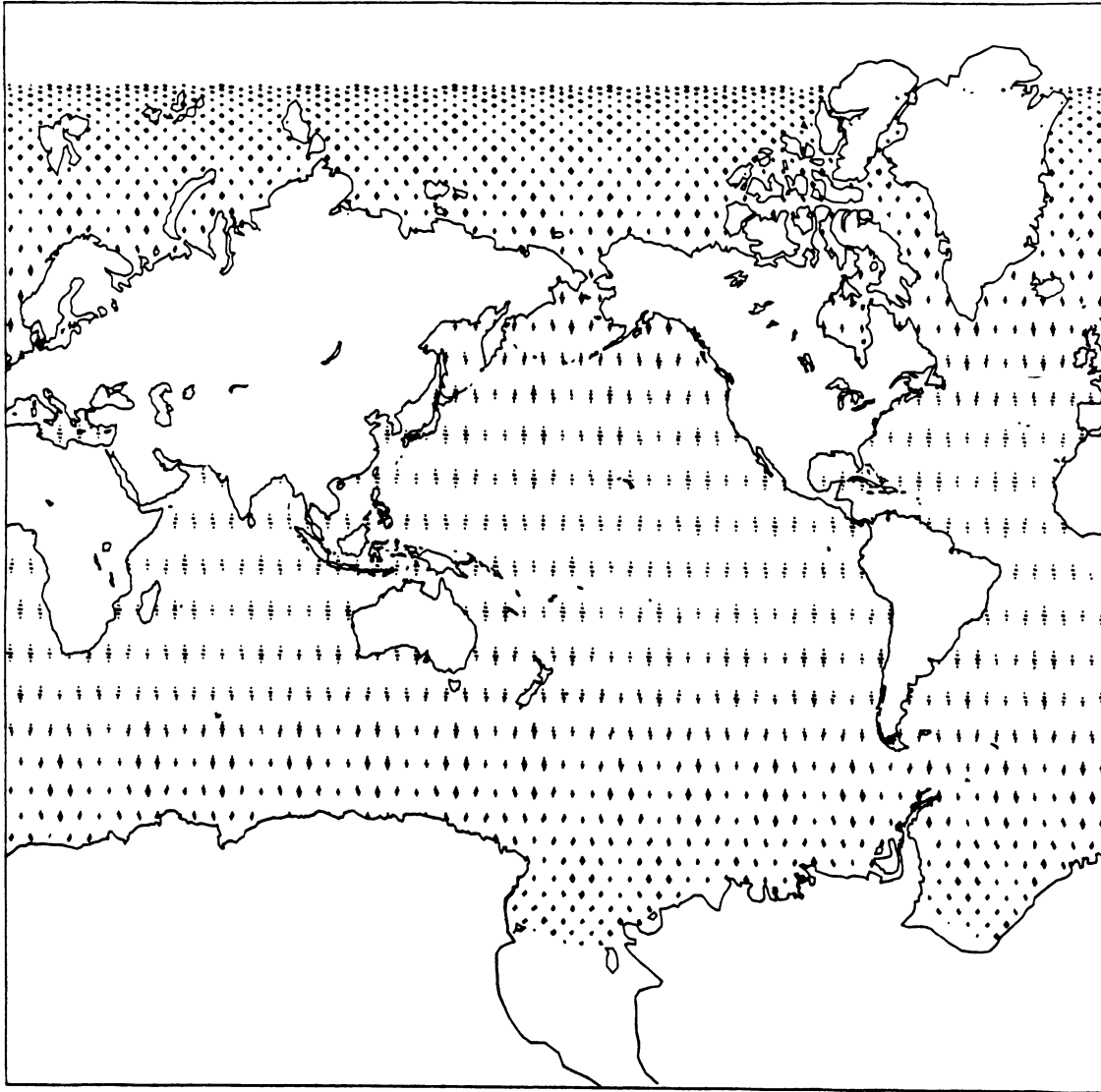


Figure 2.4 ERS-1 Altimeter Crossovers

Topex/ERS-1 Crossovers (10 day, 32100 points)

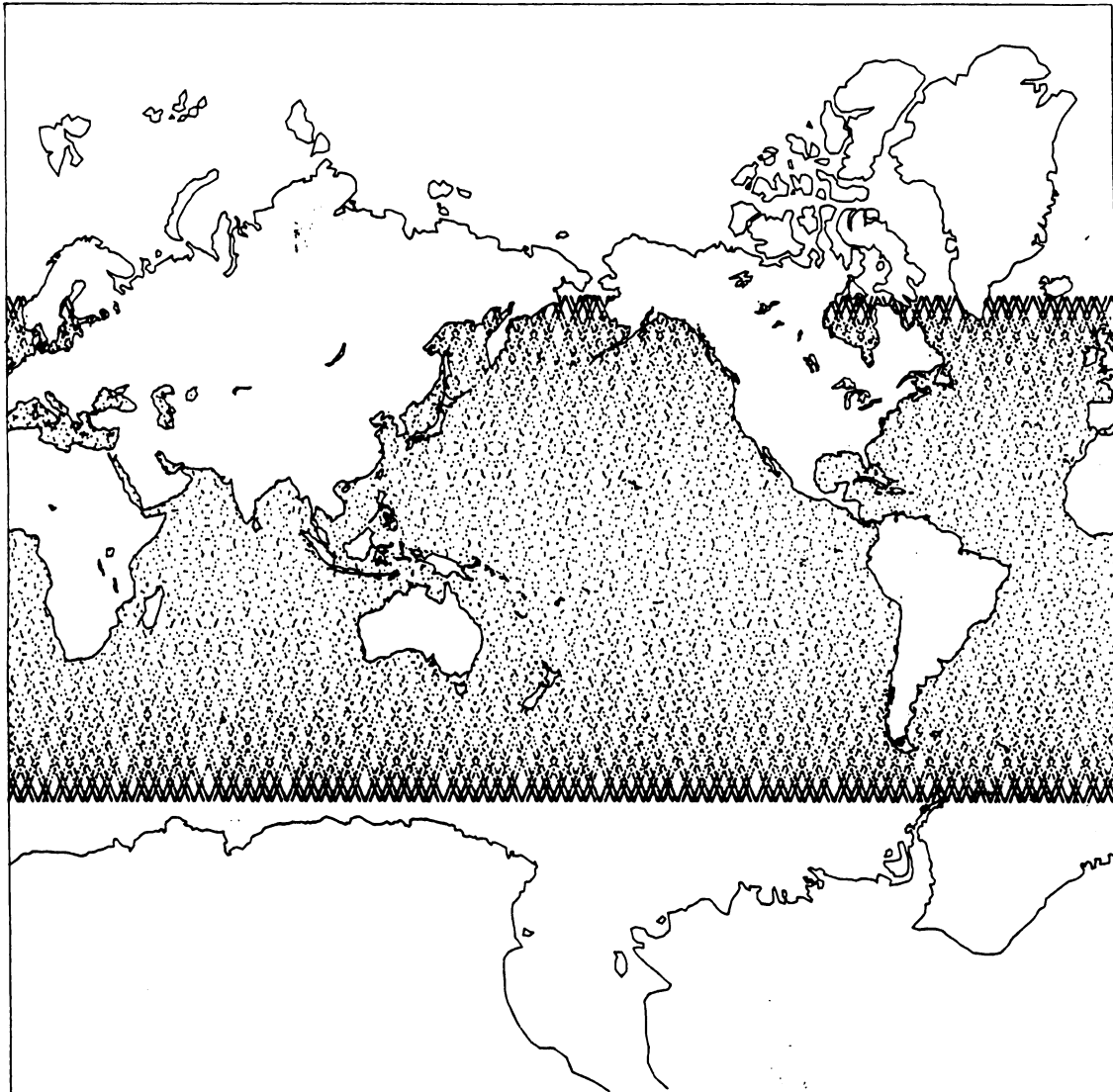


Figure 2.5 Topex/ERS-1 Dual-Satellite Crossovers

The nominal orbits may have been previously determined from a least-squares estimate using ground based tracking data. Crossover measurements are stored in time sequential order, and the crossover occurrences are referenced by predetermined address reference indices.

- Step 2: Ephemerides are propagated for satellites  $i$  and  $j$  and other non-crossover measurements are processed sequentially. When the crossover measurements are encountered, the measurement partial derivatives with respect to the state parameters (parameters to be estimated, e.g., dynamic parameters in the equation of motion of the spacecraft, kinematical parameters in the observation models) at the first crossover times,  $H(t_i)$ , are computed and stored on a scratch disk file according to respective address indices.
- Step 3: When the second crossover time,  $t_j$ , is encountered, the associated address identification index of  $t_j$  is decoded. A direct disk access read is then performed on the scratch disk file to obtain  $H(t_i)$ , from which the crossover partial derivative  $H(t_i, t_j)$  and the crossover residual can be computed and accumulated into the information matrix. This procedure is repeated until all measurements are processed. The final result of this step is the information equation containing fully accumulated partial derivatives for all available measurements, including crossover measurements, except for those edited as a result of excessively large residuals.
- Step 4: The estimate of the state parameter adjustment is obtained using the

technique of Gentlemen [1973]. If deemed necessary due to large adjustments, the entire process can be repeated beginning with Step 1. Otherwise, a small change in the orbit may produce acceptably small changes in the crossover times and locations from those obtained in the initial execution of Step 1. In this case, another iteration can be performed beginning with Step 2

The procedure described above has been implemented in UTOPIA, and the application using Seasat and Geosat crossover measurements have been performed.

## 2.5 Sensitivity of Geopotential Coefficients Using Crossover Data

In this section, analytic theory is used to examine the sensitivity of single and dual satellite altimeter crossover data to geopotential coefficients. The radial orbit error due to geopotential perturbation can be represented in a spatial domain for near-Earth, near-circular satellite orbits. For a near-circular orbit (orbit eccentricity  $\sim 0$ ), the radial orbit error can be expressed in terms of the order zero part ( $q = 0$  in eccentricity function) as follows [Tapley and Rosborough, 1985b; Rosborough, 1986]:

$$\begin{aligned} \Delta r^{(0)} = & \sum_{l=1}^{\infty} \sum_{m=0}^l \sum_{p=0}^l D_{lmp} \tilde{\Phi}_{lmp}^c (\bar{C}_{lm} \cos m\lambda + \bar{S}_{lm} \cos m\lambda) \\ & \pm \sum_{l=1}^{\infty} \sum_{m=0}^l \sum_{p=0}^l D_{lmp} \tilde{\Phi}_{lmp}^s (\bar{C}_{lm} \sin m\lambda - \bar{S}_{lm} \sin m\lambda) \end{aligned} \quad (2.4)$$

where

$\Delta r^{(0)} \sim$  radial orbit error to order zero in eccentricity ( $q = 0$ )

- $\bar{C}_{lm}, \bar{S}_{lm} \sim$  geopotential coefficients  
 $D_{lmp} \sim$  function of satellite altitude and inclination  
 $\lambda$  longitude  
 $lmpq$  are indices for the summation  
 $\tilde{\Phi}_{lmp}^c$  and  $\tilde{\Phi}_{lmp}^s \sim$  latitude functions  
+ sign denotes satellite is on ascending pass  
- sign denotes satellite is on descending pass

Note that Eq. (2.4) represents only the order zero (in eccentricity) part of the radial perturbation. The higher order effects ( $q > 0$ ) for near-circular orbits are negligible for this study.

The first term in Eq. (2.4) can be described as the geographically depend mean radial orbit error:

$$\gamma = \sum_{l=1}^{\infty} \sum_{m=0}^l \sum_{p=0}^l D_{lmp} \tilde{\Phi}_{lmp}^c ( \bar{C}_{lm} \cos m\lambda + \bar{S}_{lm} \sin m\lambda ) \quad (2.5)$$

And the second term is the geographical variability error about the mean:

$$v = \pm \sum_{l=1}^{\infty} \sum_{m=0}^l \sum_{p=0}^l D_{lmp} \tilde{\Phi}_{lmp}^s ( \bar{C}_{lm} \sin m\lambda - \bar{S}_{lm} \cos m\lambda ) \quad (2.6)$$

To this level of approximation, for single satellite crossovers, the crossover error can be expressed as follows:

$$\Delta x = 2v$$

$$= 2 \sum_{l=1}^{\infty} \sum_{m=0}^l \sum_{p=0}^l D_{lmp} \tilde{\Phi}_{lmp}^s (\bar{C}_{lm} \sin m \lambda - \bar{S}_{lm} \sin m \lambda) \quad (2.7)$$

Geographically correlated orbit error due to the perturbations of zonal spherical harmonics (i.e.  $\bar{C}_{l0}$ ) are unobservable from single satellite crossovers because that  $\Delta \gamma = \gamma_i - \gamma_j$  as defined by Eq. (2.5) is zero for the same satellite.

For dual satellite crossovers with distinct inclinations and altitudes, the crossover error between satellite  $i$  and  $j$  can be expressed as follows:

$$\begin{aligned} \Delta x &= \gamma_i - \gamma_j + v_i - v_j \\ &= \sum_{l=1}^{\infty} \sum_{m=0}^l \sum_{p=0}^l \left( D_{lmp} \tilde{\Phi}_{lmp}^c \right)_i (\bar{C}_{lm} \cos m \lambda + \bar{S}_{lm} \sin m \lambda) \\ &\quad - \sum_{l=1}^{\infty} \sum_{m=0}^l \sum_{p=0}^l \left( D_{lmp} \tilde{\Phi}_{lmp}^c \right)_j (\bar{C}_{lm} \cos m \lambda + \bar{S}_{lm} \sin m \lambda) \\ &\quad \mp \sum_{l=1}^{\infty} \sum_{m=0}^l \sum_{p=0}^l \left( D_{lmp} \tilde{\Phi}_{lmp}^s \right)_i (\bar{C}_{lm} \sin m \lambda - \bar{S}_{lm} \cos m \lambda) \\ &\quad \pm \sum_{l=1}^{\infty} \sum_{m=0}^l \sum_{p=0}^l \left( D_{lmp} \tilde{\Phi}_{lmp}^s \right)_j (\bar{C}_{lm} \sin m \lambda - \bar{S}_{lm} \cos m \lambda) \end{aligned} \quad (2.8)$$



The sensitivity of geopotential coefficients using altimeter crossover data can thus be inferred from Eq. (2.8) and Eq. (2.9) for the case of single and dual satellite crossovers, respectively. For single satellite crossovers, the sensitivity coefficient can be expressed as follow:

$$\begin{aligned}
 S_{\alpha_{lm}} &\equiv \frac{\partial \Delta x}{\partial \alpha_{lm}} \\
 &= 2 \frac{\partial v}{\partial \alpha_{lm}}
 \end{aligned}
 \tag{2.9}$$

where  $S_{\alpha_{lm}}$  = sensitivity of geopotential coefficient  $\alpha$  of degree  $l$  and order  $m$  (i.e.  $\bar{C}_{lm}$  or  $\bar{S}_{lm}$ ).

For dual satellite crossovers, the sensitivity is again the partial of  $\Delta x$  with respect to the geopotential coefficients.

$$\begin{aligned}
 S_{\alpha_{lm}} &\equiv \frac{\partial \Delta x}{\partial \alpha_{lm}} \\
 &= \frac{\partial \gamma_i}{\partial \alpha_{lm}} - \frac{\partial \gamma_j}{\partial \alpha_{lm}} + \frac{\partial v_i}{\partial \alpha_{lm}} - \frac{\partial v_j}{\partial \alpha_{lm}}
 \end{aligned}
 \tag{2.11}$$

for satellites  $i$  and  $j$ .

Figure 2.6 shows the sensitivity indices computed for a (36x36) geopotential field to the dual satellite crossovers for Topex and ERS-1 using Eqs. (2.7) and (2.8). Zonal

harmonics, although weak compared to some geopotential coefficients, are sensitive to the dual-satellite crossover data for Topex and ERS-1 orbits. Figure 2.7 shows a plot of crossover rms per order of the geopotential predicted for Topex, ERS-1 and Topex/ERS-1 orbits assuming errors in the geopotential are given by the differences of GEM-10B [Lerch et al., 1981] and GRIM-3B [Reigber et al., 1983]. Figure 2.7 shows that the Topex/ERS-1 dual satellite crossovers have a consistently higher crossover rms over the single satellite crossovers for Topex, meaning that, depending on the orbital characteristics for the two altimetric satellites, the dual satellite crossovers in general are more sensitive to geopotential coefficient error. In particular, order one geopotential coefficients have significantly higher crossover rms in the dual satellite crossover than the cases for single-satellite crossovers for the Topex and ERS-1 orbits.

## **2.6 Orbit Determination Experiments Using Altimeter Crossover Data**

Gravity field solutions which have included or excluded altimeter crossover data have been evaluated using orbit fits to examine the effect of crossover data on the gravity solutions. Table 2.1 shows two 6-day fits for Geosat (epochs at 1986/12/7 and 1987/1/1) using three different gravity field. PGS-1331 is the Seasat tailored field [Lerch et al., 1982], and the PTGF2 fields are the University of Texas preliminary Topex gravity field [Tapley et al., 1987]. Crossover residual rms is a good diagnostic of global radial orbit accuracy for altimetric satellite orbit, as the variability part of the radial orbit error can be approximated by dividing the square root of 2 into the crossover residual rms [Shum, 1983]. The orbit fits with the PTGF2 field which included Seasat crossover data are at the 40-50 cm level, while the other fields produce

fits at the meter level. Although the crossover rms does not include the geographically correlated (mean) part of the radial orbit error, a lower crossover rms indicates the variability part of the radial orbit error is significantly reduced by the inclusion of crossover data in the gravity solution.

Table 2.1 Evaluation of Earth Gravity Models With and Without Altimeter Crossover Data

<ul style="list-style-type: none"> <li>• Geosat Orbit fits</li> <li>• Seasat altimeter data excluded or included in the gravity field solution</li> </ul>			
6 day orbit fits	Crossover residual rms (cm)		
	PGS-S4 *	PTGF2 + (without crossover)	PTGF2 + (with crossover)
1986/12/7	105	80	41
1987/1/1	111	105	47
<ul style="list-style-type: none"> <li>* GSFC Seasat-tailored field</li> <li>+ University of Texas preliminary Topex fields</li> </ul>			

The radial orbit error for the Geosat orbit, predicted by the gravity field covariance matrices, are plotted on Figure (2.8). In which, Seasat crossover data and direct altimeter measurements are included in PTGF2A gravity model. Again, smaller radial orbit errors projected to Geosat orbit by gravity field covariance matrices included

crossover data can be found consistently through entire range of geopotential orders than the one without crossovers.

## **2.7 Summary**

In summary, generalized methodology for the computation of single- and dual-satellite altimeter crossover times, locations and measurements has been developed. Techniques have been developed to use single and dual satellite crossover measurements for precision orbit determination and reduction of geophysical parameters. Analytical theory has been used to examine the sensitivity of geopotential coefficients using single and dual satellite crossovers. For circular orbits, zonal harmonic coefficients which are unobservable using single satellite crossovers are sensitive to dual satellite crossovers. Depending on the orbital characteristics of the altimetric satellite, order one geopotential coefficients using dual satellite crossovers can be significantly more sensitive than those of single satellite crossovers. Numerical experiments showed that the use of Seasat crossover measurements contributes significantly to the solution accuracy of the Earth's gravity field.



# SENSITIVITY OF CROSSOVER DATA TO GEOPOTENTIAL COEFFICIENTS

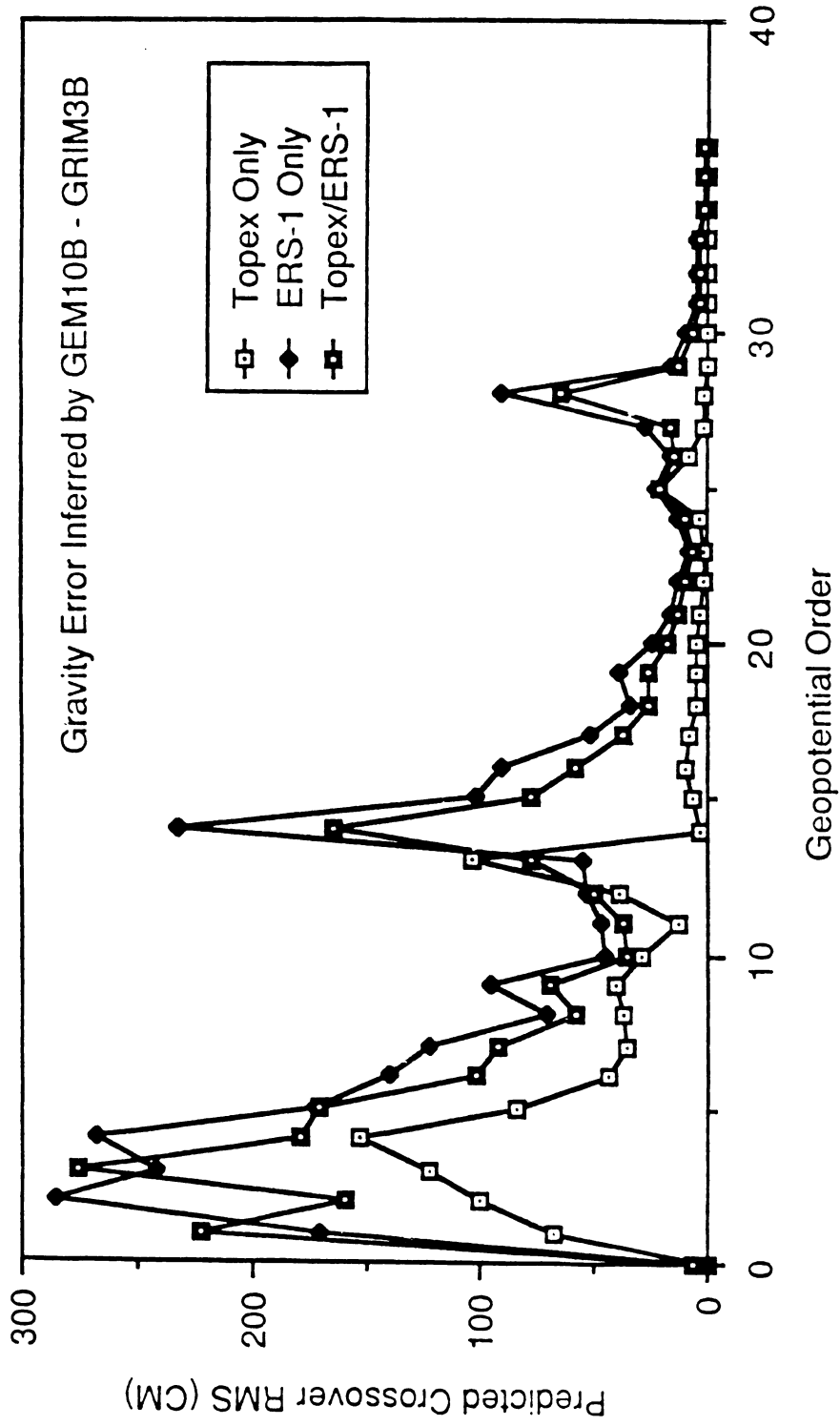


Figure 2.7 Sensitivity of Crossover Data to Geopotential Order

# Radial Error Predicted by Gravity Field Covariance Matrices

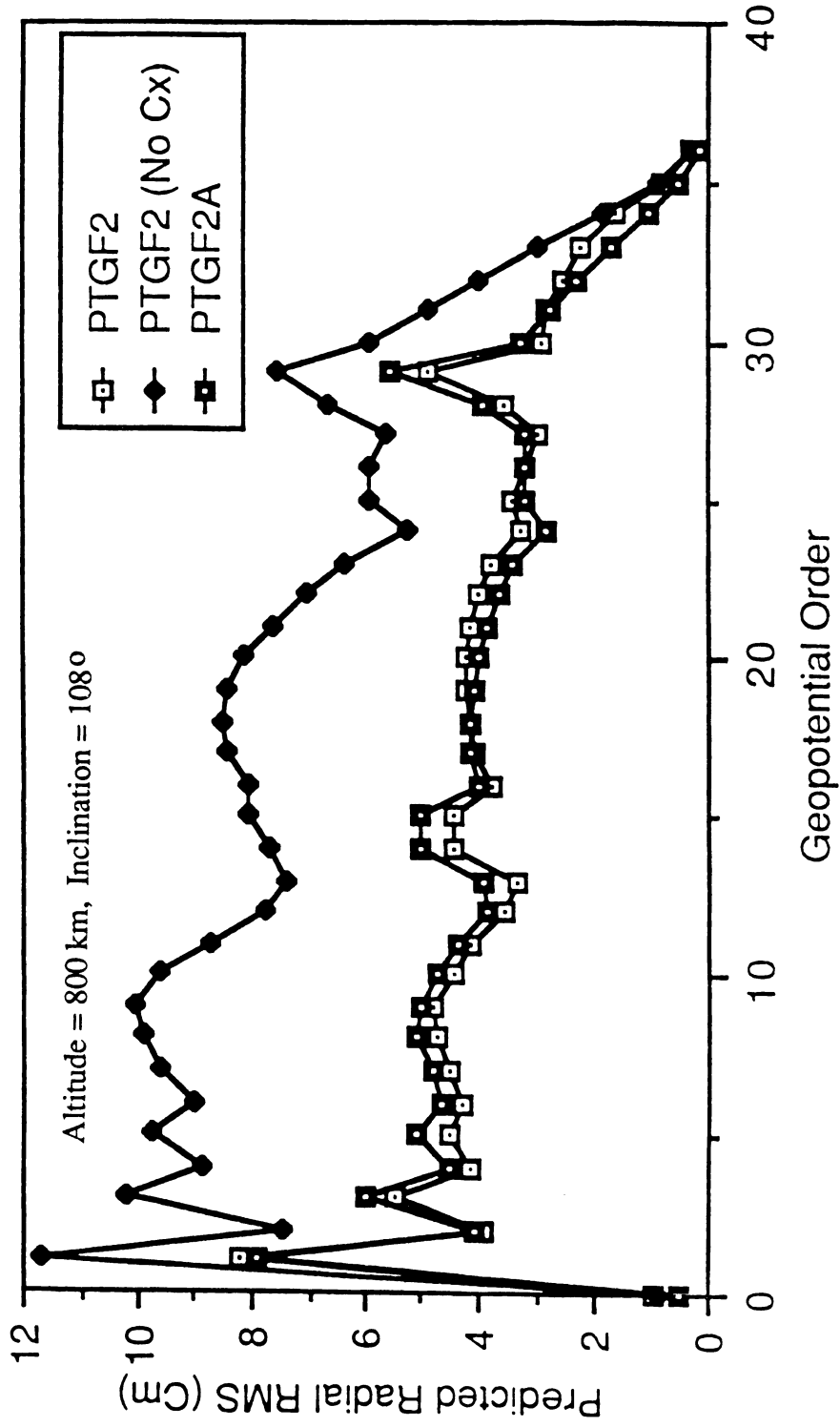


Figure 2.8 Radial Orbit Error Predicted by Gravity field Covariance Matrices

## Chapter 3

### Precision Orbit Determination for Geosat ERM

#### 3.1 Introduction

One of the major factors limiting the application of subdecimeter precision altimetric measurement is the ability to determine the radial position of the satellite orbit to a compatible accuracy. The determination of the radial component of the satellite's position is important, since radial orbit errors are directly reflected in the altimetric measurement, and consequently influence the estimates of the sea surface topography.

During the ERM, Geosat was tracked by the Navy's Opnet and the Defense Mapping Agency's Tranet (Transit Network) doppler tracking systems. Opnet consists of three radiometric tracking stations located in the continental United States and one station located in Hawaii. Ephemeris computation for the Geosat ERM are performed by the Navy Astronautics Group (NAG) using Opnet tracking data and the GEM-10B gravity model [Lerch et al., 1981]. This ephemeris has a radial uncertainty of 3.38 m (rms), as indicated by the computation of the crossover residual rms during a 17 day repeat period. This large radial orbit error is a major limitation in the determination of absolute sea surface topography. In addition the NAG ephemeris, a more accurate Geosat ERM ephemeris has been computed by The University of Texas Center for Space Research (CSR) using a new gravity model, PTGF3A [Tapley et al., 1988b], and 80 days of Tranet Doppler tracking data from a global 48 station network [Smith et al., 1988]. The crossover rms error for the unique arc solution is 0.32 m. Geosat ERM orbit fits and the evaluations of CSR and NAG orbits are presented in the



following sections.

### **3.2 A General Statement of the Orbit Determination Problem**

To separate variations in the satellite height from variations in the ocean surface height and to orient the ocean surface height measurements with respect to a common center of mass coordinate system, an independent determination of the radial component of the satellite orbit is required. The fundamental components involved in the determination of a near earth satellite orbit are the following:

- The mathematical model of the differential equations which describes the motion of the satellites in an inertial coordinate system;
- The solution of these differential equations;
- The measurements of the satellite translational motion;
- The mathematical technique which enables the estimation of the satellite's position, velocity, and constant parameters in the force and observation models.

Tracking data are required to determine the orbit. A weighted least squares approach can be used to determine the position and velocity which best fit the tracking data. The differential equations of translational motion require accurate models of all gravitational and nongravitational forces acting on the satellite. Ground-based measurement models are also required to define the orientation of the Earth in the space with respect to the moon, sun, and planets and the orientation of the Earth with respect to the angular velocity vector.

### 3.3 Dynamical Equations of Motion and Force Models

The orbit determination accuracy depends on the knowledge of the dynamic forces acting on the satellite. The dominant forces which influence the satellite's orbit are due to the gravitational attraction of the Earth, sun and moon and their tidal effects, the effects of atmospheric resistance, and the influence of the direct and reflected solar radiation pressure.

The dynamical equations for the motion of a satellite, expressed in the geocentric inertial coordinate system are as follow:

$$\ddot{\vec{r}} = \frac{GM\vec{r}}{r^3} + \sum f(\vec{r}, \vec{v}, \vec{c}, t) \quad (3.1)$$

where

$$\frac{GM\vec{r}}{r^3}$$

gravity of spherical Earth

$$GM$$

product of the universal constant of gravitation and the mass of the Earth

$$\vec{r}, \vec{v}$$

position and velocity vectors of the satellite

$$\sum f(\vec{r}, \vec{v}, \vec{c}, t)$$

perturbation forces

Gravitational:

- Non-spherical Earth
- Luni-solar and planetary
- Solid Earth tides
- Ocean tides

- General relativity

Nongravitational:

- Atmospheric drag
- Solar radiation pressure
- Earth albedo radiation pressure
- Empirical forces

$\vec{c}$

Physical parameters used to specify the force models

The emphasis on gravity model improvements is due to the fact that geopotential modeling error remains the single largest error source in the precise computation of near-Earth satellite orbits. Depending on the altitude and orbital characteristics, the solar radiation pressure and atmospheric drag are among the next largest error sources.

### Gravity Field of the Earth

The common method of modeling the geopotential for orbit determination applications and the most convenient for examining satellite perturbations is the spherical harmonic representation. This formulation is obtained by solving Laplace's equation

$$\nabla^2 U = 0 \tag{3.2}$$

in Earth-fixed spherical coordinates and imposing the boundary condition that the potential,  $U$  goes to zero as  $r$ , the radius, goes to infinity. The solution is

$$U = \frac{GM}{r} \sum_{l=0}^{\infty} \sum_{m=0}^l \left[ \frac{a_e}{r} \right]^l \bar{P}_{lm}(\sin\phi) [ \bar{C}_{lm} \cos m\lambda + \bar{S}_{lm} \sin m\lambda ] \quad (3.3)$$

where

$GM$	the product of gravitational constant and the mass of the Earth
$a_e$	semimajor axis of the Earth's reference ellipsoid
$r, \phi, \lambda$	satellite distance, latitude and longitude respectively, in a body - fixed coordinate system
$\bar{C}_{lm}, \bar{S}_{lm}$	normalized spherical harmonic coefficients of degree $l$ and order $m$
$\bar{P}_{lm}$	normalized Legendre associated functions

Usually, the coordinate system, which is chosen, has its origin located at the center of mass of the Earth. In this case, the  $\bar{C}_{1,0}$ ,  $\bar{S}_{1,0}$ ,  $\bar{C}_{1,1}$  and  $\bar{S}_{1,1}$  coefficients are zero. The  $\bar{C}_{0,0}$  coefficient is exactly 1.0 (the point mass contribution of the Earth).

### Atmospheric Drag

The dominant feature of atmospheric resistance for most satellite is a drag force in the opposite direction to the speed of the spacecraft. Drag is usually modeled as

$$\vec{F}_D = -\frac{1}{2} \rho \left[ \frac{C_D A}{m} \right] |\vec{V}_r|^2 \vec{u} \quad (3.4)$$

where  $\rho$  is the atmospheric density,  $C_D$  is the drag coefficient,  $A$  is the cross-sectional area,  $\vec{V}_r$  is the speed relative to the atmosphere,  $m$  is the mass of satellite, and  $\vec{u}$  is the unit vector in the  $\vec{V}_r$  direction.

### Solar Radiation Pressure

Radiation from the sun produces a small force by transferring momentum from particles streaming out from the sun to the satellite. This force for a satellite is approximately:

$$\vec{F} = -P (1 + \eta) \frac{A}{m} \nu \vec{u} \quad (3.5)$$

where  $\vec{F}$  is the direct solar radiation force per unit mass,  $P$  is the momentum flux due to the sun,  $A$  is the cross-sectional area normal to the sun,  $m$  is the mass of satellite,  $\vec{u}$  is the unit vector point from the satellite to the sun,  $\eta$  is the reflectivity coefficient with values between 0 and 1, and  $\nu$  is an eclipse factor such that  $\nu = 0$  if the satellite is in shadow of the sun,  $\nu = 1$  if the satellite is in sunlight,  $0 < \nu < 1$  if the satellite is partial shadow or penumbra. The passage of the satellite from sunlight to

frequency shift of the received signal compared with the transmitted signal. If the signal is transmitted from the satellite and received by the ground tracking station, it is called a one-way doppler. Tranet is a one-way doppler system with the transmitter located on the spacecraft.

The Tranet tracking data was converted to average range rate by the following relation:

$$\frac{d\rho}{dt} = \frac{cN}{f_s \Delta t} - \frac{(f_g - f_s)c}{f_s} \quad (3.6)$$

where

$\rho$  = range between the satellite transmitter and the ground tracking receiver

$c$  = speed of light ( 299792458 m/s )

$f_s$  = satellite transmitter frequency

$f_g$  = ground tracking station receiver frequency

$N$  = doppler count

$\Delta t$  = doppler count interval

Eq. (3.6) is the method currently used to process Tranet doppler data, e.g. the Geosat Tranet data. By integrating the the range change over a pass of tracking data, a biased range measurement can be determined with a precision of about 5 cm. Biased range is a more powerful data type than doppler. However, it was not used in this study since a previous analysis of Geosat data identified a number of significant problems which would have to be overcome before it could be processed with a high

degree of confidence [Topex, 1987].

### 3.5 Orbit Determination Process

The dynamical equation of motion (Eq. (3.1)) can be expressed in first order form as follow:

$$X = \begin{bmatrix} \vec{r} \\ \vec{v} \\ \vec{c} \end{bmatrix} \quad (3.7)$$

where

$X$  = augmented state vector

$\vec{r}$  = position vector

$\vec{v}$  = velocity vector

$\vec{c}$  = vector of unknown constant model parameters to be estimated

Then Eq. (3.1) can be written as:

$$\dot{X} = F(X, t) \quad (3.8)$$

with initial condition:

$$X(t_0) = X_0 \quad (3.9)$$

The observation vector can be related with the state vector by:

$$Y = G(X, t) + \varepsilon \quad (3.10)$$

where

$G ( X, t )$  is the functional relationship between the state vector and the observation vector

$\varepsilon$  is the random measurement noise vector

Assuming that there is a reasonable reference trajectory available, then the nonlinear system of Eqs. (3.8) and (3.10) can be expanded in a Taylor's series about the reference trajectory,  $X^*$  at each point in time. If the expansions are truncated to the first order terms, then the nonlinear orbit determination problem in which the complete state vector is to be estimated can be replaced by a linear orbit determination problem in which the deviation from a reference trajectory is to be determined. There are several results from the field of linear estimation theory can be applied to the linearized orbit determination problem.

To conduct this linearization procedure, let

$$x ( t ) = X ( t ) - X^* ( t ) \quad (3.11)$$

$$y_i = Y_i - Y_i^* \quad (3.12)$$

where

$X^* ( t )$  is the nominal trajectory.

$Y_i^* = G ( X_i^*, t_i )$  is the computed observation at decimate time epoch.

Then the linearized system derived from the expansions of Eqs. (3.8) and (3.10) can be written as:



$$\begin{aligned} \dot{x} &= A(t)x \\ y_i &= \tilde{H}_i x_i + \varepsilon_i, \quad i = 1, 2, \dots, l \end{aligned} \quad (3.13)$$

where

$$A(t) = \frac{\partial F}{\partial X}(X^*, t) \quad (3.14)$$

$$\tilde{H}_i = \frac{\partial G}{\partial X}(X_i^*, t_i), \quad i = 1, 2, \dots, l \quad (3.15)$$

The general solution of the first linear equation in Eq. (3.13) can be expressed as:

$$x(t) = \Phi(t, t_0)x_0 \quad (3.16)$$

where  $x_0$  is the epoch value of state vector. The matrix  $\Phi(t, t_0)$  is called the state transition matrix and it maps the epoch state vector to time  $t$ .

If the following definition is used

$$y(t) = \tilde{H}\Phi(t, t_0)x_0 + \varepsilon = Hx_0 + \varepsilon \quad (3.17)$$

where  $H = \tilde{H}\Phi$  and the subscript on  $x_0$  is dropped, then the linear system, Eq.(3.17), can be expressed as follows:

$$y = Hx + \varepsilon \quad (3.18)$$

where  $x$  is the epoch state vector to be estimated.

The minimum variance linear estimation theory gives the best estimate  $\hat{x}$ , which minimizes the observation residuals, as:

$$\hat{x} = \left( H^T R^{-1} H + \bar{P}^{-1} \right)^{-1} H^T R^{-1} y \quad (3.18)$$

where

$R$  the observation error covariance matrix

$\bar{P}$  *a priori* covariance matrix

The solution can be solved by the Givens-Gentleman Square-Root-Free accumulation approach [Gentleman, 1973].

### 3.6 Tranet Tracking System for Geosat ERM

During the Geosat ERM, precision orbit determination was performed by the Naval Surface Weapons Center (NSWC) using the Tranet tracking system. The Tranet data is not available for general distributions to the public. However, under agreement with the Defense Mapping Agency (DMA), 80 days ( 11/8/1986 - 1/27/1987 ) of Tranet data were made available for the assessment of the Tranet tracking system to perform precision orbit determination for the planned Topex/Poseidon Mission.

The distribution of ground-based tracking stations is of fundamental importance in the orbit computation. The station distribution, in combination with the accuracy and quantity of data collected at each site, determines the ultimate accuracy with which

the orbit can be ascertained. The Tranet system is a global network of stations operating with one of two types of receivers. Tracking data from 48 stations, 23 Tranet-II stations and 25 MX1502 stations, were supplied by the Defense Mapping Agency's Tranet tracking system (Figure 3.1). Station coordinates, provided by the NSWC, were rotated into the Lageos determined terrestrial reference system [Tapley et al., 1985a] and are listed in Table 3.1. The Tranet-II stations (Figure 3.2) are permanent sites which use the Electrac 547B Doppler Tracking Receiver and use rubidium or cesium oscillators. The portable Tranet stations (Figure 3.3) use a Magnovox 1502-DS (MX1502) receiver with Efratom rubidium oscillators. All stations use the CHU Associates 3330 antenna.

Tranet tracking station coordinates were supplied by NSWC. The Tranet system measures one-way range differences and operates on two frequencies, 400 MHz and 150 MHz, so that the large first-order term in the ionospheric refraction correction expansion can be eliminated. Meteorological data are collected at all sites for computing the tropospheric refraction.

Each of the two tracking receivers has a unique data storage format for use in computing range rates (or range differences). The Tranet-II data contain 400 MHz doppler counts already corrected for the first order ionospheric refraction effect. No information for the 150 MHz channel is given but a value from which the ionospheric refraction may be computed is packed for each observation. The doppler count interval is approximately 20 seconds and each count is tagged in station clock time at the end of the count interval.

The Magnavox 1502 data contain doppler counts for both the 400 MHz and 150 MHz channels without any ionospheric corrections. The doppler counts on each

Table 3.1 TRANET Tracking Station Coordinates\*

Station	ID	Location	Height (m)	Geodetic Longitude (deg)	Geodetic Latitude (deg)
ASCENS	3000	Ascension Island	43.0890	345.597931	-7.907847
ST.HEL	3004	St. Helena Island	602.3430	354.283417	-15.943045
CYPRUS	3006	Dhekeia, Cyprus	128.7450	33.730690	35.001770
HAWAII	3007	Ewa Beach, Hawaii	26.7460	202.000473	21.315937
DIEGO	3010	Diego Garcia Island	-58.9730	72.376572	-7.263543
CAMBRI	3011	Cambridge Bay, Canada	7.6530	254.879059	69.117821
BAHRAI	3012	Bahraib, Arabian Gulf	-14.8880	50.608078	26.209211
ASUNCI	3013	Asuncion, Paraguay	188.160	302.387024	-25.300926
WICHIT	3015	Wichita Falls, TX	305.1170	261.490692	33.978878
SIoux	3017	Sioux City, IA	309.5150	263.627563	42.407131
SHEMYA	3018	Shemya, Alaska	75.6250	174.103851	52.728355
LASCRU	3021	Las Cruces, NM	1182.7290	253.246063	32.278805
QUITO	3022	Quito, Ecuador	2921.8791	281.506409	-0.215118
SIGONE	3024	Sigonella, Sicily	65.7200	14.922437	37.406292
SNATIA	3025	Santiago, Chile	733.5500	289.333862	-33.149483
KINSHA	3026	Kinshasa, Zaire	454.6640	15.255136	-4.370434
DENVER	3027	Aurora, CO	1684.1801	255.234985	39.714542
BANGKO	3028	Bangkok, Thailand	-15.9180	100.543198	13.724522
RAPID	3029	Rapid City, SD	994.7140	256.900970	44.161602
IDAHO	3036	Idaho Falls, ID	1449.0179	247.964691	43.516869
ARIZON	3037	Flagstaff, Arizona	2167.8350	248.177841	35.228157
NEVADA	3038	NAS Fallon, Nevada	1179.5850	241.298187	39.430286
MERIDI	3039	NAS Meridian, MI	71.9760	271.384460	32.550591
PERU	3040	Grisson AFB, IN	217.2710	273.871246	40.644283
HERNDN	3069	Herndon, VA	83.1940	282.686615	38.995449
SMITHF	3545	Smithfield, Australia	36.6740	138.654739	-34.673820
BRUSSE	3547	Brussels, Belgium	163.6160	4.359006	50.798229
MIZUSA	3548	Mizusawa, Japan	126.4350	141.133316	39.135220
WETTZE	3549	Wetzell, Germany	667.2520	12.878165	49.144413
HERNDN	3550	Herndon, VA	86.2780	282.686859	38.995464
LASCRU	3552	Las Cruces, NM	1182.4940	253.246094	32.278805
GUAM	3553	Guam, Marianas Island	94.9410	144.634552	13.439736
PRETOR	3554	Pretoria, South Africa	1607.7050	28.347746	-25.946804
SANJOS	3555	San Jose, Brazil	611.2630	314.130432	-23.217533
ANCHOR	3556	Anchorage, AL	78.7590	210.175003	61.283417
THULE	3557	Thule, Greenland	71.3870	291.245239	76.535789
MAHE	3558	Mahe, Seychelles	552.9000	55.479584	-4.670597
SANMIG	3559	San Miguel, Philippines	57.8800	120.072533	14.987878
TAFUNA	3560	Tafuna, Amer. Somoa	47.4690	189.284225	-14.329233
AUSTIN	3561	Austin, TX	218.5730	262.274475	30.383593
MCMURD	3562	Mcmurdo, Antartica	-14.3100	166.673798	-77.847626
CALGAR	3563	Calgary, Canada	1248.9980	245.706512	50.871357
OTTAWA	3564	Ottawa, Canada	48.8390	284.081238	45.399899
KERGUE	3567	Kerguelen Island	80.4860	70.256065	-49.35194
TAHITI	3568	Papatee, Tahiti Island	349.8170	210.425461	-17.566742
HERMIT	3570	Hermitage, UK	167.6280	358.715912	51.45377
SANFER	3590	San Fernando, Spain	91.4810	353.794556	36.465332
KOUROU	3591	Kourou, French Guiana	-13.3900	307.313568	5.171404

\*Reference Ellipsoid: Equatorial Radius = 6378137. m, Reciprocal of Flattening = 298.257





channel are time tagged in station clock time at the end of the doppler intervals. An algorithm is described for computation of a 400 MHz doppler count corrected for the effect of the ionosphere to first order. The count interval is approximately 5 seconds and a signal-to-noise ratio is provided for each high and low doppler count as an indication of the quality of the observation.

Doppler counts from both receivers are tagged with station clock time. Each station clock can be calibrated to maintain agreement with the master clocks which presumably correspond to Coordinated Universal Time (UTC). The calibration is performed by tracking the Navy Navigation Satellite (Navsat) and solving for the time offsets between the Navsat clocks and master clocks. The MX1502 receivers reset their clock every time a NAVSAT is tracked. Assuming no significant drift between Navsat tracking, the MX1502 data essentially time tagged in the same time maintained by the last Navsat tracked.

Ionospheric refraction is the most significant media effect the transmitted signals experience and therefore correct modeling is essential for accurate orbit determination. It was assumed that the radio transmissions from the satellite are propagated on straight line paths at the speed of light. This would be true if the propagation medium were a vacuum. Actually, there is a considerable layer of ionized gas, the ionosphere, between the satellite and the ground observer that modifies the propagation path and the velocity of the transmitted signals. The result is that the received signal is the sum of the transmitted signal, the doppler shift, and an additional apparent frequency variation caused by the ionosphere. The signal path length can change from tens to hundreds of meters over a pass. The use of dual frequency doppler data allows the removal of the first order ionospheric error. For both Tranet-II and MX1502 data, a 400 MHz

doppler count with the effect of the ionosphere removed to first order is used to calculate the average range rate using Equation (3.6).

Unlike the Tranet-II data, an ionosphere corrected 400 MHz doppler count is not supplied in the MX1502 data, but must be calculated for each observation using information from the 150 MHz channel. Therefore, the MX1502 data required significantly more preprocessing than the Tranet-II data.

Elimination of erroneous observations from the initial Tranet Doppler data is required before the best orbit fit to the data can be obtained. The detailed data preprocessing and editing procedures are described by Smith et al. [1988] and the results are summarized here: 30.8% of a total of 377968 observations from the initial data set were edited. Of the original 13489 passes, 37.7% of the passes were edited, resulting in a final data set of 8405 passes for the 80 day span.

### **3.7 Orbit Determination**

The gravity model error is the dominant error source which limits the accuracy of the spacecraft ephemeris. A preliminary Topex gravity field resulting from the Topex gravity model improvement effort, PTGF3A, which was developed at the University of Texas at Austin Center for Space Research (UT/CSR) was used to model the geopotential [Tapley, 1988b]. PTGF3A included satellite tracking data collected from a dozen satellites and included Seasat altimeter and crossover data (Table 3.2). Since the Geosat orbit is very similar to that of the Seasat, the inclusion of Seasat crossover data in PTGF3A has produced better Geosat orbit fit to the tracking data than the results obtained with the GEM-T1 geopotential model [Marsh et al., 1988].



Table 3.2 PTGF3A Tracking Data Summary

Satellite	Inclination (degree)	Eccentricity	Semimajor axis (km)	Data Type
Lageos	110	0.0046	12270	Laser
Starlette	50	0.0205	7337	Laser
Nova-1	90	0.0020	7570	Range-rate
Geos-1	59.4	0.0723	8072	Laser
Geos-2	105.8	0.0330	7706	Laser
Geos-3	115	0.0005	7220	Laser
BE-C	41.2	0.0258	7507	Laser
DI-C	40.1	0.0500	7321	Laser
DI-D	39.5	0.0800	7606	Laser
Peole	14.89	0.0160	7008	Laser
Ajisai	50	0.0006	7870	Laser
Seasat	108	0.0010	7170	Laser Range-rate Altimeter & Crossover
Oscar-14	89	0.0050	7470	Range-rate

Several experiments for computing the best fits orbit have been performed for three 17-day arcs. Evaluation of the along track orbital error frequency spectrum indicated the primary error is at the frequency of once per satellite revolution. It was found that there are significant drag error due to the mismodeling of the atmospheric density model. A set of density correction parameters [Shum et al., 1986b] were found effective in removing drag error and lowered both the doppler and crossover residual rms. The reduction of radial orbit error reflected by the lower crossover residual rms may be due to the ability of the density correction parameter to remove eccentricity error

caused by drag mismodeling which manifests itself as radial error.

Orbit fits for three Geosat ERM 17-day arcs are summarized in Table 3.3 in terms of rms range-rate and crossover residuals.

Table 3.3 Residual RMS Summary for Geosat ERM Orbit Fits

Epoch	Range Rate		Crossover	
	Number	Residual RMS (cm/s)	Number	Residual RMS (cm)
11/17/86	48308	0.69	16710	40
12/21/86	61394	0.66	16467	34
1/7/87	64815	0.65	18393	32
Average	58172	0.66	17190	35

### 3.8 Geosat ERM Ephemerides Evaluation

During the following discussions, the CSR orbit is referred to as the orbit computed by UT/CSR, and the NAG orbit is referred to as the orbit computed by Navy Astronautics Group and packed in the GDR's.

A means of evaluating the quality of the ephemeris is important. While the absolute orbit accuracy cannot be determined directly, the relative orbit accuracy could be evaluated by examining the tracking data residuals, altimeter crossover residuals and collinear altimeter profile differences. Comparisons between the CSR and the NAG orbits have been performed to estimate their relative accuracies.

The range rate residuals indicate how well the computed range rates fitted the

range rate tracking data. A low range rate residual rms generally indicates an orbit that is consistent with the tracking data. However, to a certain extent, the range rate residual can be lowered by simply tightening the observation edit criteria and editing more data. Such over-editing lowers the residual rms, but does not necessarily improve the orbit since useful orbit information can be excluded from the orbit solution. Therefore an orbit fit should not be judged solely on the size of the range rate residuals. An improved method employing what is referred to as the navigation solution, which estimates four pass parameters, was used to predict range rate residual rms that is free from gravity and troposphere model error to first order. Therefore, the predicted rms can be compared to the computed rms to assess the performance of the orbit determination process.

The crossover residual is useful as an indicator of radial orbit error. The geometry and computation of the crossover measurements have been described in Chapter 2. To determine the height of the spacecraft above the reference ellipsoid using the altimeter measurement, which measures the height above the instantaneous or actual ocean surface, height corrections for the geoid and dynamic topography must be computed. These height corrections are not well known, particularly the marine geoid, and therefore they introduce uncertainties of up to a few meters in the calculation of the height above the reference ellipsoid. At a given geographic location, the geoid errors are constant and can be virtually eliminated through the use of a differenced altimeter measurement at the crossover points. At the crossover point, the height corrections due to the geoid and constant part of the dynamic topography are the same and therefore canceled out. The residuals in the crossover, or differenced altimeter measurement,

will be a function of the orbit error, and the time varying ocean surface topography (i.e. tides, current eddies, etc.). It is assumed that orbit error will be the major contributor to the crossover measurement.

Although, the slowly changing portion of the ocean topography can be eliminated at the crossover point, the remaining temporal changes, such as ocean tide, unmodeled orbit error, short wavelength phenomena, as well as altimeter time tag error, can still be aliased into the radial error on a global basis. Therefore crossovers provide valuable information about radial orbit error sources, but the estimate is not perfect. The geographical distributions of crossovers for a Geosat ERM 17-day arc is presented in Figure 3.4. The rms crossover residual for the CSR orbit is 32 cm, however the NAG orbit has a rms crossover residual of 338 cm, almost one order of magnitude higher than the CSR's. During the Geosat ERM, the ground track of the spacecraft repeat itself over every 17 days within in a band less than 1 km. By examining the collinear altimetric profile differences, the relative radial orbit errors can be assessed. Since the collinear profiles are in the same direction along the satellite ground track, part of the variable orbit error as well as all of the geographically correlated orbit error due to geopotential perturbations are cancelled out from the differenced collinear profiles. The differences between them reflect the relative orbit error due to errors in the geopotential coefficients and the time varying sea surface topography. This expected smaller collinear rms sea surface profile residual indicates that collinear tracks will be useful for mesoscale variability studies.

Three collinear altimetric surface profiles derived from the CSR orbits and three collinear sea height profiles derived from the NAG orbits placed on the GDR's are plotted in Figure 3.5. This Figure shows that the CSR sea surface profiles are more

consistent to each other than the NAG profiles. There is an apparent long wavelength radial orbit bias between these two data systems of about 4 m. This bias is due to the errors in the realization of the Earth's mass center for the reference coordinates used to compute the NAG orbit. Figure 3.6 is a gray-tone image of the large systematic radial orbit difference between the CSR orbit and NAG orbit based upon a 17-day arc in a global scale. White color indicates that the CSR radial orbit is 10 meters higher than the NAG orbit, while the black color indicates that the CSR radial orbit is 4 meters lower than the NAG orbit. Because large data gaps in the polar regions, there are many areas filled in gray color represent the missing data areas. The sea surface derived from CSR orbit is generally higher in southern hemisphere and lower in the northern hemisphere. The radial bias between these two orbits is 3.32 meters over the world oceans. This difference is primarily due to a bias in the z-axis between these two reference coordinate systems.

Two repeat cycles of Geosat profiles from 56 orbital revolutions ( $2.2 \times 10^9$  m) were used to estimate the radial accuracies of the CSR and NAG orbits. The rms of profile differences reveals the total error while the spectrum of the profile differences reveals peaks in the orbit spectrum. Figure 3.7 shows the ground tracks of Geosat profiles used for this orbit error analysis. The rms differences between the sea surface height derived from CSR orbit and NAG orbit is 4.66 meters. The spectrum of the radial differences presented on Figure 3.8 shows that the primary peak amplitude is about 4.8 meters at wavelength 40,000 km (once per rev) and a secondary amplitude peak of 1.2 meters occurs at 20,000 km wavelength (twice per rev). Rms differences between two collinear CSR sea surface profiles is 16 cm and the amplitude spectrum of the collinear altimeter profile differences between two CSR profiles shown on Figure

3.9 is almost white. The largest peaks with amplitude less than 3 cm over a broad range indicate that once per rev long wavelength radial orbit error has been removed effected from the CSR orbits. The rms differences between the same two NAG sea surface profiles is 137 cm. Figure 3.10 shows the amplitude spectrum of NAG altimeter collinear profile differences. Once per rev radial orbit error of 1.2 m can be found clearly in this plot. At wavelengths shorter than 10,000 km, the amplitudes are less than 20 cm. Thus, the long wavelength radial orbit errors contained in the GDRs can be handled for extracting the mesoscale variability from these collinear altimeter profiles.

### 3.9 Summary

Although the absolute orbit accuracy cannot be directly estimated, the range rate and crossover residuals do give an indication of the quality of the CSR Geosat ephemeris produced using the Tranet data. The average range-rate residual rms of about 0.65 cm/s for 17 day arc lengths was near the average noise level of 0.5 cm/s predicted by the navigation solution, indicating excellent fits for arcs of these lengths.

Average crossover residual rms of about 35 cm can be used to evaluate the total radial orbit accuracy. However, crossovers can only measure the variable part of the orbit error since geographically correlated error, such as that due to gravity mismodeling, will cancel out in the crossover difference. The analytical spatial expression for the radial orbit perturbations due to the geopotential given in Eq. (2.5) shows that the two quantities, i.e. the regional mean part and the variable part are in the same order of magnitude but are only  $90^\circ$  out of phase in longitude. If it is assumed

that the crossover variance is the sum of the radial orbit error variance of the ascending and descending passes from which the crossover was calculated, then the crossover variance is approximately twice the radial orbit error variance. Thus, the variable part of the radial orbit error is the crossover residual rms divided by the square root of 2. Since the mean part of the radial error is nearly equal to the variable part in magnitude, and root sum squaring the mean and variable radial errors globally, the resulting radial orbit accuracy is the same as the residual crossover rms. If gravity model error is considered to be the dominant source of orbit error, the crossover variance should reflect the overall radial orbit error variance. In the case of the collinear altimeter profile differences, the collinear residual rms has been found to be smaller by a factor about 2 than the crossover residual rms because both the regional mean and variable parts of radial orbit error due to the perturbations of geopotential are unobservable.

Based on the discussion above, a conclusion can be made that the CSR orbit has achieved the relative radial orbit accuracy of about 35 cm. This conclusion was determined from the evaluation of three 17-day arcs crossover residual rms which reflect the variable part of radial orbit error due to geopotential coefficients error of PTGF3A gravity field. The result also agrees with the predicted Geosat radial orbit error rms of 35 cm by a preliminary calibrated covariance matrix of PTGF3A gravity model (Figure 3.11). While the CSR collinear altimeter profile difference rms is about 16 cm and the once per revolution orbit error has been removed effectively. On the other hand, the NAG orbit which is supplied with the GDRs produced a 3.38 m rms crossover residual over a 17-day period. The collinear altimeter profile difference rms is 1.37 meters and its spectrum shows a peak amplitude of 1.2 m at a frequency of once

per orbital revolution. Relatively small collinear altimeter profile errors (amplitude < 20 cm) at wavelengths shorter than 10,000 km make the Geosat ERM GDRs especially valuable for the study of mesoscale variability.



GEOSAT (1/7 - 1/25, 1987) CROSSOVERS (18395)

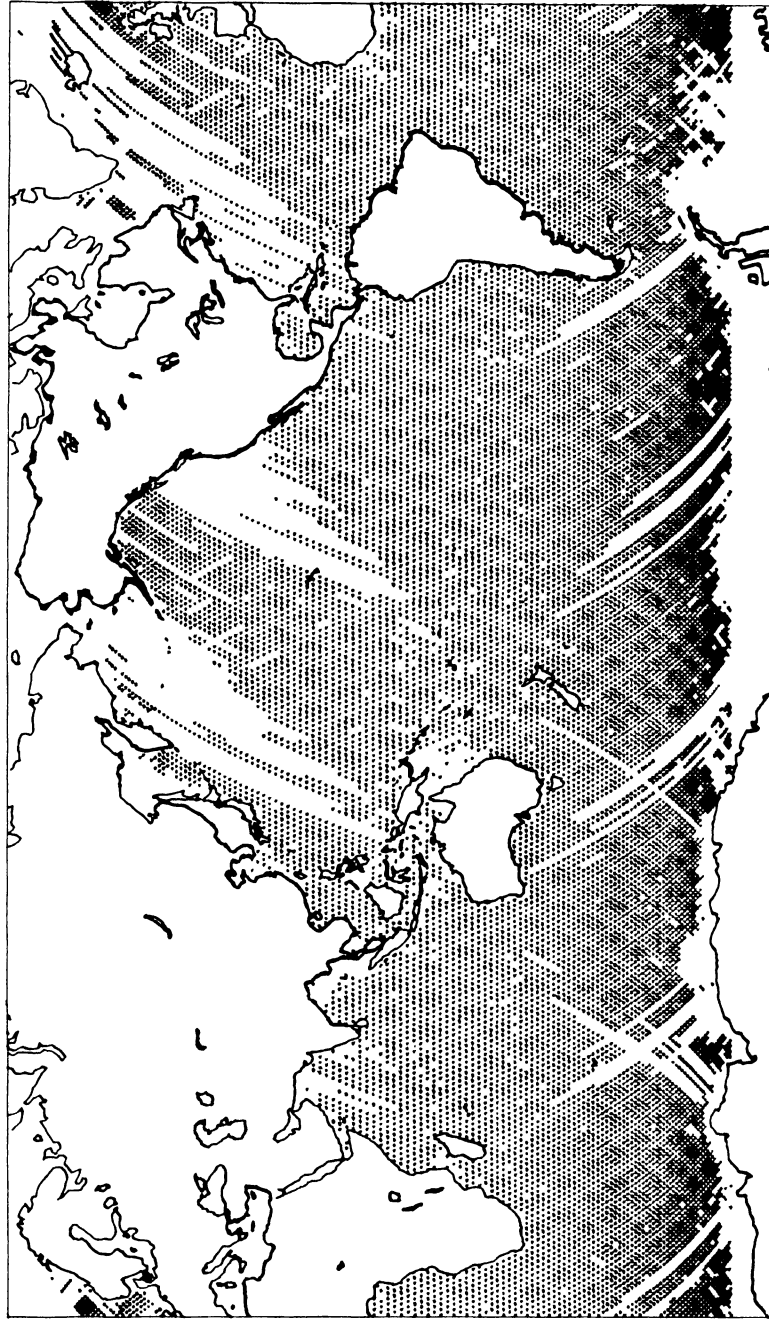


Figure 3.4 Geosat Altimeter Crossovers for a 17-day Arc (18395 points)  
Crossover rms Residuals : 32 cm (CSR orbit), 338 cm (NAG orbit)

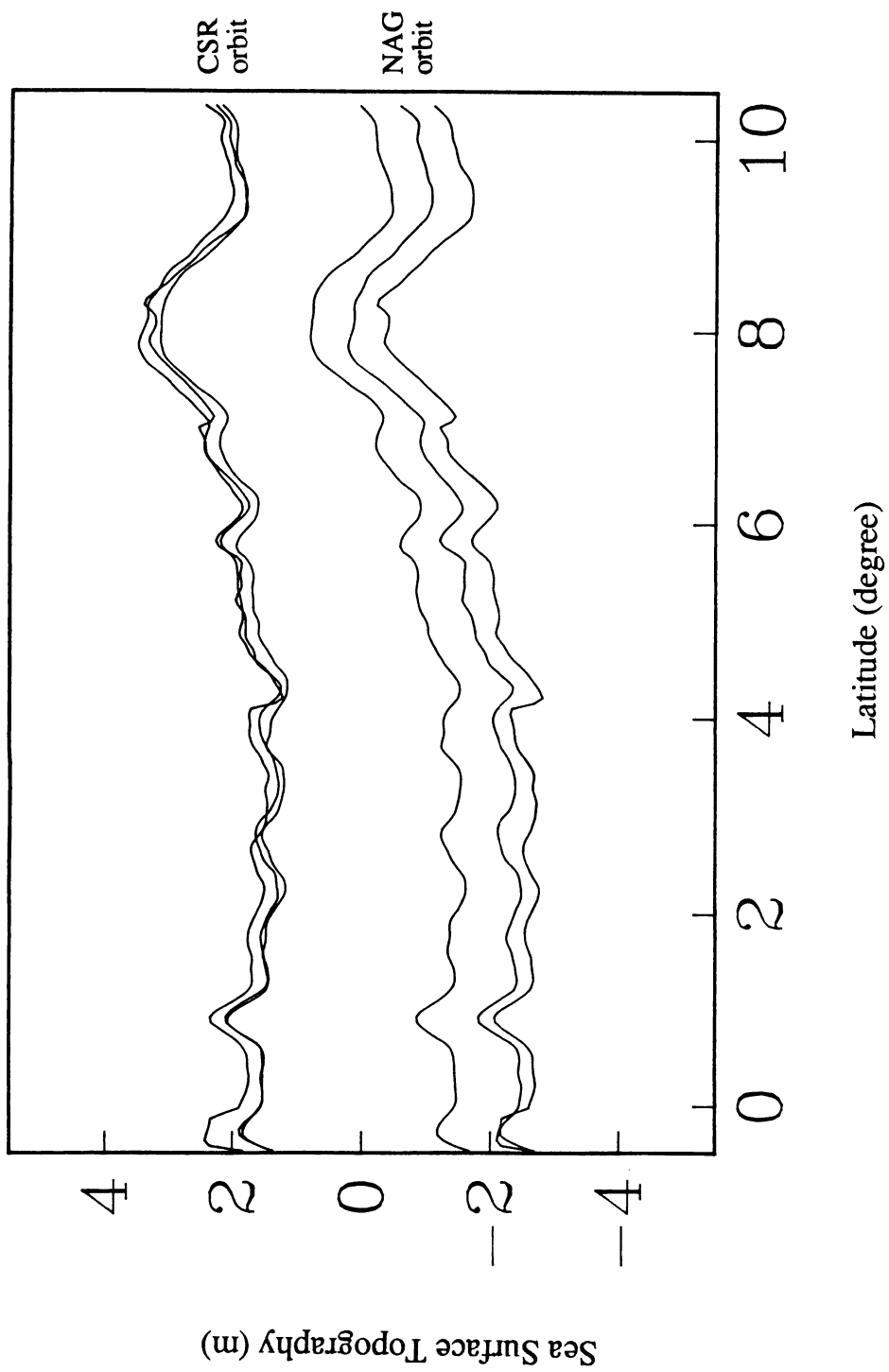


Figure 3.5 CSR/NAG Collinear Altimeter Profiles

Bias = 3.32 m  
 RMS = 3.7 m

+10 m

-4 m

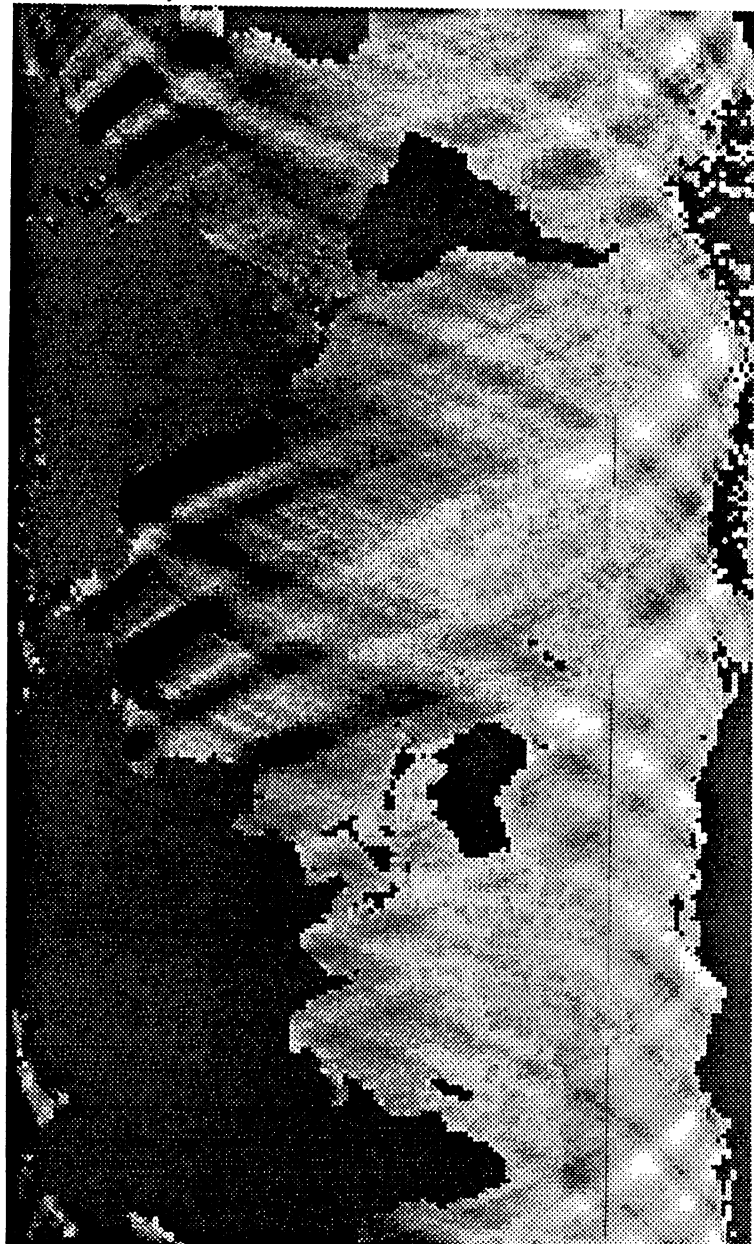


Figure 3.6 Gray tone scaled radial orbit differences of CSR - NAG orbits

$\sim 4.8 \sin \theta - 3.32 \text{ m}$  parameter shift in final plot  
 $4.5 \sin \theta - 3.823 \text{ m}$  shift inside in orbit

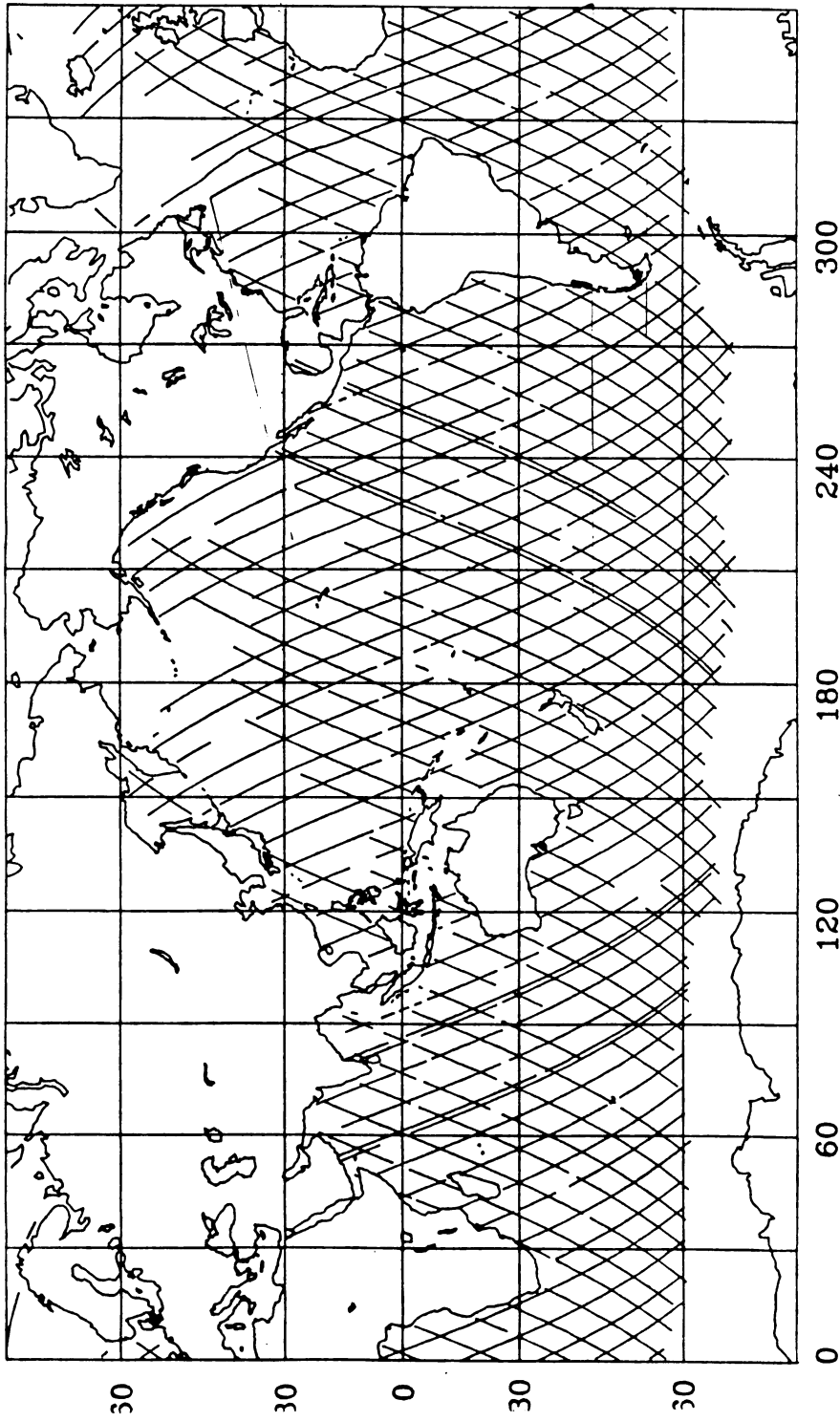


Figure 3.7 Ground tracks for orbit collinear altimeter profiles evaluation

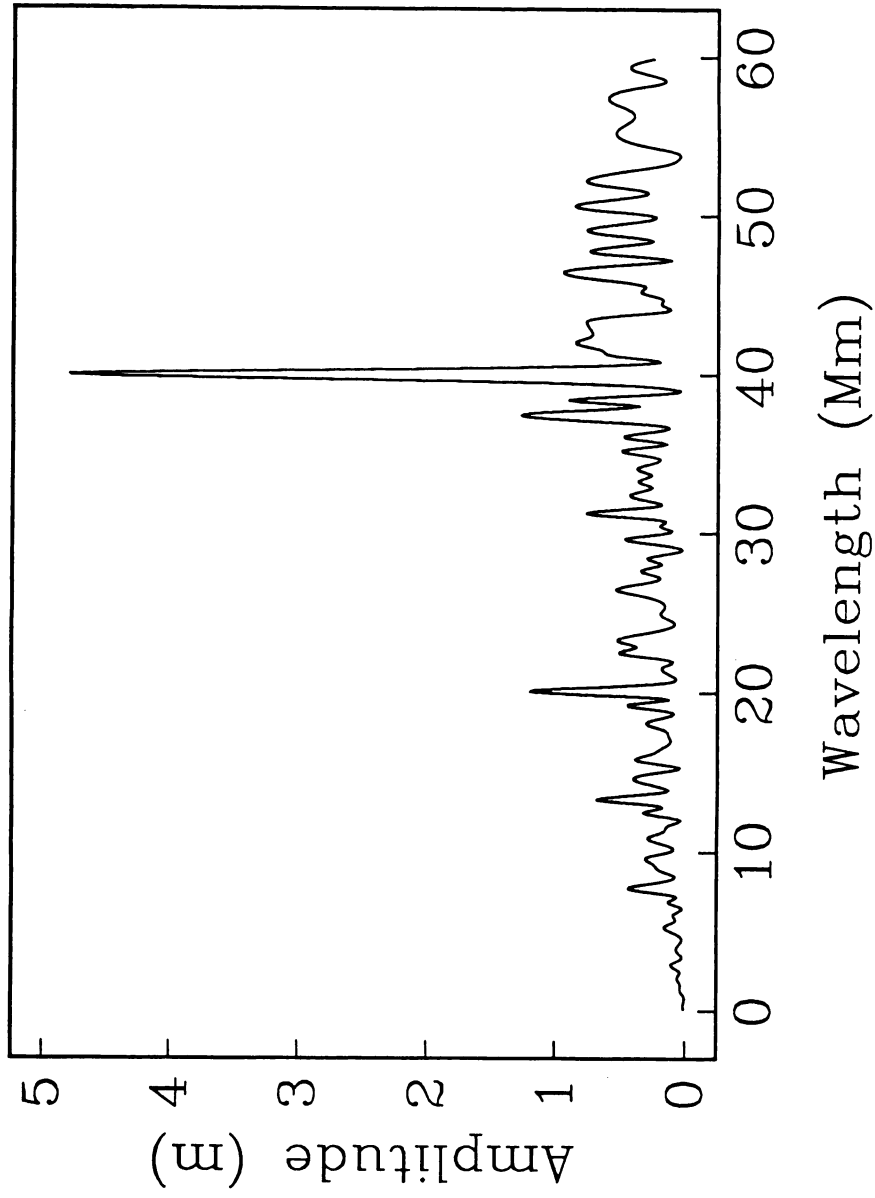


Figure 3.8 Spectrum of the radial orbit difference of CSR - NAG

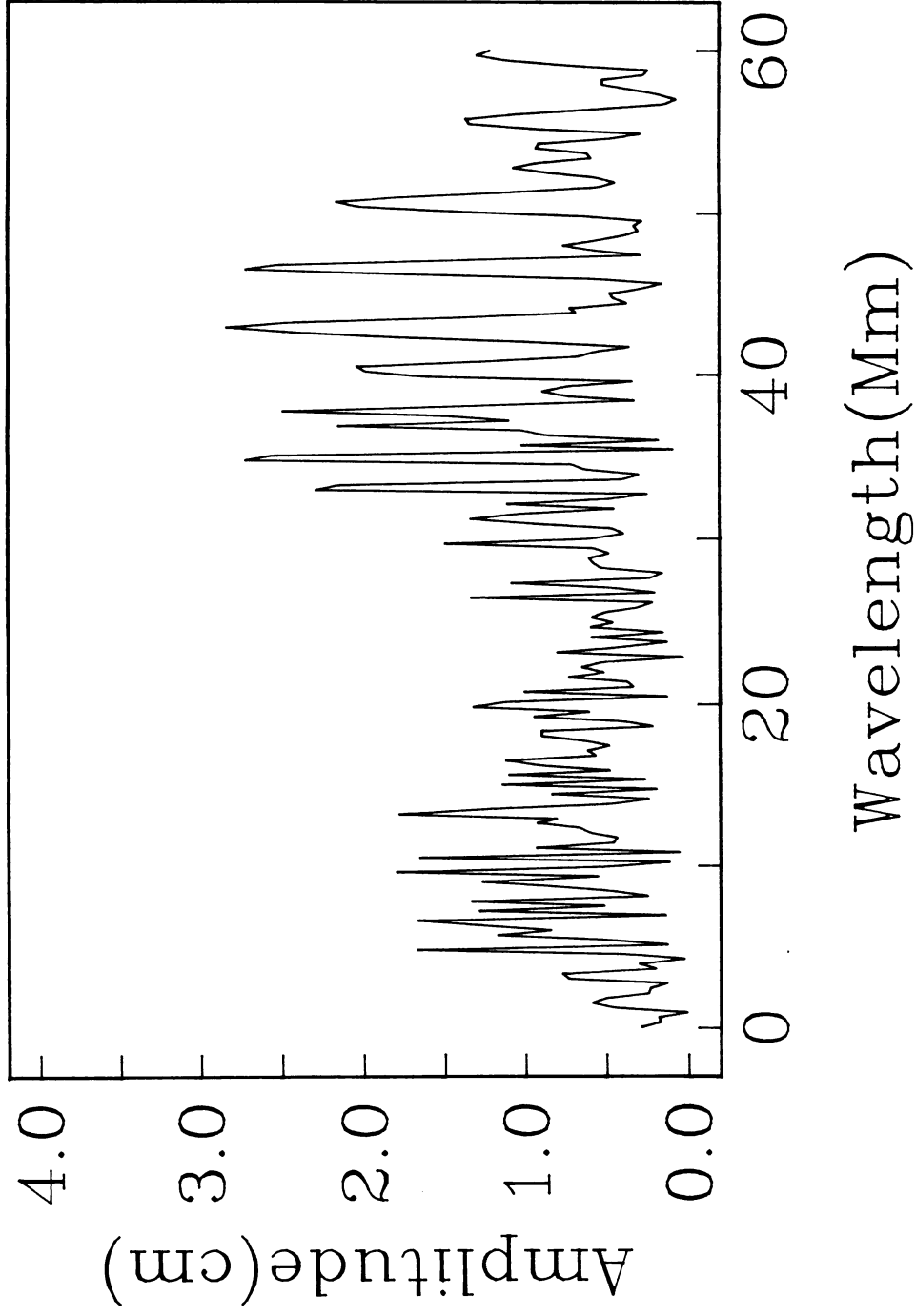


Figure 3.9 Spectrum of the difference between two CSR collinear altimeter profiles

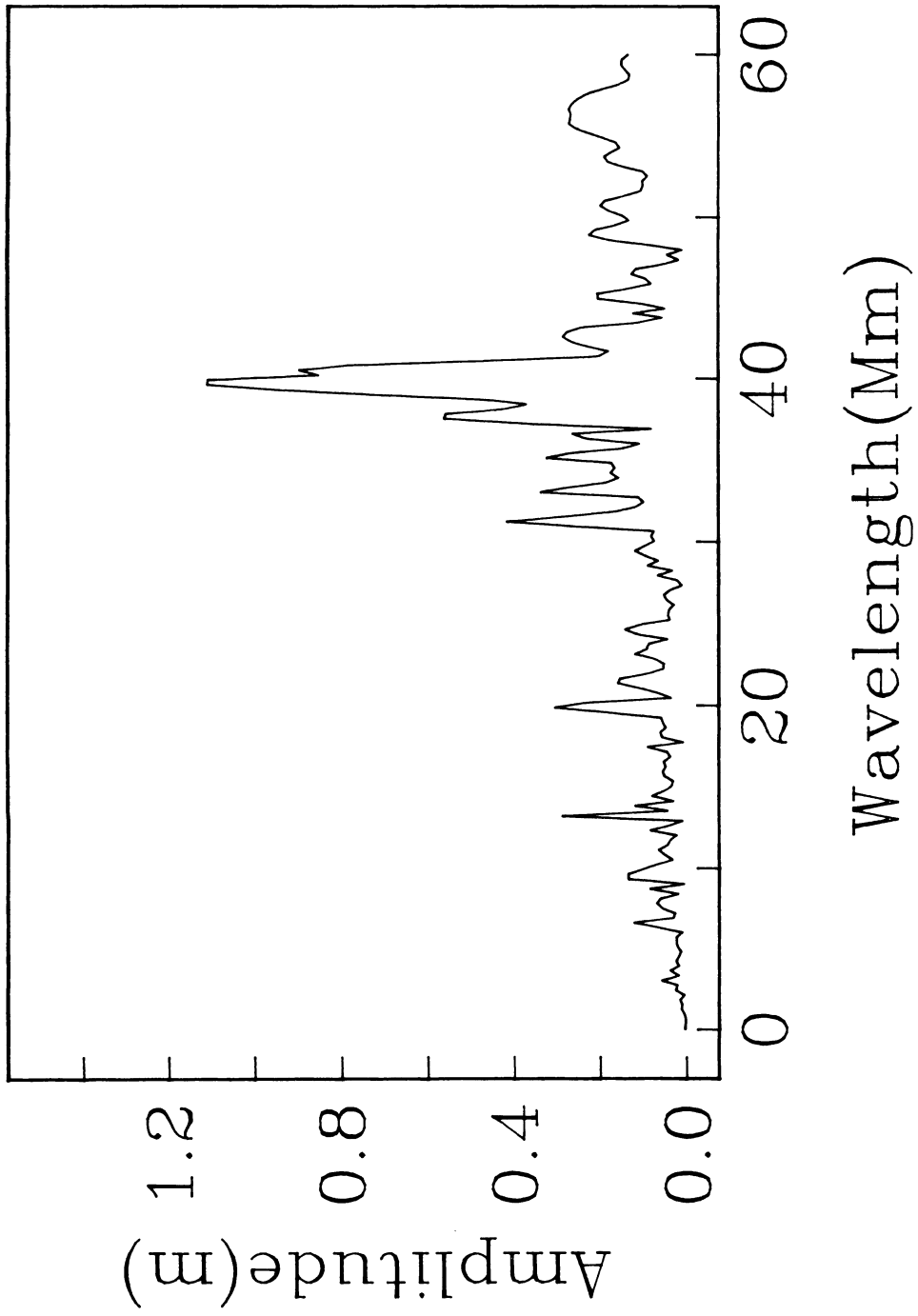


Figure 3.10 Spectrum of the difference between two GDR collinear altimeter profiles

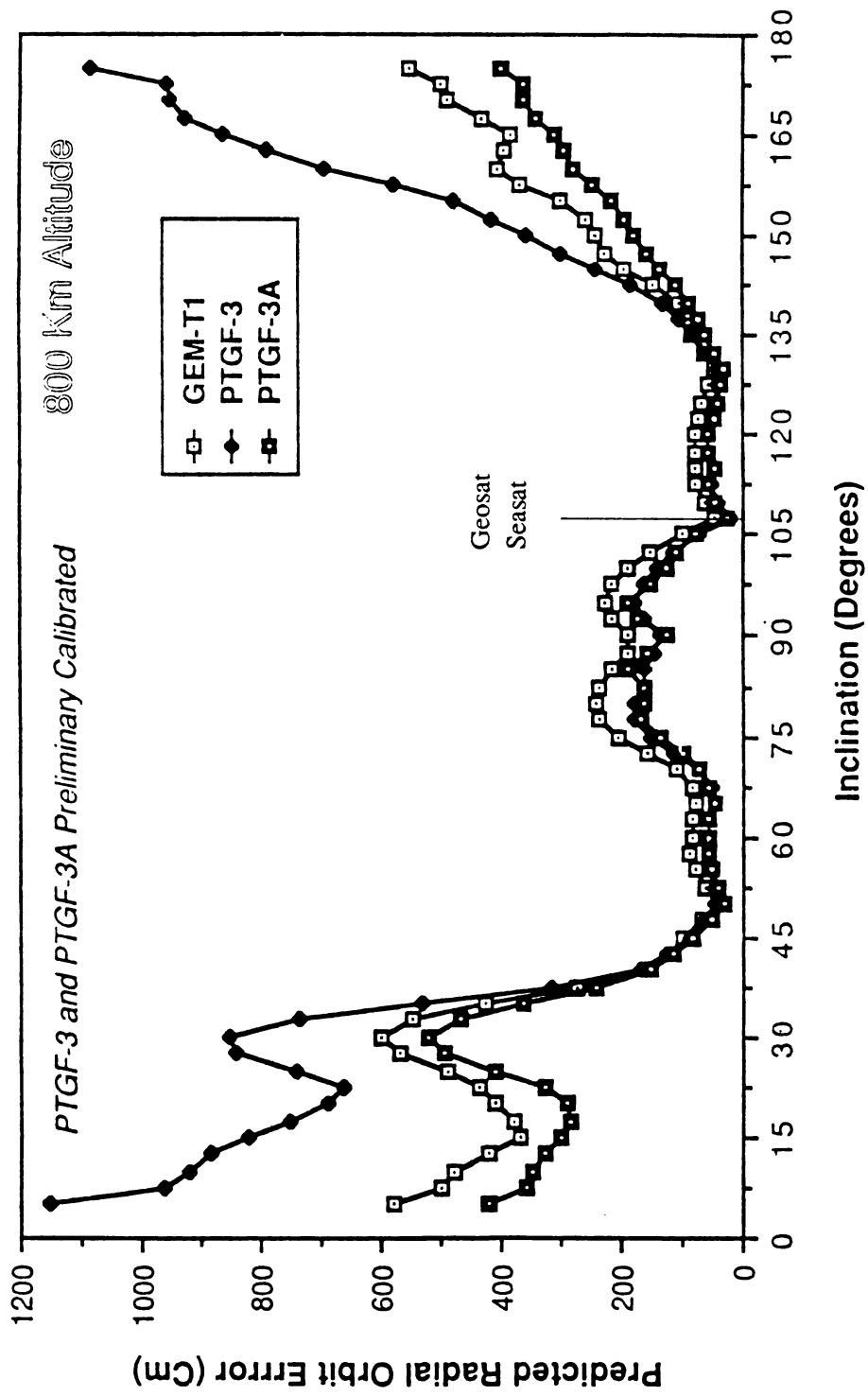


Figure 3.11 Predicted Geosat radial orbit error From Gravity Covariance Matrices



## Chapter 4

### Global Mesoscale Variability From Geosat ERM

#### 4.1 Introduction

Satellite altimetry is becoming an important tool for acquiring global, synoptic measurements of the dynamic topography of the oceans associated with currents, eddies and equatorial waves [Fu, 1983a]. However, to determine the geostrophic circulation at both mesoscales (100 ~ 1,000 km) and basin scales (1,000 ~ 10,000 km), the slope of the sea surface (relative to the geoid) must be measured to an accuracy of 0.1  $\mu$ rad or better [Stewart et al., 1986]. This slope accuracy corresponds to 10 cm accuracy (or better) topography measurement over a distance of 1,000 km. Such high accuracy data is not yet available from the Geos-3, Seasat or Geosat altimeter missions. The current limitations [Tapley et al., 1982a] are the radial orbit error, tide model errors, atmospheric delay error and electromagnetic bias. Moreover, the largest uncertainties in determining absolute dynamic topography are due to inaccuracies in the global geoid models. Thus, both the altimeter measurements and the global geoid models must be substantially improved before global dynamic topography can be measured synoptically. The Topex/Poseidon mission, 1991 launch [Born et al., 1984], may achieve the high accuracy topography measurements. Geoid models with similar high accuracy may be achieved from a space-borne gravity gradiometer mission [Gravity Workshop, Colorado Springs, 1987] or from improved tracking of low-altitude, low-drag satellites.

While the current altimeter data are not accurate enough to measure absolute

dynamic topography over basin scales, they are sufficiently accurate for mapping mesoscale (100 - 1000 km) variations in dynamic topography. There are two reasons why mesoscale variability can be measured with relatively inaccurate altimeter data. First, as shown below and in previous studies, the error in the altimeter profiles primarily consists of wavelengths greater than 10,000 km. Second, the sea surface slope associated with mesoscale variability are relatively large ( $> 1 \mu\text{rad}$ ). By applying a simple along-track derivative method to Geosat altimeter profiles, the signal to noise ratio for some mesoscale features is about 50; slope variations as low as  $0.2 \mu\text{rad}$  can be detected.

The techniques for extracting mesoscale variability from satellite altimeter measurements are well established [Fu, 1983a]. The methods involve the removal of long-wavelength orbit error and long-wavelength dynamic topography, and then the removal of the time-invariant geoid and steady state ocean circulation components of sea surface topography. These methods have been applied to the 3.5-year Geos-3 and 3-month Seasat data sets to determine the statistics of global mesoscale variability.

The simplest method is the "collinear track method" where profiles of mesoscale variability are obtained from repeated altimeter profiles along the same satellite ground track. The repeat profiles are first averaged together. The average profile consists of the geoid, the time invariant dynamic topography and the average of all of the long-wavelength errors. Individual profiles are then subtracted from the long-term average. Finally, the long-wavelength error (mostly orbit error) is reduced by removing a linear or quadratic polynomial from each profile. The residual profiles reveal variations in sea surface topography (over the averaging time interval) having wavelengths less than  $\sim 2000$  km. For example, despite the relatively low accuracy of the Geos-3

measurements, several groups of investigators [Douglas and Gaborski, 1979; Cheney and Marsh, 1981a; Douglas et al., 1983] were able to measure the relatively high-amplitude mesoscale variations of Gulf Stream meanders and eddies using this repeat profile method.

A similar technique was applied to Seasat altimeter data on a global basis [Cheney et al., 1983]. Because of improvements in altimeter design, atmospheric delay corrections and orbit precision, Seasat revealed previously unknown spatial details in the mesoscale variability of the oceans that are generally consistent with historical data [Wyrтки et al., 1976]. One of the surprising results from the analysis of Seasat data was that over most ocean areas the mesoscale variability is quite low ( $< 4$  cm). The smaller areas of high variability are associated with western boundary currents and the Antarctic Circumpolar Current.

In addition to mapping the global rms mesoscale variability, residual Seasat profiles were used to track time varying mesoscale features (e.g., Cheney and Marsh, 1981b) over the short 3-day repeat cycle of Seasat. While Seasat's 3-day repeat ground track had good temporal resolution, its spatial resolution (i.e.  $\sim 700$  km ground spacing) was sometimes inadequate for tracking small eddies. A mesoscale eddy detected along a single Seasat ground track eventually drifted to the region between ground tracks. The Geosat altimeter, which has been collecting altimeter data along a 17-day repeat cycle for approximately 1.5 years [Cheney et al., 1987a], has better spatial resolution ( $\sim 165$  km) but the increased repeat interval results in poorer temporal resolution.

Papers describing the Geosat altimeter mission and the accuracy of the Geosat

altimeter data can be found in the *Johns Hopkins APL Technical Digest* [1987] and a brief description of Geosat Exact Repeat Mission was given in Chapter 1. To date, this Geosat/ERM has completed about 40 cycles having ground tracks that repeat to within a 1 km band crosstrack. One of the more remarkable results from these data is a sea level time series over a large region of the Equatorial Pacific showing the propagation of a Kelvin wave associated with the 1986-1987 El Nino [Cheney et al., 1987b; Miller et al., 1987]. Sea surface slopes associated with this Kelvin wave range from only 0.04  $\mu$ rad to 0.1  $\mu$ rad. Despite the very low amplitude topography of this feature, the Geosat results show agreement with island tide gauges, inverted echo sounders and thermistor chains [Cheney et al., 1988]. In this chapter, the analysis of Geosat/ERM altimeter data for mapping the larger amplitude features (0.1 - 10  $\mu$ rad) of sea surface slope variability over all ocean areas including the shallow seas is the primary interest.

A simple numerical derivative high-pass filter technique [see Appendix] has been developed for extracting mesoscale variability from satellite altimeter data having large-amplitude (~3 to 4 m) and long-wavelength (> 10,000 km) errors; no data adjustments are necessary. This method was then applied to the first year (22 repeat cycles) of Geosat/ERM data. The derivative high-pass filter that was adopted for this study has several advantages over previous filter methods (e.g. removing linear trends from 2000 km long altimeter profiles). The main advantage is that the derivative filter is only 2 points long so that it produces no edge effects. In contrast, the removal of a tilt and bias from 2000 km long segments will produce artificial undulations up to 500 km from the ends of each profiles. These edge effects are most apparent on the Falkland plateau where published maps (e.g. Figure 4.1, [Cheney et al., 1983]) show high variability

**SEASAT ALTIMETER  
MESOSCALE VARIABILITY**

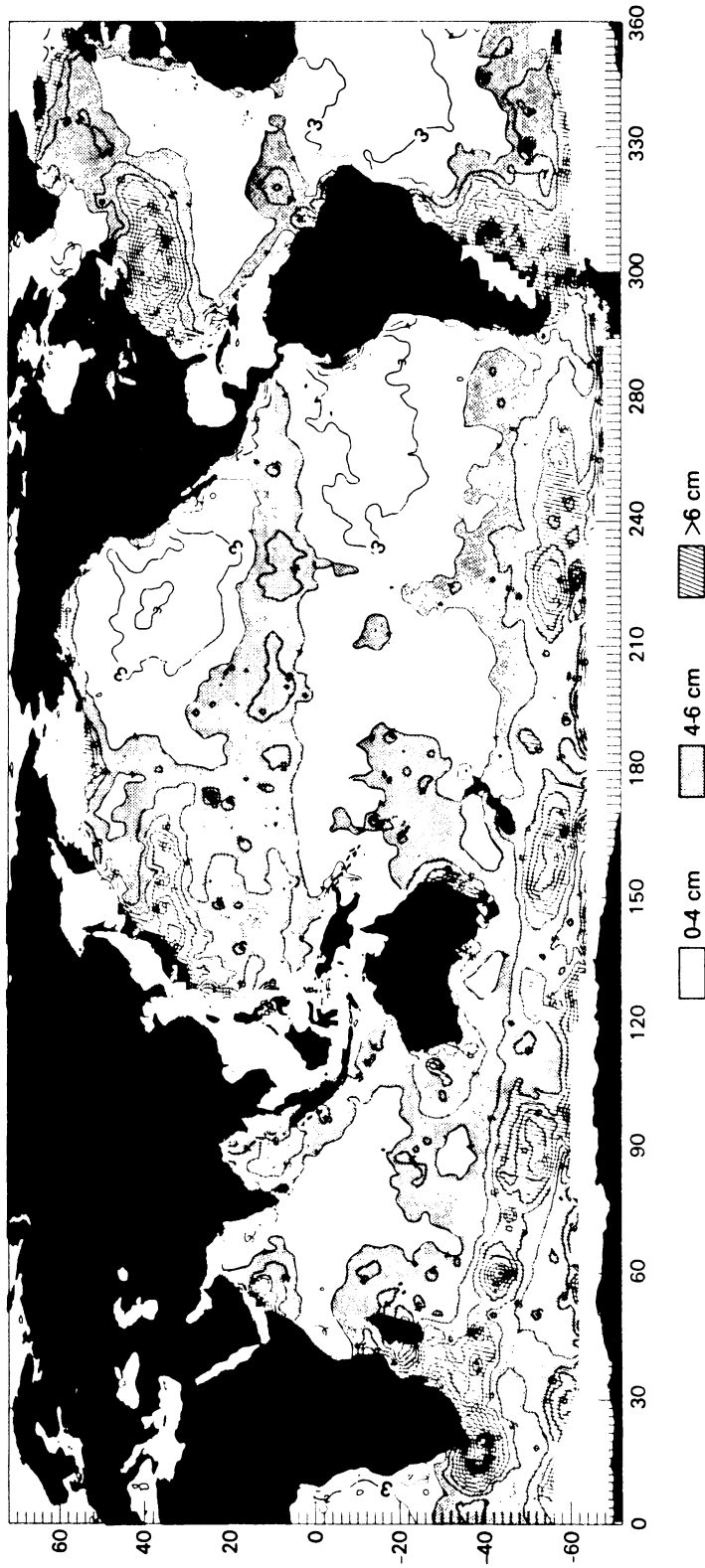


Figure 4.1 Seasat Altimeter Mesoscale Variability [Cheney et al., 1983]

and this analysis shows low variability. The tilt and bias method interacted with the high variability north of the Falkland Plateau causing the leakage of the variability toward the ends of the profiles. The second advantage of the derivative filter is that it transforms a height profile into a slope profile. The slope of the sea surface (i.e. the difference in dynamic topography at two points) is a parameter that can be measured independently. Moreover, if the ocean is in geostrophic balance, then the gradient of the sea surface is proportional to the current velocity. There is also a simple relationship between sea surface slope variability and eddy kinetic energy [Menard, 1983].

Douglas et al. [1984], Sandwell et al. [1986] and Tai et al. [1986] have recently suggested an improved method of orbit error removal over the conventional "bias and tilt adjustment". In their approach, the radial orbit error of each satellite orbit is estimated globally (rather than regionally over areas a few thousands kilometers on a side) by representing the orbit error as a Fourier series in time. They have shown that the Fourier series representation is preferable because it does not suppress ocean variability with spatial scales less than the shortest wavelength of the Fourier series. It also produces smaller edge effects and forces ascending and descending profiles to agree at crossover points. In comparison with the derivative filter method, the Fourier series method may yield more accurate basin-scale variability but similar mesoscale variability. This simple derivative method has been applied to 180 million new Geosat observations (10/s) for this mesoscale variability study.

## 4.2 Data Processing and Analysis

### 4.2.1 Pre-processing

The first 22 repeat cycles of the Geosat Geophysical Data Record (GDR) altimeter data from Nov. 7, 1986 to Nov. 16, 1987 were used in this analysis. Each once per second GDR includes the following quantities: ten sea surface height measurements, the average of the 10 measurements, the standard deviation of the average, environmental corrections and pre-processing flags [Cheney et al., 1987]. Based on the previous experience with Seasat altimeter data [Cheney et al. 1983; Marsh et al., 1982], the following editing criteria were first applied to the GDR's:

- standard deviation ( $\sigma$ ) of 1 per second average exceeding 10 cm;
- Automatic Gain Control (AGC) greater than 34 db or less than 15 db;
- Significant Wave Height (SWH) greater than 8 m;
- data over land or ice;
- flagged data considered to be bad;

This editing eliminated about 4% of the data (see Table 4.1).

Instead of using the 1 per second average heights, the 10 per second observations were averaged into twice per second observations. This increased sampling rate retains more of the short-wavelength information needed for interpolation and removal of the high-amplitude, short-wavelength geoid undulations (see below). Moreover, the average of many repeat cycles is used for geophysical studies where the short-wavelength information is desired. The following corrections (supplied with the GDR's) were then applied to the 2 per second data: ocean tides (Schwiderski), solid

earth tides (Cartwright), ionosphere delay and the troposphere delay (both dry and wet components from FNOC). After applying the corrections the data were divided into ascending or descending passes depending on the orientation of the satellite velocity with respect to the Earth. The passes were further subdivided whenever a time gap exceeded 10 seconds. The histogram of Geosat ERM altimeter data is presented in Figure 4.2.

Table 4.1 Summary of Altimeter Data Editing for  
Three 17-day Geosat ERM arcs

Editing Criteria	Arc 1	Arc 2	Arc 3
	11/17/86 - 12/4/87	12/21/86 - 1/7/87	1/7/87 - 1/25/87
sigma >10 cm	3149	3383	3346
AGC > 34 db	4070	4200	3647
AGC < 15 db	0	3	1
SWH > 8 m	1275	1417	1570
Land/Ice	0	0	0
Flagged	9274	8350	52035
# of data edited	17768	17350	60598
# of data after editing	732890	771284	736112
% of data edited from 2337832 raw data points = 4.09 %			

#### 4.2.2 Orbit Error Analysis

The major limitation in using Geosat/ERM data for measuring dynamic topography is its significant long-wavelength error (mostly radial orbit error). The Geosat/ERM orbit was computed by the Navy Astronautics Group (NAG) using the



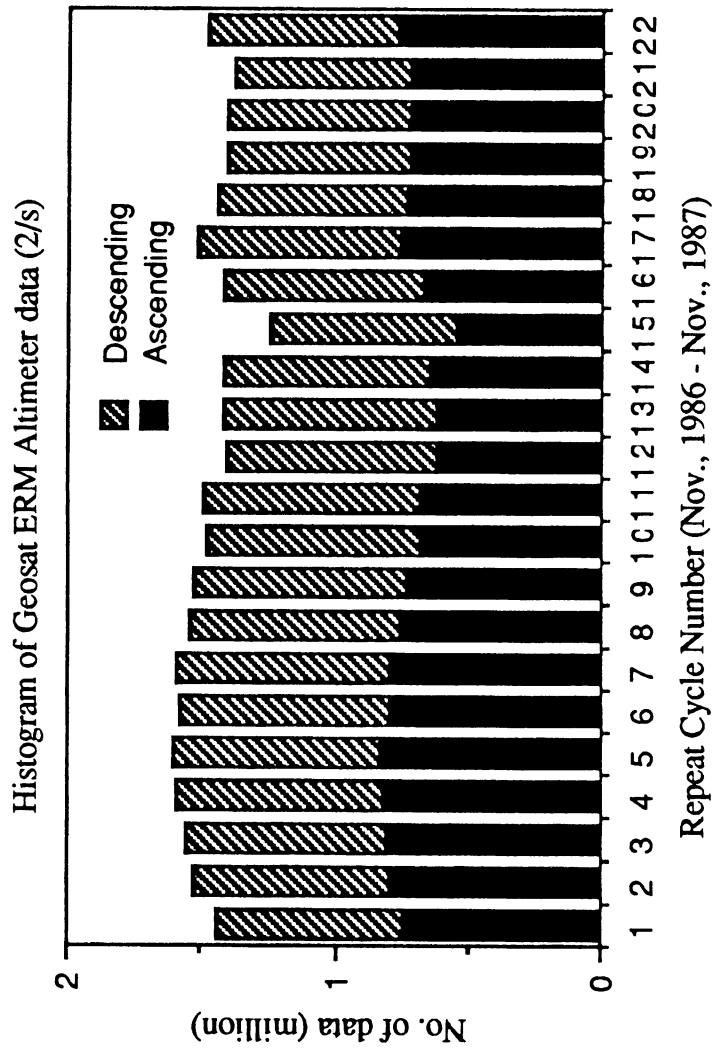


Figure 4.2 Histogram of Geosat ERM altimeter data

GEM-10B gravity model [Lerch et al. 1981] and doppler tracking data from the four Transit OPNET tracking stations (all in U.S.). Because of gravity model errors and the poor geometry of the tracking network the radial orbit error is quite large ( $\sim 4$  m crossover rms) and dominated by a frequency of once per orbital revolution (40,000 km wavelength).

To illustrate this orbit error, three ascending Geosat repeat profiles across the Northwestern Pacific are shown in Figure 4.4a (track labeled A-A' on Figure 4.3). Two different orbits were used to calculate the sea surface topography profiles (Figure 4.4a), the first was the standard NAG orbit and the second was the CSR orbit computed using a new global gravity model PTGF3A as well as 80 days of Tranet doppler tracking data from a global network of 48 stations [Chapter 3]. The differences between the NAG profiles and the CSR profiles are large ( $\sim 4$  m) and it is a good measure of the magnitude of the radial error in the NAG orbit. In addition to the large differences between the NAG profiles and the CSR profiles there are smaller differences among the 3 profiles having common orbit type. This smaller, relative orbit error is  $\sim 1.5$  m rms for the NAG profiles and  $\sim 0.16$  m rms for the CSR profiles [see Chapter 3]. When the absolute dynamic topography is measured with a satellite altimeter, the absolute radial orbit error limits the accuracy of the measurements. Similarly, when changes in dynamic topography are measured, the accuracy is limited by the relative orbit error. The profiles shown in Figure 4.4a suggest that the Geosat/ERM profiles will be best for variability studies where changes in dynamic topography are measured. The relative collinear orbit error rather than the absolute orbit error is important for mesoscale variability studies because profile differences are involved.

To determine the amplitude and dominant wavelength of the absolute NAG orbit error, the amplitude spectrum of the difference between the NAG profiles and the CSR profiles has been computed for 56 orbital revolutions of data. Since there are numerous large gaps in the data associated with the continents, a least squares technique was used to fit the sine and the cosine components one frequency at a time. The spectrum (Figure 3.8) has a peak of about 5 m at a wavelength of 40,000 km which corresponds to a frequency of one cycle per revolution. A second smaller peak occurs at a wavelength of 20,000 km (twice per revolution). The amplitude spectrum decreases for wavelengths less than 10,000 km suggesting that the absolute orbit error is small at short wavelengths. With such large radial orbit error, unadjusted Geosat/ERM data are useless for all types of oceanographic studies since dynamic topography is generally less than 2 m.

One way to suppress the long-wavelength orbit error, without adjusting the data, is to take the along-track derivative of each profile. As shown in Figure 4.4b, differentiation suppresses much of the long-wavelength geoid undulation as well as the long-wavelength radial orbit error. In the wavenumber domain, the derivative corresponds to multiplying the spectrum by  $2\pi j/\lambda$  where  $\lambda$  is the wavelength. Long-wavelengths are suppressed while short wavelength are enhanced; the imaginary factor  $j$  shifts the phase of the signal by  $90^\circ$ . Figure 4.5 (light curve) shows the slope error spectrum for the NAG profiles minus the CSR profiles. The slope spectrum has a peak of  $\sim 0.8 \mu\text{rad}$  at a wavelength of 40,000 km and smaller peak of  $\sim 0.2 \mu\text{rad}$  at 20,000 km wavelength. These results suggest that the absolute slope of the sea surface can be measured to an accuracy of  $\sim 1 \mu\text{rad}$  (i.e. 1 m over 1000 km) using Geosat/ERM data. In some energetic areas of the oceans, the dynamic topography slope is 3-8

$\mu\text{rad}$ . Thus, the simple differentiation procedure transforms data that are useless for ocean circulation studies into data that are marginally useful for these studies. However, for basin-scale circulation studies the absolute errors in Geosat/ERM data are still 10-100 times too large.

The situation is greatly improved when unadjusted Geosat/ERM slope profiles are used for mesoscale variability studies. This is because the relative error in the NAG orbit is smaller than the absolute error, especially at a wavelength of 40,000 km (once per revolution). Much of the error in the NAG orbit is caused by errors in the GEM-10B gravity model. These errors repeat geographically and thus are common to collinear profiles [Chapter 3]. To determine relative slope error, the spectrum of the difference between the second Geosat/ERM repeat cycle and the average of the 22 repeat cycles has been calculated. The amplitude spectrum for 71 orbit revolutions is shown in Figure 4.5 as a heavy line. In general, the relative error in the NAG slope spectrum is about 5 times less than the corresponding absolute error. A broad, low amplitude peak in the relative slope spectrum ( $0.14 \mu\text{rad}$ ) occurs at a wavelength of 40,000 km. At other wavelengths, the relative error is less than  $0.05 \mu\text{rad}$ . These results show that the relative error among repeat Geosat/ERM slope profiles is only 0.1 to  $0.2 \mu\text{rad}$ . In other words, a 0.2 m change in sea surface topography over a distance of 1000 km can be measured with Geosat/ERM data without adjusting the data.

#### 4.2.3 Averaging, Differencing and Filtering

After editing, applying corrections and differentiating the profiles, all 22 repeat cycles ( $\sim 32$  million 2/sec observations) were loaded into two compact files, one for

the ascending profiles and the other for the descending profiles. Each file has 244 columns representing the 244 equator crossing and 7000 rows representing the possible number of twice per second samples in a complete ascending or descending arc (Figure 4.6). A third dimension was used to store the 22 repeat cycles. Pre-processed passes were interpolated onto the uniform along-track bins and placed into the file. Because the data were over sampled slightly (i.e. 2 points per second), a linear interpolation scheme could be used after the data were low-pass filtered (15 km cutoff wavelength). To avoid storing latitude and longitude information, simple formulas were used to map the record position in the file into geodetic latitude and longitude and vice versa; profiles were assumed to be collinear. After all of the data were loaded into the file, the slope were averaged, when more than 6 repeat cycles were available, to compute a mean slope profile. To remove remaining outliers, individual slopes were compared with the average. If an individual slope was more than 5 standard deviations from the average, then it was edited and the average was recomputed. This procedure removed 0.8% of the data. The average profile was extracted for marine geophysical studies.

The final step in the processing was to low-pass filter the profiles. This is necessary because the derivative filter enhances the very short wavelength altimeter noise. The noise become most apparent when 22 repeat profiles are averaged together and then the individual profiles are subtracted from the average (Figure 4.7). The 22 differenced profiles on the bottom of Figure 4.7 were low-pass filtered using a Gaussian filter [see Appendix] with half amplitude filter width  $\sigma = 1$  s (corresponds to a cutoff wavelength of 30 km). Increasing the filter length reduces the short wavelength altimeter noise and reveals the mesoscale variability of the Kuroshio Current as well as the low variability at 10°N latitude. After examining data from many

areas, a 5 second ( $\sigma = 5$  s) filter length was adopted (175 km half amplitude cutoff wavelength). As shown by Fu [1983b] the mesoscale variability has very little power at wavelengths less than 250 km. To avoid possible edge effects caused by the low-pass filter, 15 seconds of data (i.e. 100 km) were eliminated from the ends of the profiles.

The repeat profile method assumes that the profiles are collinear. If they are not, then crosstrack geoid gradients can introduce false signals in the differenced profiles. The amplitude of the false signals is equal to the cross-track gradient times the spacing between profiles. Geosat ERM repeat profiles lie within a  $\pm 500$  m band. The largest geoid gradients are associated with oceanic subduction zones. For example, the Kurile Trench (Figure 4.4b at  $48^\circ - 50^\circ$  N) has a geoid gradient of about  $200 \mu\text{rad}$ . The expected amplitudes of false signals above the Kurile trench are about 0.1 m. In terms of slope, this corresponds to  $\sim 5 \mu\text{rad}$ . As expected, these false signal are seen in the difference profiles (Figure 4.7) at the location of the Kurile trench. All ocean trenches have the large geoid gradients and thus one must be careful when interpreting mesoscale variability in these areas.

### **4.3 Slope Variability**

#### **4.3.1 Slope Difference Profiles**

The variability apparent in the slope difference profiles ranges in amplitude, wavelength and cause; most but not all of the variability is due to oceanography. To illustrate this variety of signals and their different sources, 22 slope difference profiles

along 7 long satellite passes (Figure 4.8, Profiles A-G) have been plotted for examination. The locations of these 7 profiles are marked on Figure 4.3 as A to A' etc. For Example, the ascending profile A crosses the Western Pacific in a northwest direction and corresponds to the profiles in Figures 4.4 and 4.7. All 22 repeat profiles are plotted together along the lowest edge of the figure and then they are plotted individually moving up from the bottom of the figure. Two areas of higher variability are apparent in the slope difference profiles A; one is between  $-30^{\circ}$  and  $-20^{\circ}$  latitude and the other area is between  $30^{\circ}$  and  $40^{\circ}$  latitude (i.e. Kuroshio Current). Data gaps, associated with the Samoa Islands and the Kurile Islands, are also apparent. In contrast to the tilt and bias method or other types of high-pass filtering techniques, the derivative filter does not produce edge effects. Thus variability can be mapped in areas where many of the repeat cycles are intermittent or missing.

Profiles B is a descending profiles that extends from the coast of Nicaragua to the Ross Sea (see B-B' in Figure 4.3). This profile was selected because it crosses an area of extremely low variability ( $\sim 0.2 \mu\text{rad}$ ) in the Southeast Pacific ( $0^{\circ}$  to  $-20^{\circ}$  latitude). This minimum variability is only slightly greater than the long-wavelength orbit error so the actual variability is either at the threshold or below the measurement precision of the unadjusted slope data. At  $-30^{\circ}$  latitude, the variability increases to about  $1 \mu\text{rad}$ . The high variability ( $1-3 \mu\text{rad}$ ) between  $-48^{\circ}$  and  $-62^{\circ}$  is associated with the Antarctic Circumpolar Current (ACC). The repeat cycles also illustrate the seasonal variation in the Antarctic ice front which is minimal during repeats 7 and 8 and maximal during 18 and 19.

Ascending profile C crosses high variability areas at both the ACC at  $\sim -50^{\circ}$  and the Agulhas Current at  $\sim -40^{\circ}$ . Again, the variability is very low between  $-20^{\circ}$  and  $0^{\circ}$ .

Profile D illustrates the high variability area ( $\sim 10 \mu\text{rad}$ ) of the Gulf Stream at  $40^\circ$  and the correlation of variability with ocean depth. In this area of the Gulf Stream, high variability is expected but there is an unexpected sharp decrease in variability that occurs at  $43^\circ$  latitude. This sharp decrease corresponds to the continental margin where ocean depths decrease from 5000 m to 200 m. The transition from high to low variability occurs at an ocean depth of  $\sim 3000$  m. As shown below in greater detail, this correlation of high variability in deep water and low variability in shallow water is a global phenomena.

It is interesting that the correlation of variability and ocean depth has not been noted in previous studies using Geos-3 and Seasat altimeter data. It is believed through this analysis, that the correlation has not been observed because the adjustment of the altimeter profiles causes the variability to "leak" from the high areas into the low areas. The problem is usually exaggerated because areas of high variability occur near continental margins and coastlines where profiles end. Consider the profiles along D-D'. Suppose a best fitting, linear trend was removed from each profile. The linear function would try to reduce the residual amplitude of the Gulf Stream variability by increasing the amplitude at the end of the profile. The outcome is that variability would "leak" from the high Gulf Stream area to the low continental shelf area near the end of profiles. Previous studies show high variability on the shallow continental shelves adjacent to areas of high variability such as the Gulf Stream and the Falkland Current was attributed to tide model error [Parke, 1981]. This analysis suggests that the tide models are not especially bad on continental shelves where the water depth exceeds about 200 m. Instead, the high variability observed in previous studies is an artifact



caused by adjusting the profiles.

Profile E illustrates a limitation of this slope method as well as evidence for short-wavelength tide model error near islands. By adjusting Geosat altimeter profiles (using a crossover method), Cheney et al. [1987b] were able to map the eastward propagation of a Kelvin wave associated with the 1986-1987 El Nino. Sea surface slopes associated with this Kelvin wave range from only  $0.04 \mu\text{rad}$  to  $0.1 \mu\text{rad}$ . As seen in Profile E at  $0^\circ$ , these slopes are too small to be detected using the derivative high pass filtering technique because its accuracy is  $\sim 0.2 \mu\text{rad}$ . However, by gridding and averaging over a 200 km radius (see below), the equatorial variability can be detected.

The other feature apparent in Profile E is the high variability associated with the very shallow water ( $< 100$  m) of the Tuamotu Archipelago ( $-15^\circ$  and  $-17^\circ$ ). From examination of several of these anomalous features, this short-wavelength variability reflects the tide model error in the GDR's. The largest tide model errors appear in water depths less than 100 m. A more prominent example of tide model error is apparent in profile F where it intersects the Amazon Shelf. On the broad, shallow shelf (depth  $< 100$  m) the sea surface slope profiles vary monotonically from one repeat cycle to the next. Moreover, the signatures seem to repeat themselves after  $\sim 20$  cycles; cycle 1 looks like cycle 20, 2 looks like 21 and 3 looks like 22. This signal is actually the once per day solar tide that is aliased into a much lower frequency by Geosat's sampling characteristics. The orbit plane of Geosat precesses at a rate of  $1.06^\circ$  per day with respect to vernal equinox. Therefore, it takes 340 days to complete one revolution. Every 17.05 days Geosat returns to the Amazon shelf to sample the solar tide. During this time, the phase of the tide will appear to have shifted by only  $18^\circ$ . After 20 repeat cycles, Geosat will have sampled one complete solar tidal cycle.

Although the short period solar tide is aliased into a much longer period, a long time series of Geosat data could be used to improve tide models in shallow areas where errors are large.

The final profile G extends from South of New Zealand, across East Australia and terminates in the Yellow Sea. This profile was included to illustrate the artificial high variability that is associated with missing and/or short profiles. As expected, the variability is high over the East Australian Current ( $-40^{\circ}$  to  $-35^{\circ}$ ). However, it is also high along the short profile between Northern Australia and New Guinea ( $-10^{\circ}$ ). Because Geosat is sometimes unable to regaining lock when it moves from land to ocean, only about one half of the data are available over this short segment. In general, high variability in areas where many profiles are missing (e.g. where land and ice is prevalent) has been observed in this analysis. In these areas, some of the high variability is due to poor quality of the available data. However, many of the areas where data are missing are also shallow ( $< 100$  m) so the high variability may be due to tide model errors as well.

#### 4.3.2 RMS Slope Variability

The root mean square (rms) variability in along-track sea surface slope was computed for each pass from the 22 slope difference profiles. Ascending and descending rms slope variations were then averaged into  $1^{\circ}$  by  $1^{\circ}$  areas. Areas containing no data were interpolated from surrounding areas. The global map was then low-pass filtered to remove the short wavelengths ( $< 220$  km) associated with gridding the data in  $1^{\circ}$  cells. The results are shown in Figure 4.9 as a color image of the rms

slope variability. The colors ranging from light blue to red indicate the level of variability. Over most ocean areas, the rms slope variability is 1  $\mu$ rad or less. Small areas of higher variability are associated with missing data, mesoscale variations in ocean currents and tide model error.

As stated in the last section, the slope variability becomes artificially high when many of the repeat cycles are missing. These areas were identified by plotting the number of profiles used to compute the rms slope variation. The data density map is shown in Figure 4.10 where black represents areas where all 22 repeat profiles are available and white represents areas where there are no profiles. On the average, 15 profiles are available although there are areas in the Arctic and Antarctic where less than 5 profiles are available. In these areas of low data density, the rms variability is artificially high and probably unreliable. Therefore when interpreting the rms variability maps, one must also check the data density map to see that sufficient data are available.

In ocean areas where the number of profiles is greater than about 6, the rms slope variability reflects mesoscale variations in ocean current as well as unmodeled errors (mostly tides). In general, this global rms slope variability map from Geosat/ERM is similar to the global mesoscale variability map derived from Seasat 3-day repeated profiles (Figure 4.1, [Cheney et al., 1983]). However, this new map has improved temporal coverage because 375 days of Geosat/ERM data were used instead of 25 days of Seasat data and improved spatial resolution because Geosat has a ground-track spacing of 160 km at the equator instead of the 930 km spacing for Seasat. In addition, because the derivative filter has no edge effects, it was able to extract variations in sea surface slope within 100 km of all shorelines.

The highest variations in sea surface slope ( $> 3 \mu\text{rad}$ ) occur over the western boundary currents such as the Gulf Stream, the Kuroshio Current, the Falkland/Brazil Current and the Agulhas Current. The Antarctic Circumpolar current (ACC) produces a nearly continuous band of medium to high ( $1.5 - 4 \mu\text{rad}$ ) variability in the Southern Ocean. The pattern of ACC variability is not random, but as shown below it is highly organized by the topography of the seafloor. In each ocean, the major gyres are delineated by the color contours of rms variability. The highest variability occurs where the western boundary currents depart from the confinement of the continental shelves ( $30^\circ - 50^\circ$  latitude). Intermediate variability extends decreasingly towards the east and towards the equator. Variability is generally low along the eastern sides of the ocean basins except in the south Atlantic where the ACC and Agulhas Currents converge. A band of intermediate to low variability extends across both the Atlantic and Pacific Oceans between latitudes of  $-5^\circ$  to  $15^\circ$ . The lowest variability ( $< 0.5 \mu\text{rad}$ ) occurs south of this band in the eastern ocean areas between latitudes of  $-5^\circ$  to  $-30^\circ$ . The entire Weddell Sea is also characterized by low variability but the results may not be reliable because this area was only sampled by a few profiles during the Austral summer.

#### 4.3.3 Correlation of Variability with 3000 m Depth

The improved spatial resolution of the rms slope variability map reveals the strong correlation between variability and ocean depth. To show this correlation in greater detail, a 3000 m depth contour has been plotted on the rms slope variability map (Figure 4.11). White areas on the map have rms variability less than or equal to 0.2

$\mu\text{rad}$  while black areas have variability greater than or equal to  $2.5 \mu\text{rad}$ . The 3000 m depth contour was derived for a 5 minute gridding global topography data base. To be consistent with the resolution of the rms variability map, the depths were filtered and decimated to a  $1^\circ$  by  $1^\circ$  grid before contouring. In general, variability is high where major ocean currents are strong and ocean depths exceed 3000 m. Variability is generally low where ocean depths are less than 3000 m. A second type of high variability occurs in very shallow water ( $< 100$  m) where ocean tides are a problem.

The correlation of variability with 3000 m depth contour is most apparent for the western boundary currents and the ACC. For example, the variability associated with the Gulf Stream is low until the Gulf Stream separates from the continental shelf at North Carolina. To the northeast, there is marked change in variability that coincides with the 3000 m depth contour; variability is low on the shallow side of this contour and high on the deep side. At the Grand Banks, the variability turns northward following the deep ocean basin. Further to the east, the variability is low over the Mid-Atlantic Ridge where it is shallower than 3000 m. The Kuroshio Current does not show this strong correlation with ocean depth because there are no large shallow areas in its path. The variability of the Falkland/Brazil Current shows an excellent correlation with the 3000 m depth contour where the variability is high in the deep Argentine Basin and low on the Falkland Plateau. In the contrast to the North Atlantic, the variability is not strongly influenced by the Mid-Atlantic Ridge. Perhaps because it only has minor protrusion above the 3000 m depth plane. Other weaker correlation of variability with ocean depth occur along the East Coast of Australia as well as in the Gulf of Mexico.

The most striking correlation of variability and ocean depth occurs along the ACC. Starting at  $0^\circ$  longitude and moving eastward around Antarctica, the variability

has intermediate values in the deep South Atlantic but is low above the Southeast Indian Ridge, the Walvis Ridge and the western continental margin of Africa. Further to the east, the variability reached a maximum in the Agulhas Basin and then it is constricted by the narrow passage between the Agulhas Plateau and the South African Margin. A second local maximum occurs in the Enderby Basin just south of the Southwest Indian Ridge. The low variability at 45° longitude correlates with the major plateaus, the Madagascar Ridge, the Del Cano Rise and the Conrad Rise. Between the Madagascar Ridge and the Del Cano Rise, the variability appears to be focused by the narrow passage. To the east (60° longitude), another local maximum in variability occurs in the deepest part of the ocean basin. Variability is low on the Kerguelen Plateau and the shallow part of the Southeast Indian Ridge and high in the basin between these features. The boundary between high and low variability is well correlated with the 3000 m depth contour, especially along the northeast margin of the Kerguelen Plateau.

Between 100° and 140° longitude there are no major topographic plateaus and the variability has intermediate values and is diffuse. However, between 140° and 180° longitude, there are a series of topographic barriers that organize the variability. At 150° longitude the variability is low above the Tasman Rise as well as the shallow part of the Southeast Indian Ridge. High variability occurs in the basin between these features. Further to the east, the ACC crosses the narrow Macquire Ridge which extends from the New Zealand in the north to the shallow Southeast Indian Ridge in the south. The variability is intermediate to low above the Macquire Ridge and increases to a local maximum in the deep Emerald/Southwest Pacific basin to the east of the Macquire Ridge. In agreement with previous studies [Colton and Chase, 1983], this analysis

also found that the variability is high downstream from the Macquire Ridge. However, since the variability is also high in the basin upstream from the Macquire Ridge, this analysis does not show evidence that the high variability is caused by the vertical deflection of the ACC as it flows over the Macquire Ridge.

Along the Campbell Plateau, the boundary between high and low variability is highly correlated with the 3000 m depth contour. The high variability follows the deep Southwest Pacific Basin to the northeast and then turns eastward across the South Pacific. Variability is lower above the Pacific/Antarctic Rise. Further to the east, the variability is intermediate and diffuse until the ACC reaches the constriction of the Drake Passage. The variability is not especially high in the Drake passage. However, again the highest variability is found in the deepest water of the Yaghan Basin along the northern boundary of the Drake passage. Variability is low in the shallower Scotia Sea, but returns to intermediate values when the ACC reaches the deep South Atlantic.

#### 4.3.4 Variability due to Tide Model Error

As shown in profiles E and F (Figure 4.8), large tide model errors produce variations in sea surface slope, especially in shallow water (< 100 m). These shallow water tide errors are also apparent in Figures 4.9 and 4.11. However, one must keep in mind that high variability also occurs in shallow areas near land where many of the repeat profiles are sometimes missing. Thus, the interpretations of this investigation are focused on areas where most of the repeat profiles are available (Figure 4.10). Shallow water tide errors are found over two types of features, shallow continental shelves in remote areas and deep ocean seamounts/plateaus that rise to near sea level. The most prominent example of shelf tide model error occurs on the Amazon Shelf

where water depths are less than 100 m. As shown in Figure 4.8f, this tide model error is perfectly aliased from a period of 1 day to a period of 340 days by the sampling characteristics of Geosat. Other less prominent examples occur in the Yellow Sea, the Timor Sea (Northeast Australia), the Great Barrier Reef, and Bristol Bay (Southeast Alaska). While large tide model errors sometimes occur in shallow shelf areas, there are many broad, shallow shelves where tide model error is not apparent. This can be speculated that either the tides are well known on these shelves or the tidal variations are low.

The more troublesome shallow water variability sometimes occurs above shallow seamounts and plateaus that are surrounded by the deep oceans. In these areas, one would expect the tide models to be quite accurate. However, high variability occurs in the shallow parts of the Tuamotu Archipelago (profile E), Bermuda, St Helena I. and the Maldives (Indian Ocean). At each of these features, there is a very small island(s) that protrudes above sea level. There are two probable causes for this high variability. First, it is due to reflections from the land areas. Second, these small islands do not have tide gauges that were used when developing the tide models. It is important to establish which of these causes the variability. If it is due to land reflections then one must be more careful in editing land radar returns. If it is due to tide model error then one must question the use of some island tide gauges for determining deep ocean tides.

#### **4.4 Summary**

The large absolute radial orbit error associated with the NAG orbit on the altimeter data record for the Geosat ERM mission (5 ~ 10 m) prohibits the use of these data for basin-scale studies of ocean circulation. Most of this Geosat GDR orbit error occurs at



a period of one cycle per orbital revolution. Moreover, it repeats geographically so that the relative orbit error among repeat profiles is only 1 ~ 3 meters. In previous studies the tilt and bias method has been used to remove the long wavelength relative orbit error to extract mesoscale (300 - 1000 km) variations in dynamic topography. Away from the coastline the tilt and bias method is effective. However large edge effects can occur near the ends of profiles where variability is high. This occurs, for example, along most western boundary currents where variability is high near the coastline. The edge effects produce artificially high variability on the shallow continental shelves between the end of the profile and the zone of high variability. These artifacts have been interpreted as tide model error or true variability.

A simple band-pass filter method has been developed in this investigation in order to suppress the long wavelength radial orbit error without producing edge artifacts. Each altimeter profile is first differentiated (high-pass filter) and then averaged with the other collinear slope profiles. The next step is to take the difference between the individual repeat profiles and the average profile resulting in short wavelength altimeter noise and variations in sea surface slope along the profile. The final step is to suppress the altimeter noise with a low-pass filter. No adjustments of the profiles are necessary and the high-pass derivative filter produces no edge effects. Short edge effects (< 100 km) are produced by the low-pass filter, so data 100 km from ends of passes are eliminated. A spectral analysis of the repeat slope profiles reveals that the largest component of radial orbit error has an amplitude of  $0.14 \mu\text{rad}$  at a wavelength of  $\sim 40,000$  km. At longer and shorter wavelengths the error is generally less than  $0.03 \mu\text{rad}$ . This maximum relative Geosat/ERM orbit error transformed into slope error

corresponds to a measurement error on only 14 cm over a distance of 1000 km. Since mesoscale slope variability is almost always greater than  $0.2 \mu\text{rad}$ , the simple differentiation procedure effectively suppresses the orbit error below the variability signal.

The global rms variability map shows previously unknown spatial details that are highly correlated with seafloor topography. Over most areas, the rms slope variability is less than  $1 \mu\text{rad}$ . However at mid to high latitudes, areas of higher variability occur in deep water ( $> 3000 \text{ m}$ ) adjacent to continental shelves, spreading ridges and oceanic plateaus. Variability is low in shallow areas ( $< 2000 \text{ m}$ ). Along the ACC, the mesoscale variability is organized by the many shallow areas in its depth. There is no convincing evidence that variability is higher downstream from topographic protrusions. Instead, the areas of highest variability occur in the deep basins ( $> 4000 \text{ m}$ ).

The high correlation of mesoscale variability and ocean depth indicates that the major western boundary currents and the ACC have large barotropic components. At high latitudes where there is little change in seawater density with depth, the major currents can extend to the seafloor [Neumann, 1968]. Thus a correlation of mesoscale variability and ocean depth is expected. The style of correlation (i.e. low variability in shallow water, high variability in deep water) is somewhat of a puzzle. Perhaps wind-driven accelerations of the ACC are rapidly damped by bottom friction in the shallow water and the damping is less efficient in the deep water.

# GEOSAT Ground Tracks

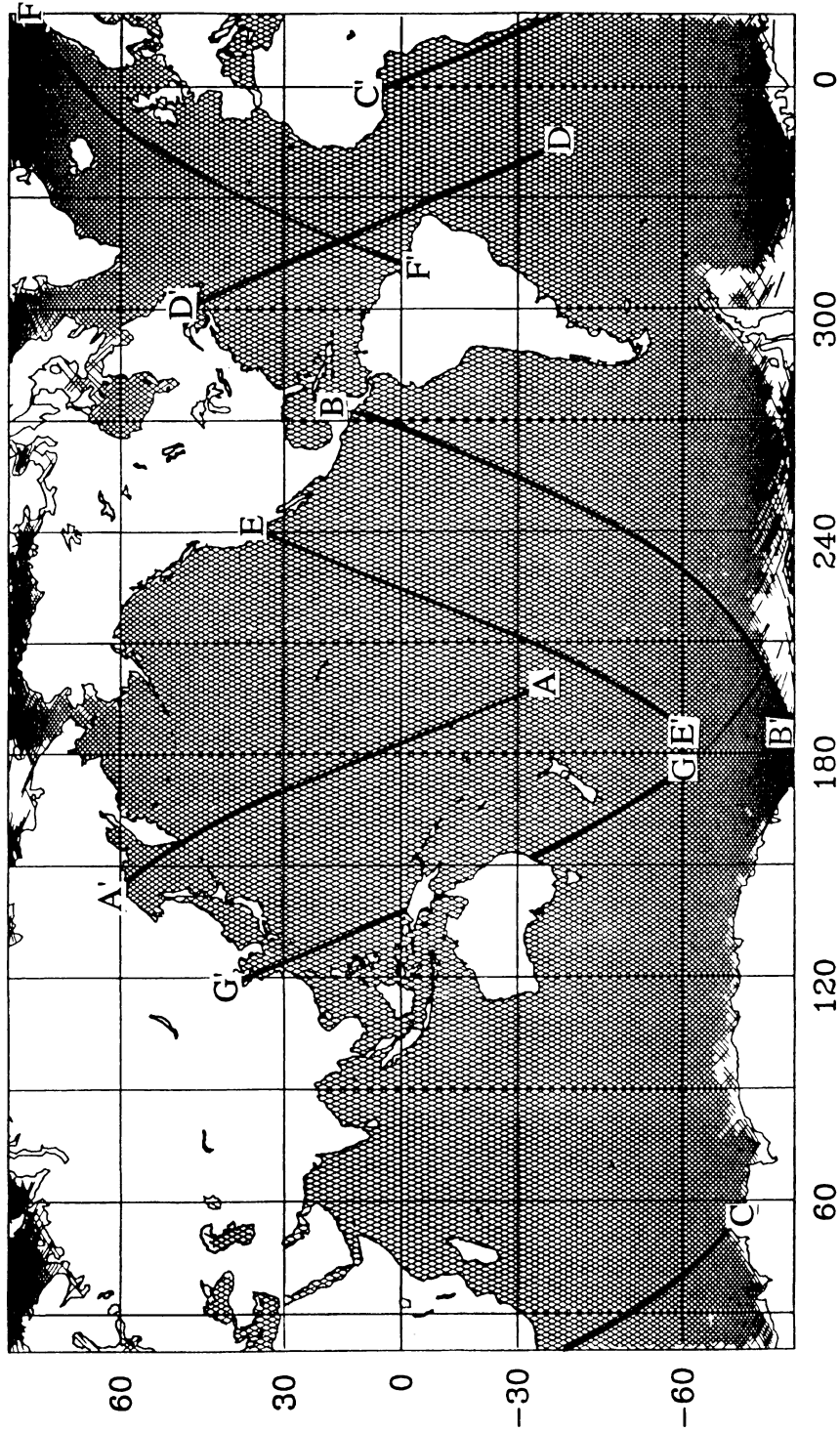


Figure 4.3 Geosat ground tracks for altimeter data analysis. Highlighted profiles A - G are shown in Figure 4.8.

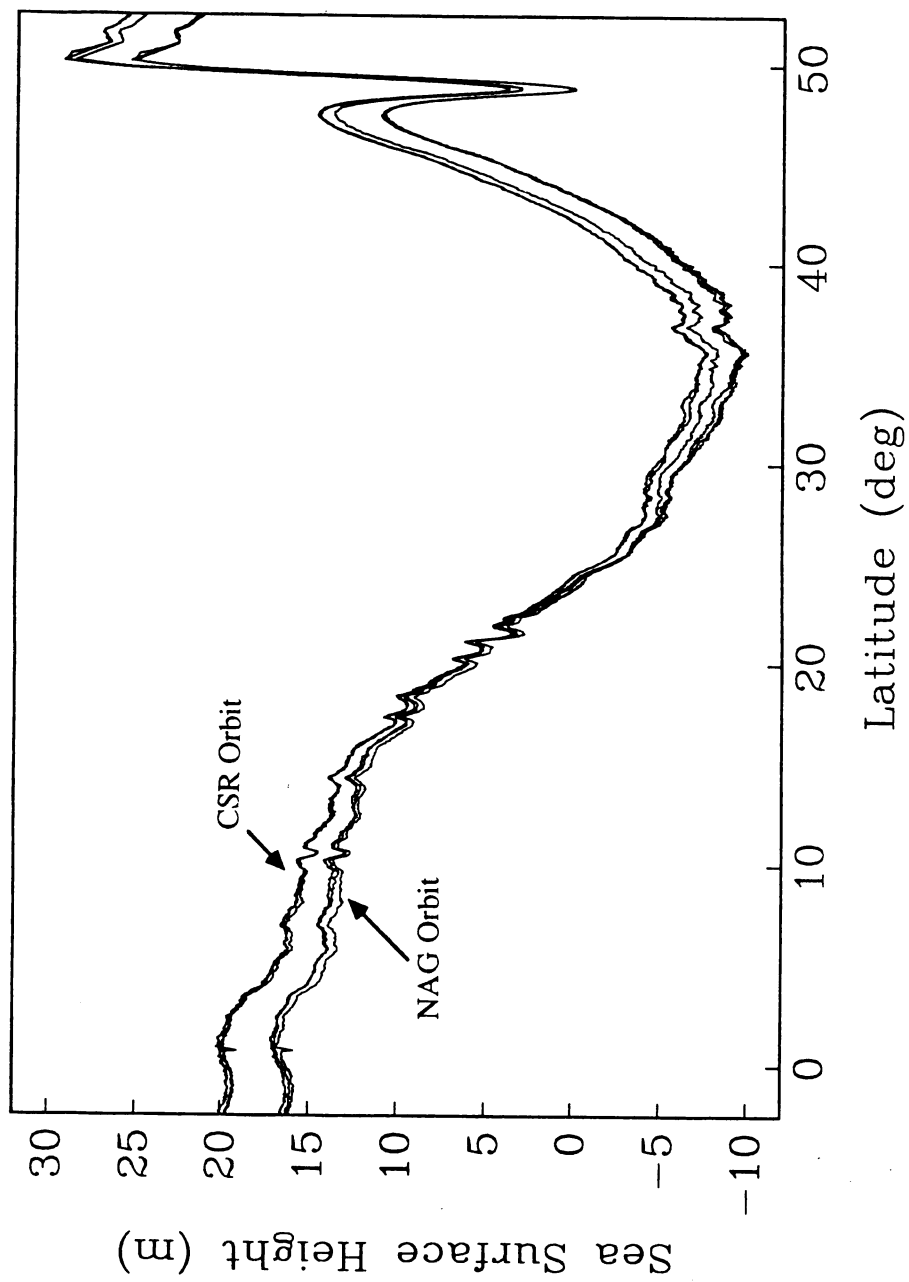


Figure 4.4a Geosat collinear altimeter sea surface height profiles (A-A' on Figure 4.3)

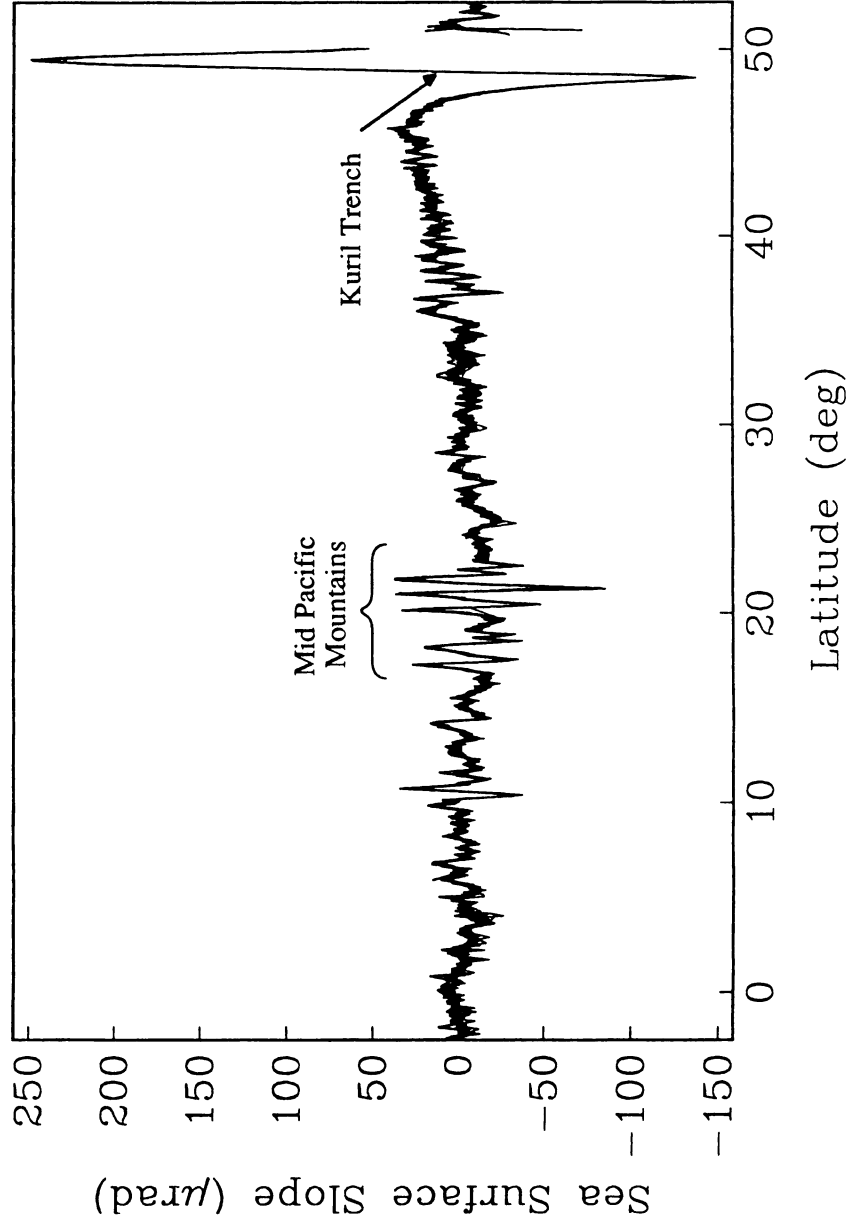


Figure 4.4b Geosat collinear altimeter slope profiles (A-A' on Figure 4.3). The derivative suppresses the long-wavelengths including the orbit error. Large variations in slope reflect seafloor topography.

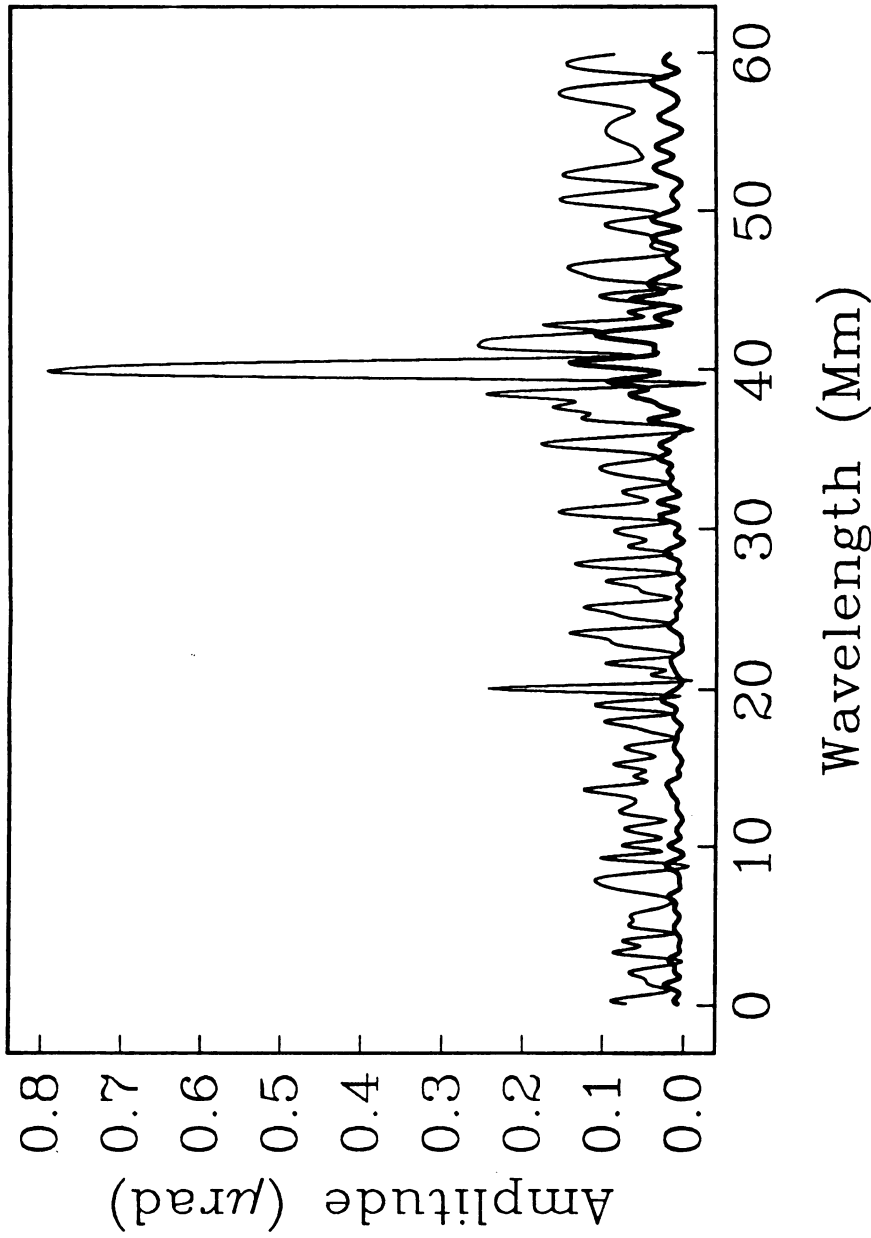
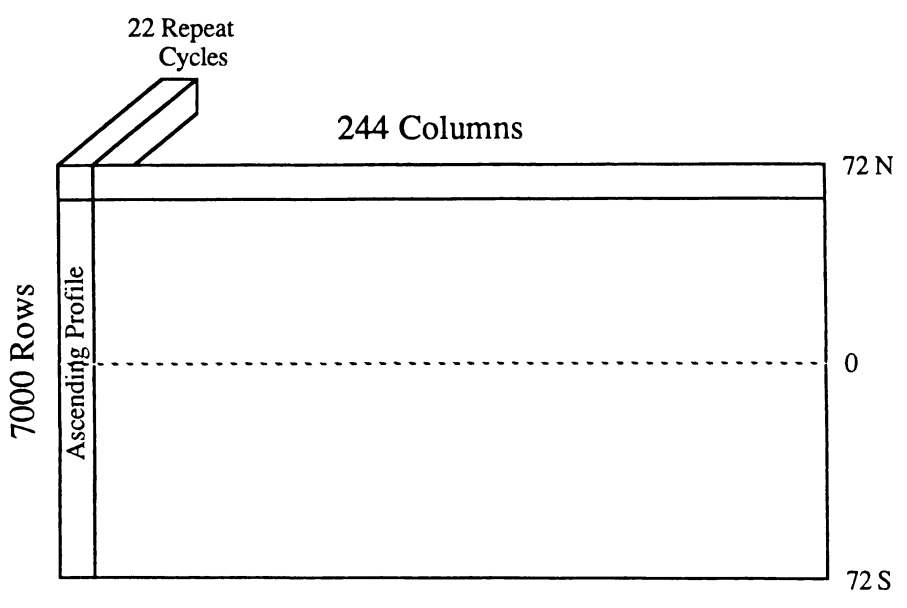


Figure 4.5 The absolute slope orbit error spectrum (CSR-CSR, light curve) has a peak of 0.8  $\mu\text{rad}$  at 40 Mm (40,000 km) wavelength. The relative slope orbit error spectrum (NAG-NAG, heavy curve) has a small peak of only 0.15  $\mu\text{rad}$  at 40 Mm wavelength.

### Stack File



### Stack Record

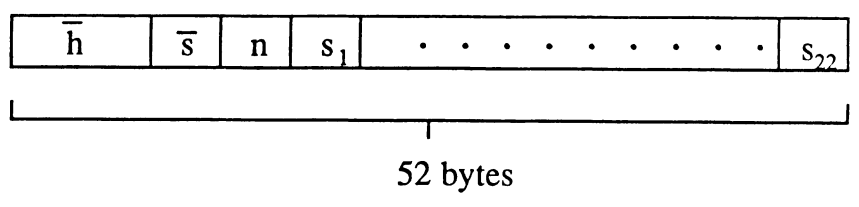


Figure 4.6 Structure of Geosat altimeter data stack files

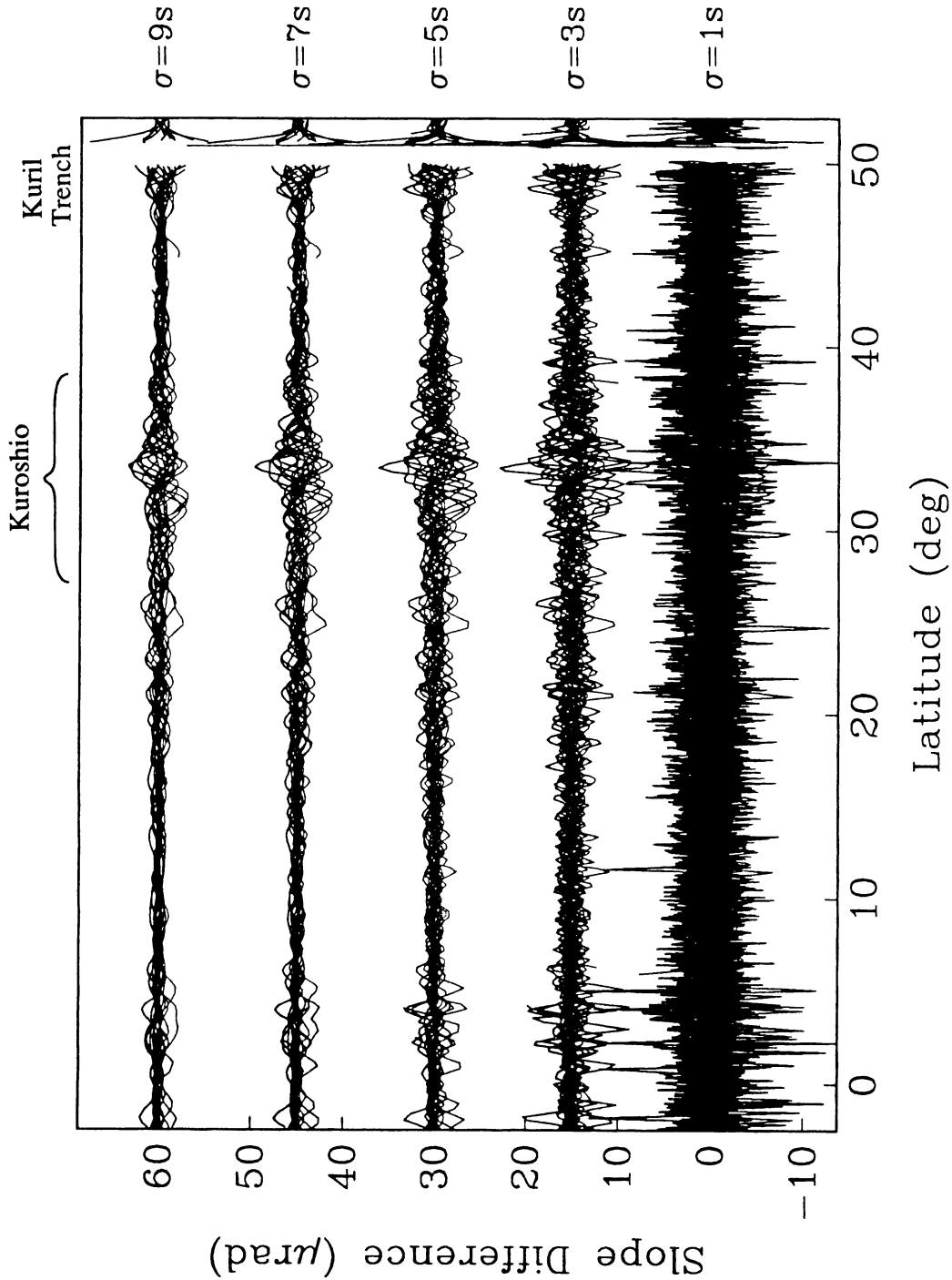


Figure 4.7 Performances of low-pass Gaussian filter



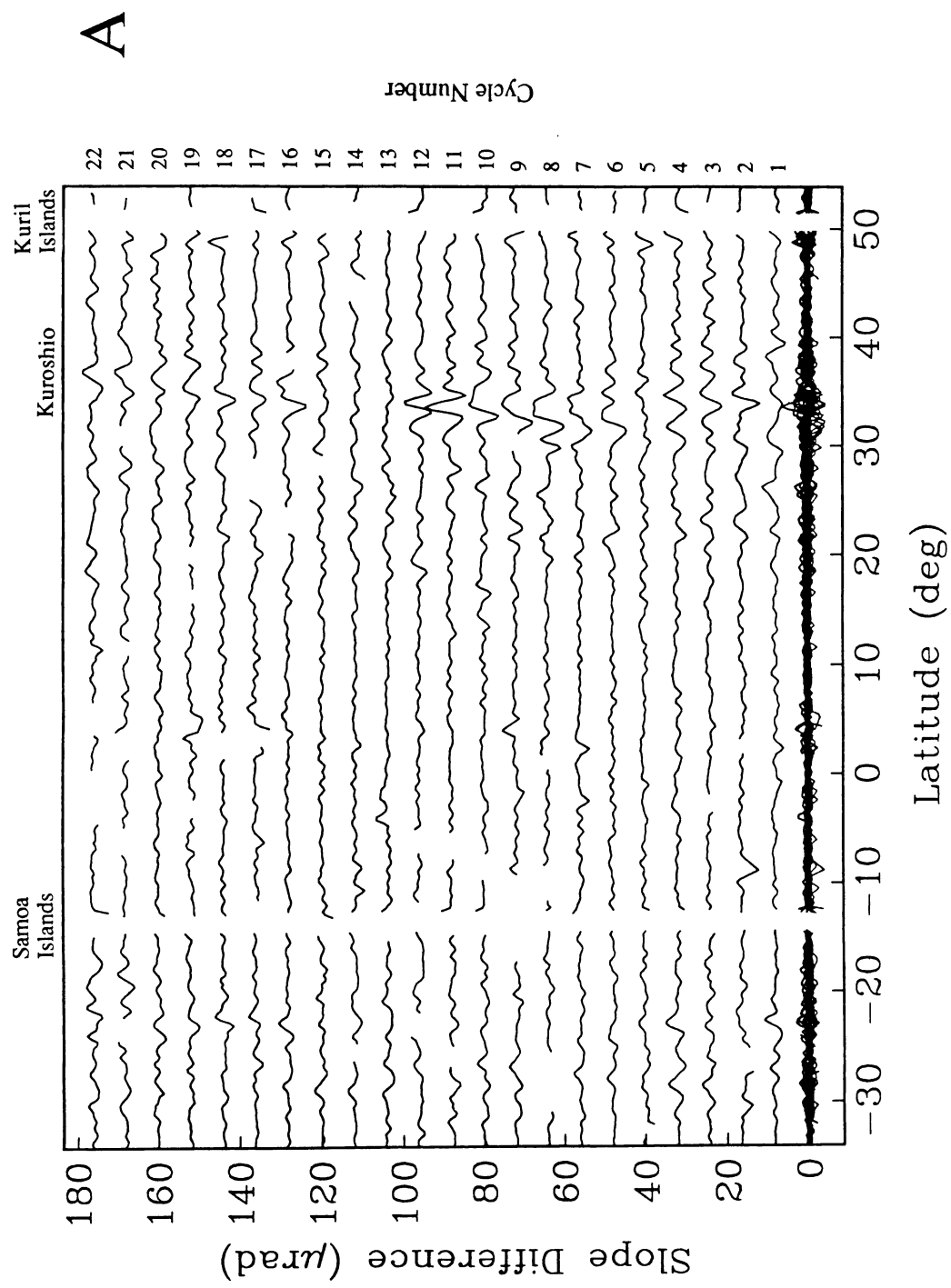


Figure 4.8a

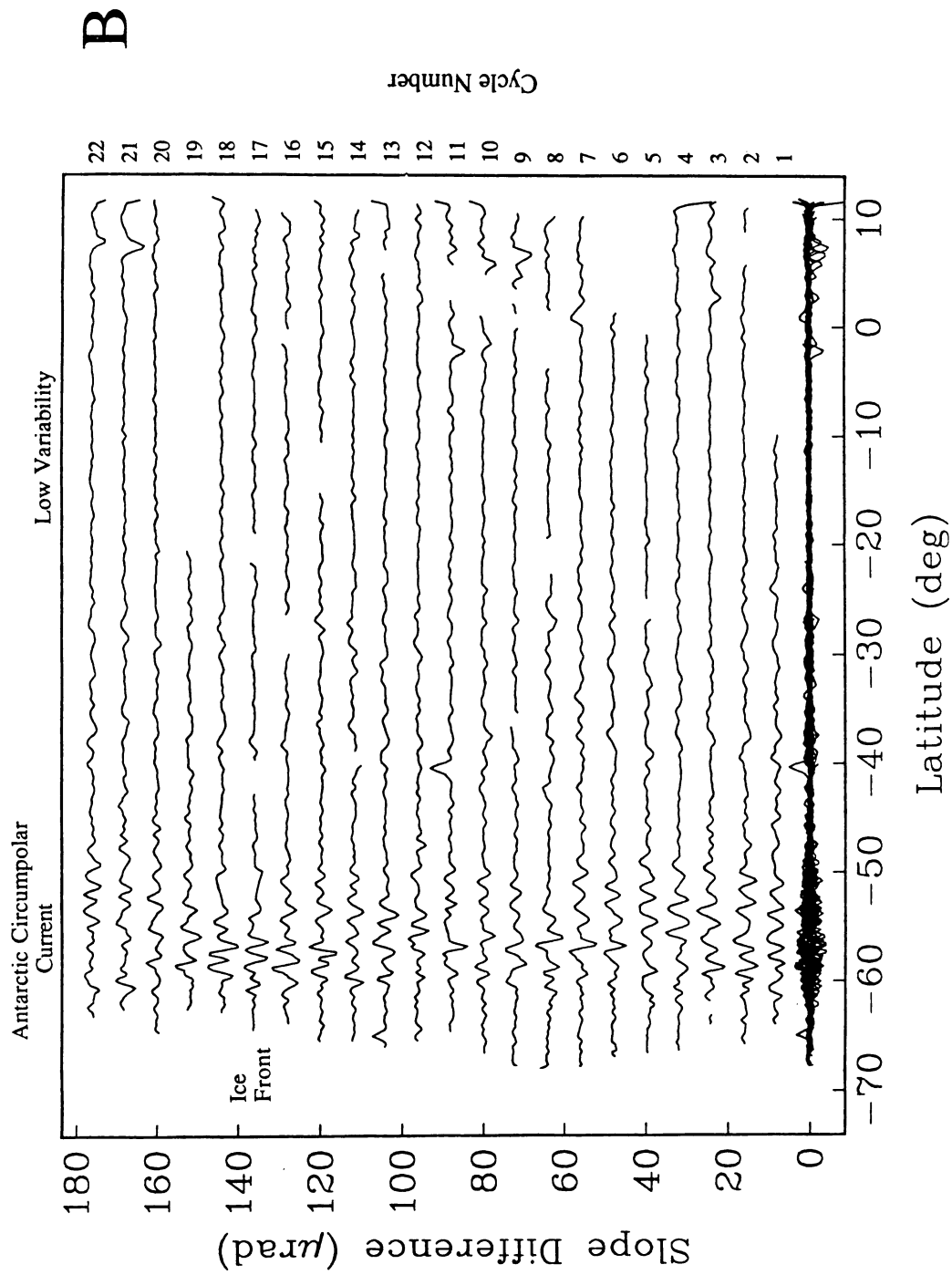


Figure 4.8b

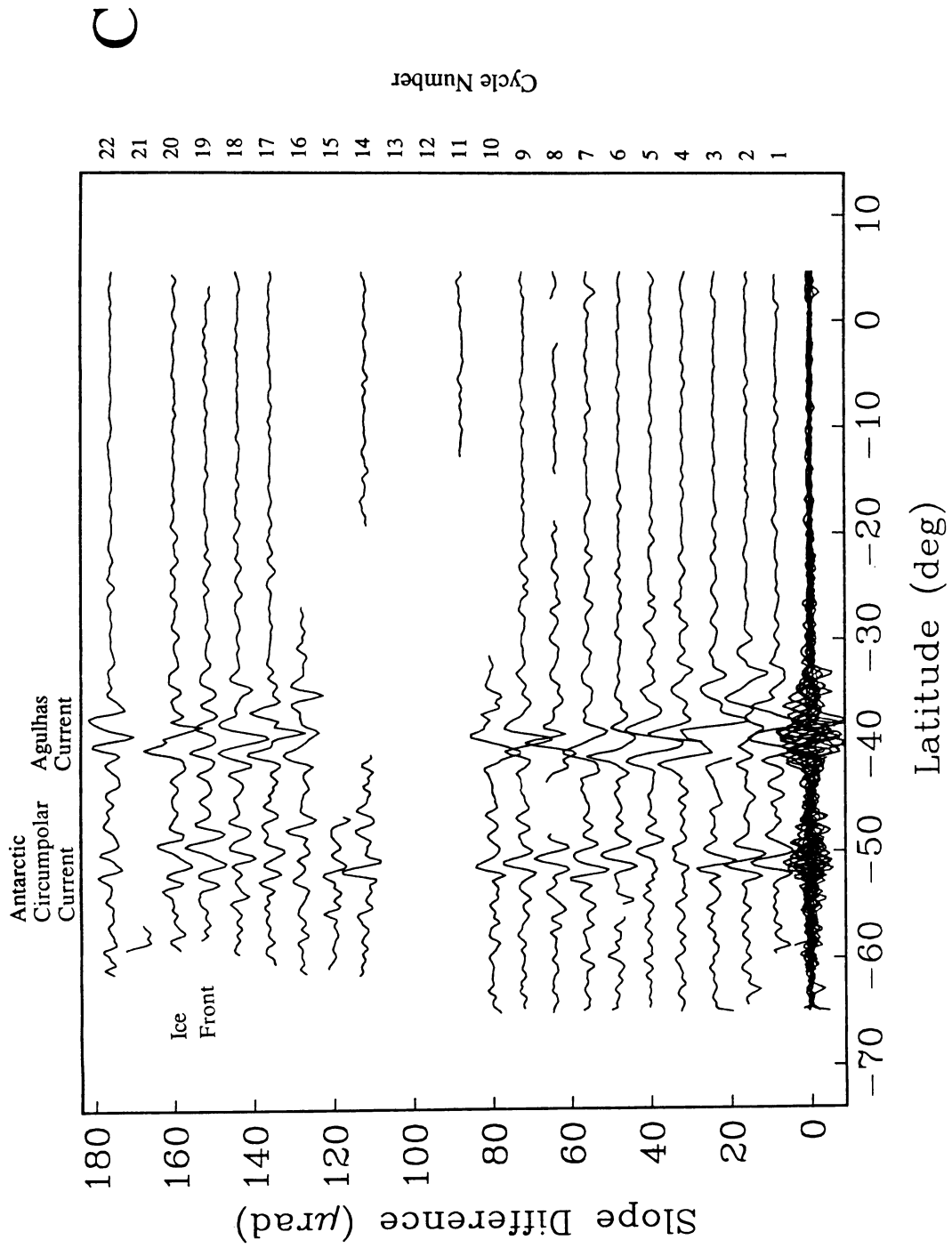


Figure 4.8c

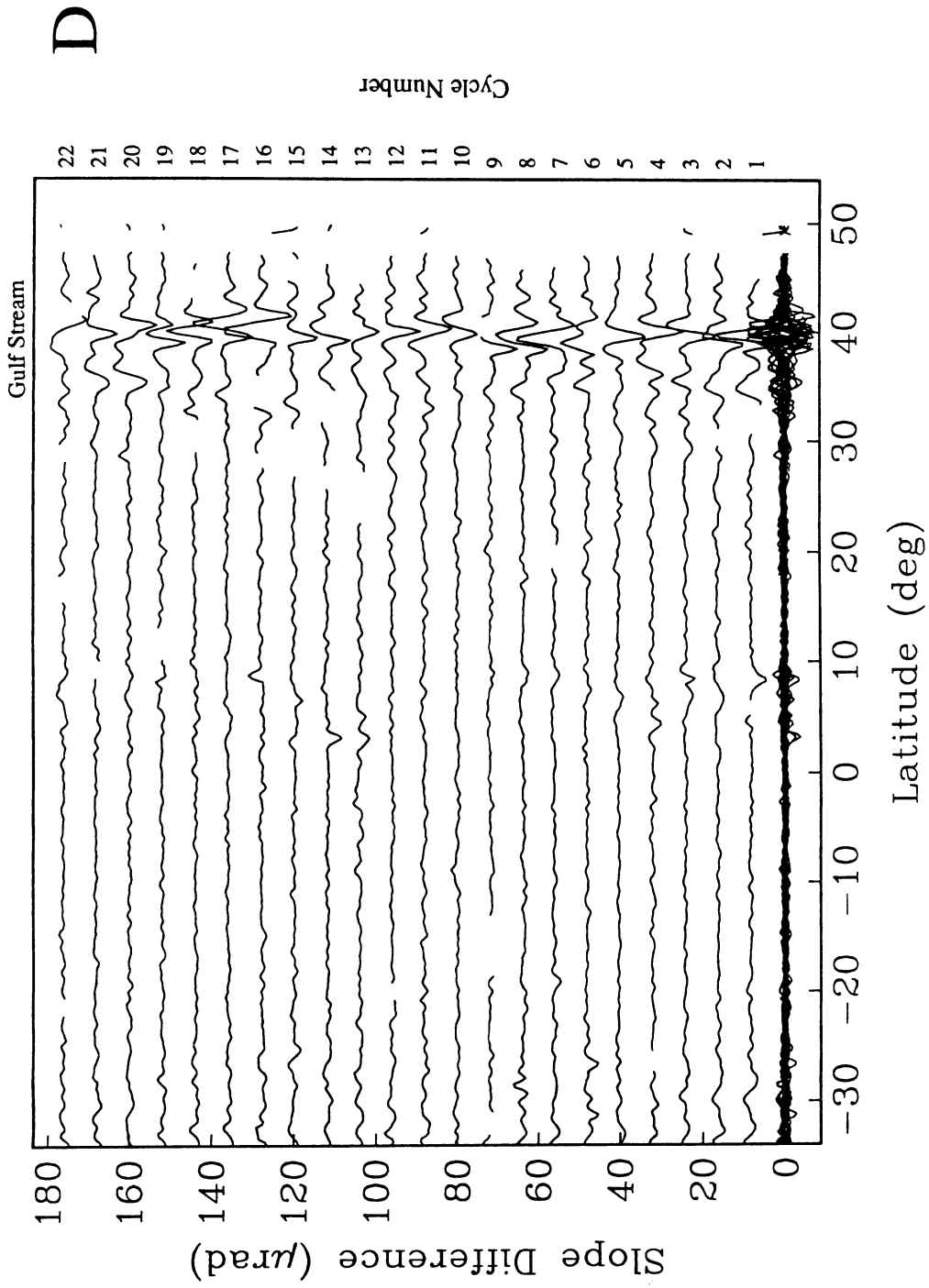


Figure 4.8d

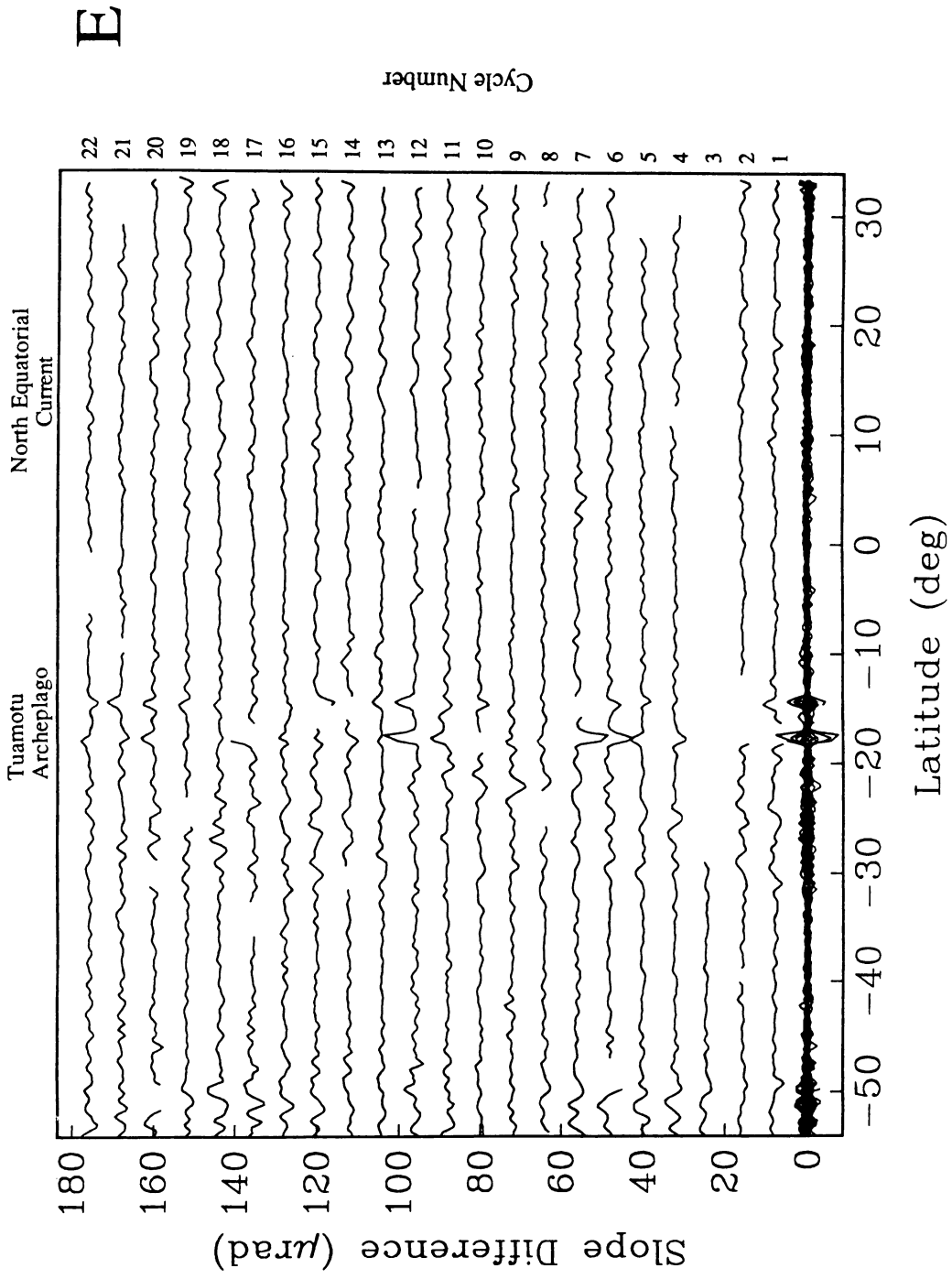


Figure 4.8e

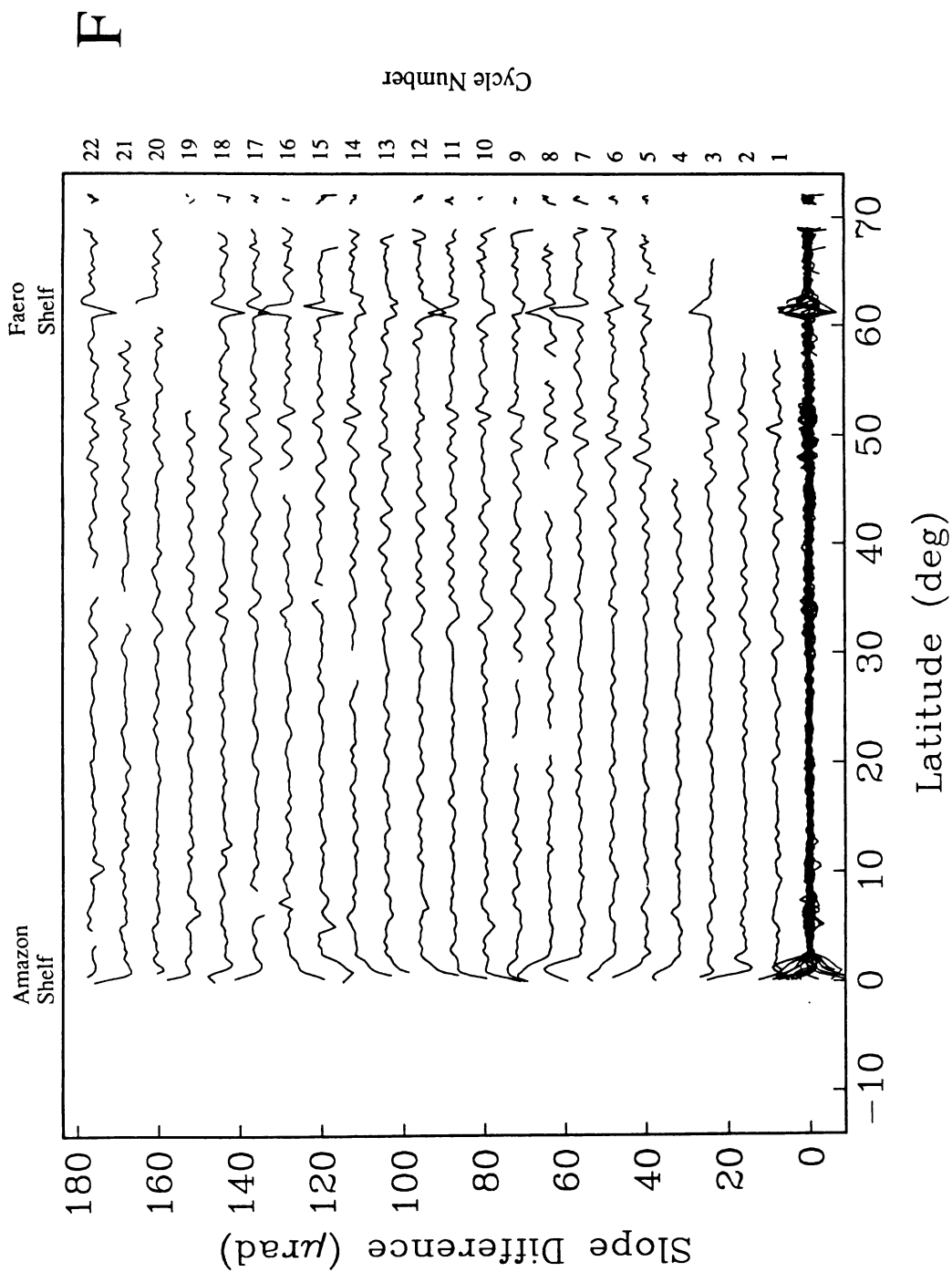


Figure 4.8f

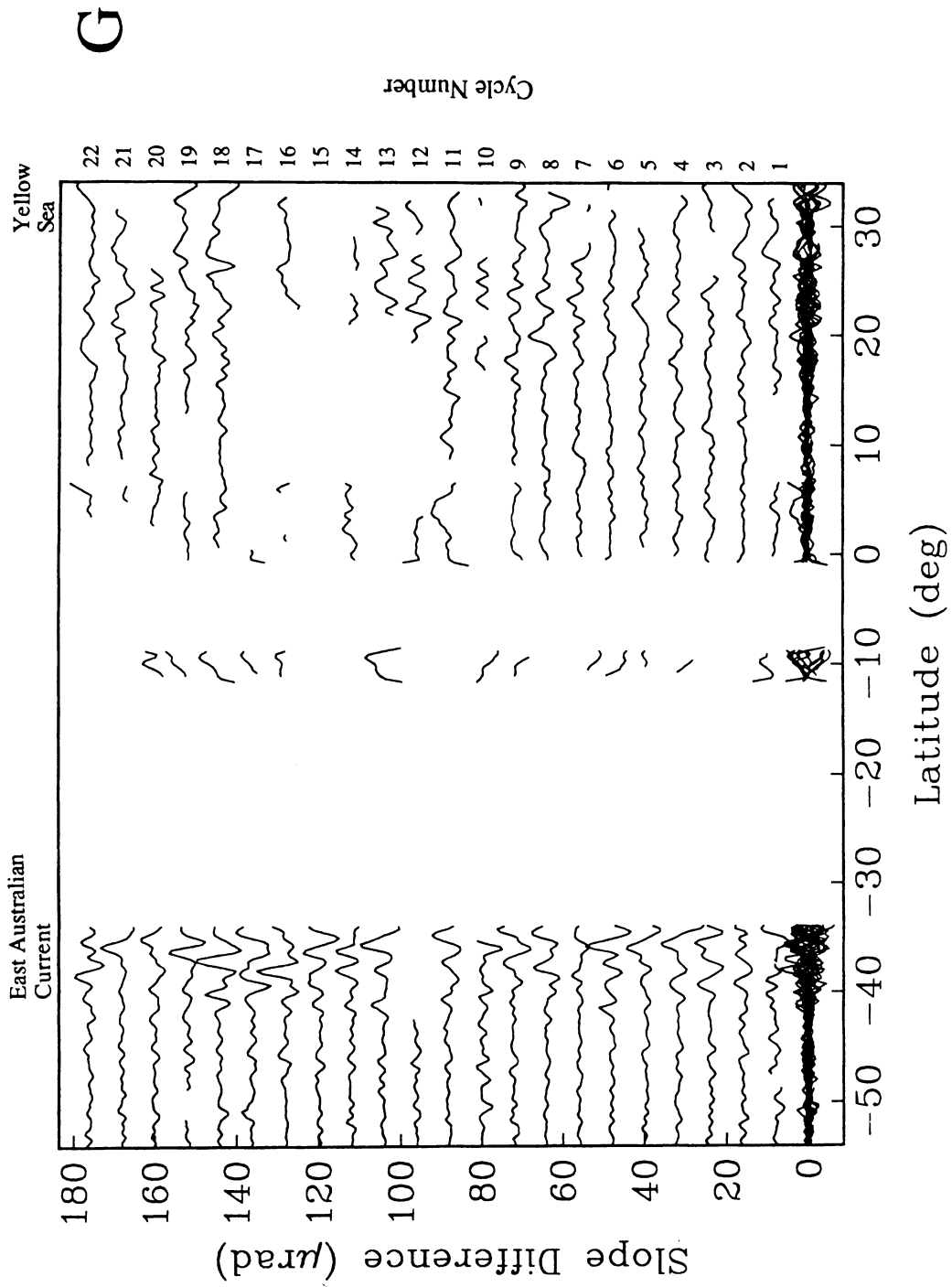


Figure 4.8g

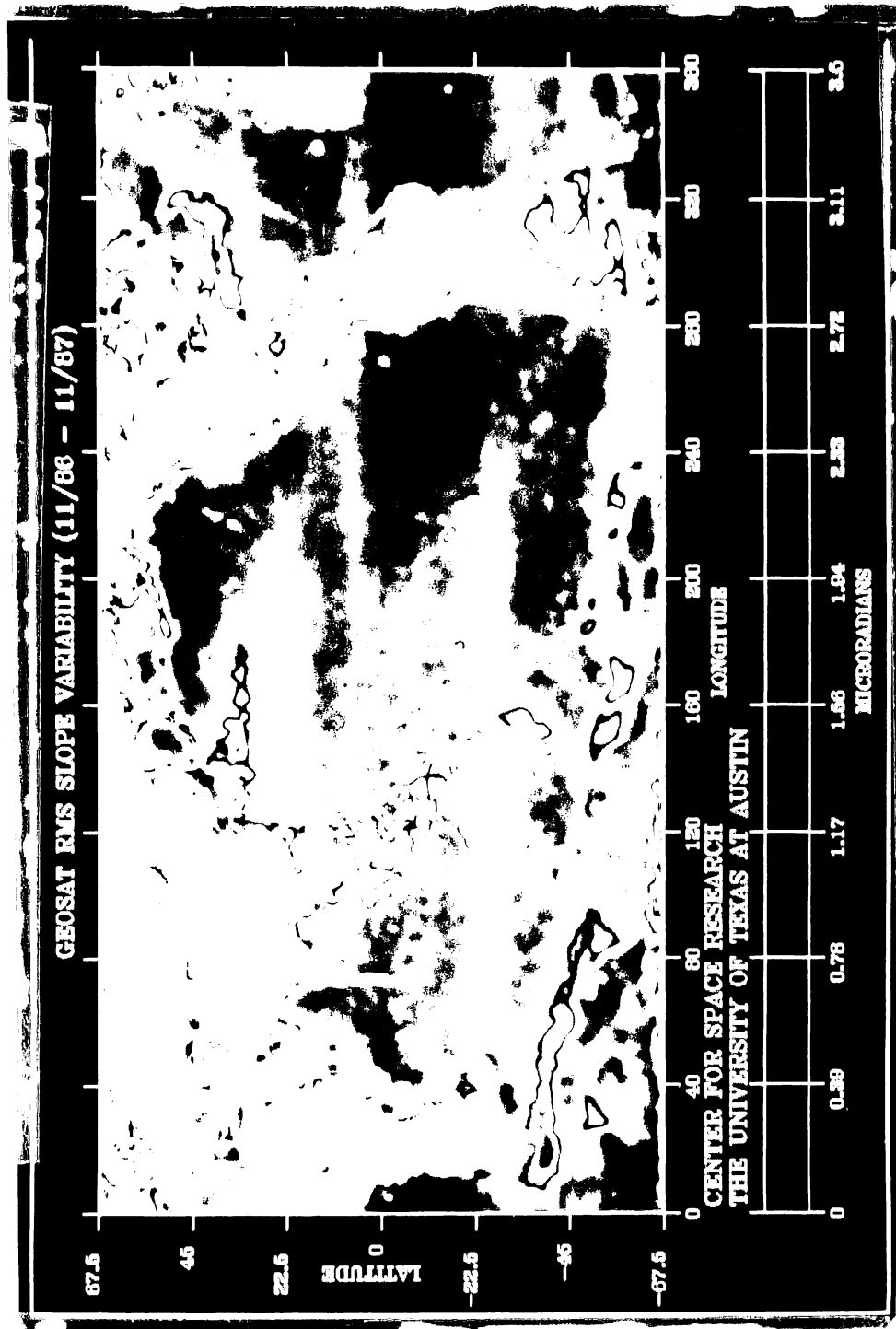


Figure 4.9 Root mean square (rms) slope variability from 1 year Geosat/ERM data. Dark grey is low variation in sea surface slope and red is high variation in slope. Over most ocean areas the rms variability is less than 0.7  $\mu\text{rad}$ . Zonal bands of intermediate variability are associated with the major gyres and equatorial currents. The highest variability occurs in the western currents and the ACC.



# Geosat Data Density



0 Profiles



22 Profiles

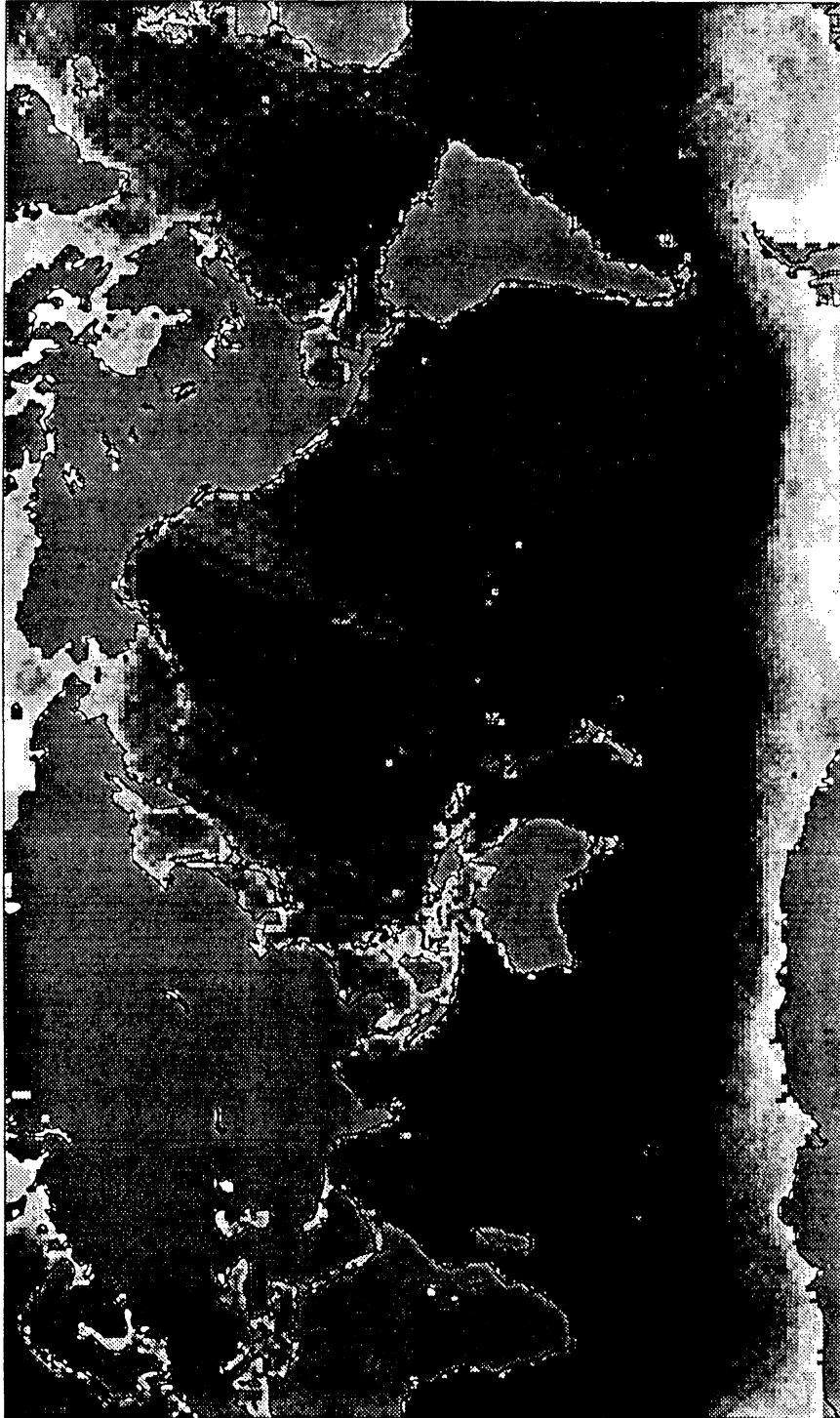


Figure 4.10 Geosat ERM altimeter data density

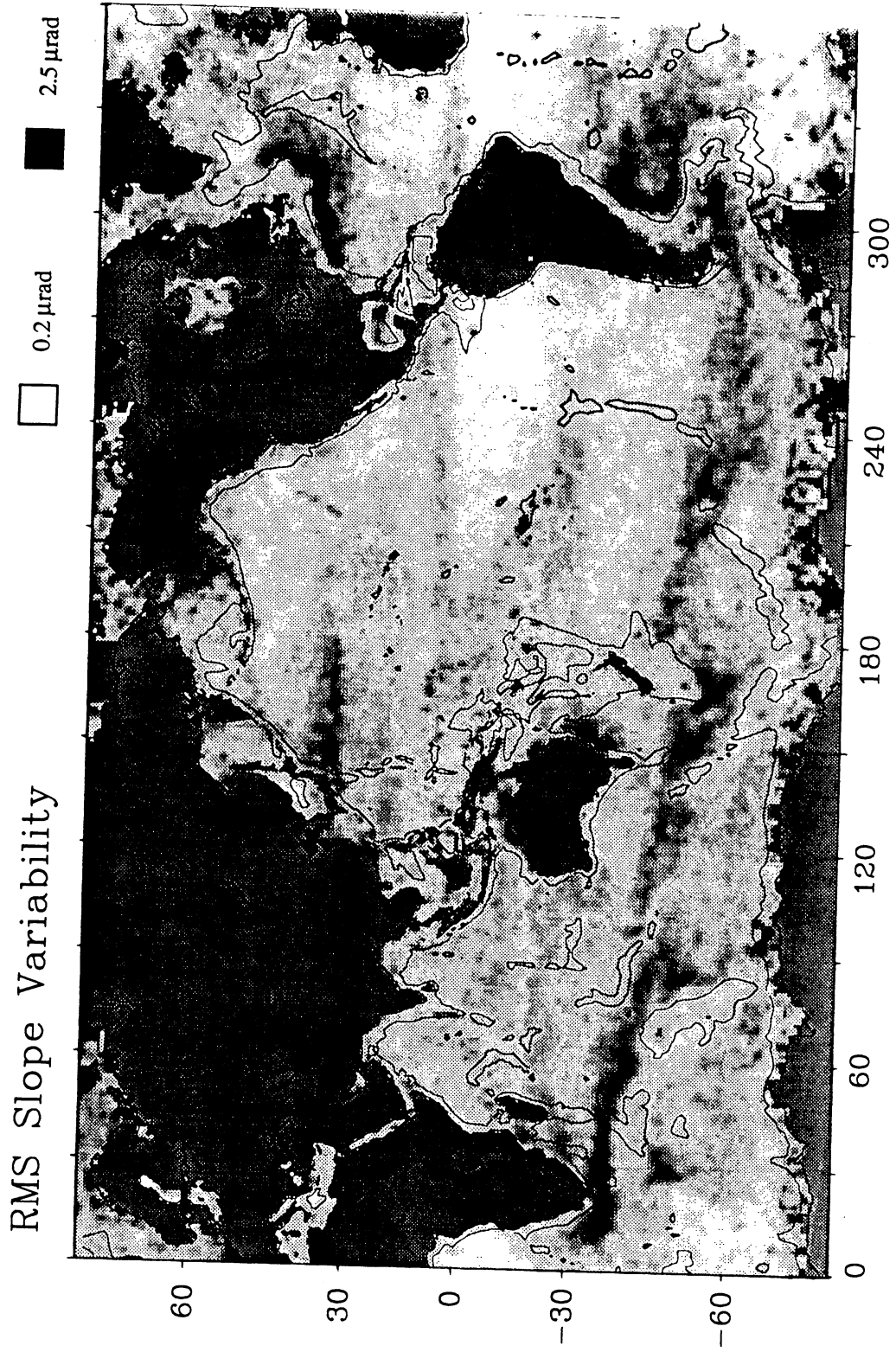


Figure 4.11 Correlation of variability and 3000 m ocean depth contour

## **Chapter 5**

### **Eddy Kinetic Energy**

#### **5.1 Introduction**

The existence of the eddies as part of the ocean circulation has been known to the oceanographers for a long time. Only recently these activities have attracted a major research effort because of the oceanic eddy field is believed to be the dominant mechanism for transforming energy and momentum in the ocean [Douglas et al., 1983].

A satellite altimeter measures the distance between the spacecraft and the sea surface with an accuracy less than 5 cm. With independently determined satellite ephemerides, sea surface heights can be inferred from altimeter measurements directly [Chapter 1]. If we consider the eddy field in geostrophic balance, sea surface slope variability is proportional to the changes of surface velocity of ocean currents. Also, an estimation of the eddy kinetic energy can be deduced under the assumption of quasi-isotropy of the velocity variability. The analysis of the first year Geosat/ERM altimeter data (see Chapter 4) yielded 22 sets of global collinear altimetric sea surface slope difference profiles. Eddy kinetic energy associated with Gulf stream and Kuroshio Current has been derived from these slope variabilities.

#### **5.2 Theoretical Basis**

Ocean currents are caused by the interaction of the Earth's rotation with the wind field, exchanging energy with atmosphere, variations of water salinity and other

phenomena. It is also a function of ocean depth and geographic location. The spatial scales of the ocean current range from 30 km up to a maximum of 10000 km (the extent of the Pacific ocean). Geostrophic equilibrium is a first-order solution of the primitive hydrodynamic equations. It states that the horizontal velocity field is such that the Coriolis force is balanced by the pressure gradient (Figure 5.1). In a local Cartesian coordinate system, the equations of motion of the ocean fluid assuming geostrophic balance and hydrostatic equilibrium (i.e. motion of a steady uniform flow) are:

$$x - f y = - \frac{1}{\rho} \frac{\partial p}{\partial x} \quad (5.1)$$

$$y + f x = - \frac{1}{\rho} \frac{\partial p}{\partial y} \quad (5.2)$$

$$\frac{\partial p}{\partial z} = - g \rho \quad (5.3)$$

were  $x, y$  are directions of east and north,  $z$  is positive upward,  $\ddot{x}, \ddot{y}, \dot{x}, \dot{y}$  are the accelerations and velocities in the  $x, y$  directions,  $\rho$  is the water density,  $g$  is the gravitational acceleration,  $p$  is the pressure.  $f$  is the Coriolis parameter which is related to the rotation rate of the earth,  $f = 2 \Omega \sin \varphi$ , where  $\Omega$  is the rotation rate in radians per second and  $\varphi$  is the latitude. Under the assumptions of a non-accelerating system (i.e.  $\ddot{x} = \ddot{y} = 0$ ), Eqs. (5.1)-(5.3) became:

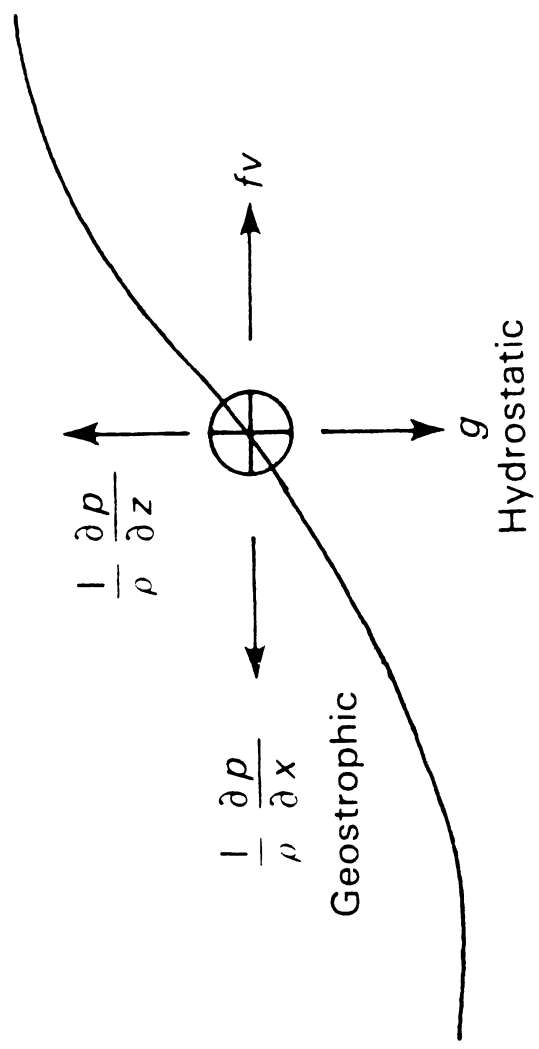


Figure 5.1 Force Balance for ocean current (from Calman, 1987)

$$f x = - \frac{1}{\rho} \frac{\partial p}{\partial y} \quad (5.4)$$

$$f y = \frac{1}{\rho} \frac{\partial p}{\partial x} \quad (5.5)$$

$$\frac{\partial p}{\partial z} = - g \rho \quad (5.6)$$

The vertical hydrostatic equation, Eq. (5.6), states that pressure changes are simply due to the weight of the water above. Thus, pressure changes in the vertical are independent of water motion. The forces are quite different in the horizontal direction. For equilibrium, the Coriolis acceleration is balanced by the horizontal pressure gradient (Figure 5.1). The balance of these forces are only approximate, so that the steady state is never actually realized. The neglected terms in the fluid dynamical equations of motion (e.g. inertial effects, forcing, turbulent dissipation, etc.) cause a complex spatial and temporal evolution of all large-scale ocean phenomena [Calman, 1987].

The desired connection between currents and surface topography is obtained by eliminating the pressure between Eqs. (5.4), (5.5) and (5.6) and integrating vertically from an arbitrary reference level,  $z_r$ , to get

$$v - v_r = \frac{g}{\rho f} \int_{z_r}^z \frac{\partial \rho}{\partial z} dz \quad (5.7)$$

where  $v_r$  is the velocity at the reference level and  $v$  is the velocity at  $z$ . If the density distribution is known between the two levels, the relative velocity can be obtained from Eq. (5.7). Horizontal constant-density surfaces (where the pressure gradients are zero) have no currents.

Historically, the density structure needed for Eq. (5.7) was measured by lowering instrumentation from ships to take the temperature and salinity, from which density could be inferred. Assumptions are required in order to compute the velocity  $v$ , i.e. a reference level,  $z_r$ , and the integration constant,  $v_r$ . The commonly used hypothesis is to choose a reference level with zero velocity assuming that nothing much happens deep in the ocean at a standard depth (e.g. 1500 or 2000 m). Wunch and Gaposchkin [1980] have shown, however, that this so-called 'level of no motion' is a generally poor assumption; the depth of the contours of zero velocity can vary greatly, and the contours can even intersect the surface and the bottom of the ocean many times on scales of interest.

Satellite altimetry becomes very important at this point. Instead of having to use an assumption about the velocity at depth or taking measurements deep into the ocean, the reference level can be chosen to be the marine geoid or a long-term averaged sea surface. No assumption is necessary about the surface velocity because it is related to the surface elevation through the geostrophic and hydrostatic equations by:

$$v_s = \frac{g}{f} \frac{\partial \eta}{\partial x} \quad (5.8)$$

where  $v_s$  is the surface velocity and  $\eta$ , which is measured directly by satellite

altimetry, is the elevation of the ocean surface with respect to the reference level. For the study of eddy kinetic energy, the observed changes in sea surface height along satellite ground tracks are sufficient to obtain useful information. If the effects of the tides, atmospheric pressure, and wave height are eliminated from the altimeter measurement, the dynamic topography,  $\eta$  is composed of two principal geostrophic components: (1) a large-scale component associated with the quasi-stationary mean circulation, which can be considered time-invariant for the time scale under consideration and (2) a mesoscale component associated with the eddy circulation, which is time-varying and appears at the surface as sea height changes or eddy dynamic heights [Menard, 1983]. To be consistent with the eddy height, the sea surface slope changes are referred to as the eddy slope.

If altimeter passes are collinear, like the case of Geosat/ERM, the eddy slope

$\Delta \frac{\partial \eta^i}{\partial x}$  can be expressed for each repeated measurement  $i$  as follows:

$$\Delta \frac{\partial \eta^i}{\partial x} = \frac{\partial \eta^i}{\partial x} - \frac{\partial \eta}{\partial x_m} \quad (5.9)$$

in which  $\frac{\partial \eta^i}{\partial x}$  is the sea surface slope of repeat cycle  $i$ , and  $\frac{\partial \eta}{\partial x_m}$  is the average of repeated slope profiles. The time-independent effects of the gravity field and mean circulation in the right hand side of Eq. (5.9) are thus eliminated. Then the sea surface slope variance  $\sigma_s^2$  is defined by:



$$\sigma_s^2 = \frac{\sum_{i=1}^n \left( \Delta \frac{\partial \eta^i}{\partial x} \right)^2}{n} \quad (5.10)$$

where  $n$  being the number of repeated observations.

Similarly, if we consider the geostrophic current surface velocity, we have

$$V = \bar{V} + \Delta V \quad (5.11)$$

where  $\bar{V}$  is the mean velocity and  $\Delta V$  is the deviation from the mean associated with the eddy flow, which by analogy is called eddy velocity. This eddy velocity  $\Delta V$  can be determined in the satellite cross-track direction  $y$ , from the eddy slope  $\Delta \frac{\partial \eta^i}{\partial x}$  in the along-track direction  $x$  for profile  $i$ . The geostrophic relation gives:

$$\Delta V_y^i = \frac{g}{f} \Delta \frac{\partial \eta^i}{\partial x} \quad (5.12)$$

where  $\Delta V_y^i$  is the eddy velocity in the cross-track direction,  $g$  is the gravitational acceleration, and  $f$  is the Coriolis parameter.

The velocity variance  $\sigma^2(V_y)$  in the same direction  $y$  is defined by:

$$\sigma^2(V_y) = \frac{\sum_{i=1}^n (\Delta V_y^i)^2}{n} \quad (5.13)$$

The eddy kinetic energy is the average of eddy velocity variance in both alongtrack and crosstrack directions:

$$E_e = \frac{1}{2} [\sigma^2(V_x) + \sigma^2(V_y)] \quad (5.14)$$

In order to compute the surface eddy kinetic energy, the velocities in both directions  $x$  and  $y$  must be known. The analysis of altimeter data only gives the velocity variance in the crosstrack direction (except at the crossover points, where both components are determined). Thus to obtain an estimate of the eddy kinetic energy (Eq. 4.33), we assume that the velocity variance is isotropic, i.e.,

$$\sigma^2(V_x) = \sigma^2(V_y) = \sigma_v^2 \quad (5.15)$$

where the  $\sigma_v^2$  is the total velocity variance. Then we have:

$$E_e = \sigma_v^2 \quad (5.16)$$

### 5.3 Eddy Kinetic Energy for the Northwest Atlantic and Northwest Pacific

The computation of the eddy kinetic energy is fairly straightforward. The cross-track eddy velocity variance,  $\sigma^2(V_y)$ , is calculated at each along-track point, where the eddy slope variance is available from the computation of slope rms variability described in Chapter 4, by introducing the geostrophic relation. Where  $x$  represents the

alongtrack direction and  $y$  represents the crosstrack direction. It is reasonable to assume that the eddy field is isotropic which enables the eddy kinetic energy to be computed from the alongtrack profiles. The possible exception to isotropy is the Gulf Stream where the principal axes of variance is sometimes parallel to the Stream's direction of flow. But even there isotropy is still a reasonable assumption [Douglas et al., 1983]. The eddy velocity variances are then averaged into 1 degree by 1 degree squares. These values were contoured to produce maps of eddy kinetic energy for Northwest Atlantic and Northwest Pacific.

As expected, eddy kinetic energy and sea surface slope variability have basically the same distribution in both regions of Northwest Atlantic and Northwest Pacific. In the Northwest Atlantic (Figure 5.2), the Gulf Stream is delineated by eddy kinetic energy values greater than  $500 \text{ cm}^2/\text{s}^2$ , with isolated peaks of  $1500 - 2000 \text{ cm}^2/\text{s}^2$  occurring between  $290^\circ$  and  $320^\circ$  in longitude. Eddy kinetic energy abruptly drops to below  $500 \text{ cm}^2/\text{s}^2$  north of the Gulf Stream at the shelf break, which also coincides with the northern limit of the warm ring region. Values of the  $500 \text{ cm}^2/\text{s}^2$  contour terminate at the  $30^\circ\text{N}$ , cold rings are not normally found below this latitude. On the map of Northwest Pacific (Figure 5.3), high kinetic energy values ( $> 500 \text{ cm}^2/\text{s}^2$ ), corresponding to the meandering of the current front, are associated with the Kuroshio Current and especially between the the Kuroshio front and the Oyashio front ( $35^\circ - 40^\circ$  in latitude,  $140^\circ - 155^\circ$  in longitude), which is a confluence zone where eddy activity is high.

#### 5.4 Comparisons With Geos-3, Seasat and Shipboard Results

Using only pairs of tracks lying within a few kilometers of each other, Douglas et al. [1983] computed the mesoscale variability and eddy kinetic energy in the Northwest Atlantic. Their eddy kinetic energy result is shown in Figure 5.4. They made detailed comparisons with measurements made by expendable bathythermographs (XBT's) and surface drifters respectively and found close qualitative agreement in most of the main features. However, the shipboard results (Figure 5.5 and 5.6) showed systematically higher values than did the altimetric results in the Gulf Stream area south of Cape Hatteras along the coast. Their explanation was that the eddy energy based on shipboard measurements was computed as the standard deviation in a finite gridded area and hence was seriously contaminated by the high spatial geoid variability near the Gulf Stream area, whereas the altimetric measurement sampled only the temporal variability. Therefore the maps derived from satellite altimeter data shown in Figures 5.2, 5.3 and 5.4 are more accurate than the shipboard results. The Geos-3 results from this analysis in the Northwest Atlantic (Figure 5.2) are in excellent agreement with Geos-3 altimeter data analysis with regard to magnitude and spatial distribution. The wider  $500 \text{ cm}^2/\text{s}^2$  contour shape in Geos-3 map is caused by the edge effects of the "bias and tilt" orbit error adjustment technique employed in the Geos-3 data analysis as discussed in Chapter 4.

Menard [1983] used the Seasat repeat track altimeter data to compute the eddy kinetic energy in the regions of Northwest Atlantic and Northwest Pacific. His results are shown in Figures 5.7a and 5.7b. In his maps, high energy is principally located near the current fronts and in the regions of return flow. Since the Seasat data are restrictive in time (25 days) and in spatial (700 km cross-track spacing at mid-latitude),

his maps are not directly comparable to the maps derived from long term Geos-3 [Douglas, 1983] and Geosat/ERM altimeter data as well as shipboard measurements [Wyrтки et al., 1976]. But general qualitative agreements with the above maps can be concluded.

### **5.5 Summary**

The two analyses presented in this Chapter for the Northwest Atlantic and the Northwest Pacific demonstrate the ability of the radar altimeter to map the eddy field in terms of eddy slope variability, eddy velocity, or eddy kinetic energy. Eddy kinetic energy maps derived from Geosat/ERM for Northwest Atlantic and Northwest Pacific are quite similar in general to those previous altimeter results. Especially, excellent agreement between this analysis and the Geos-3 results for the Gulf Stream proved that the altimeter data analysis can provide a fundamental improvement compared to the previous determinations of eddy activity from historical shipboard measurements.

# Eddy Kinetic Energy, Northwest Pacific

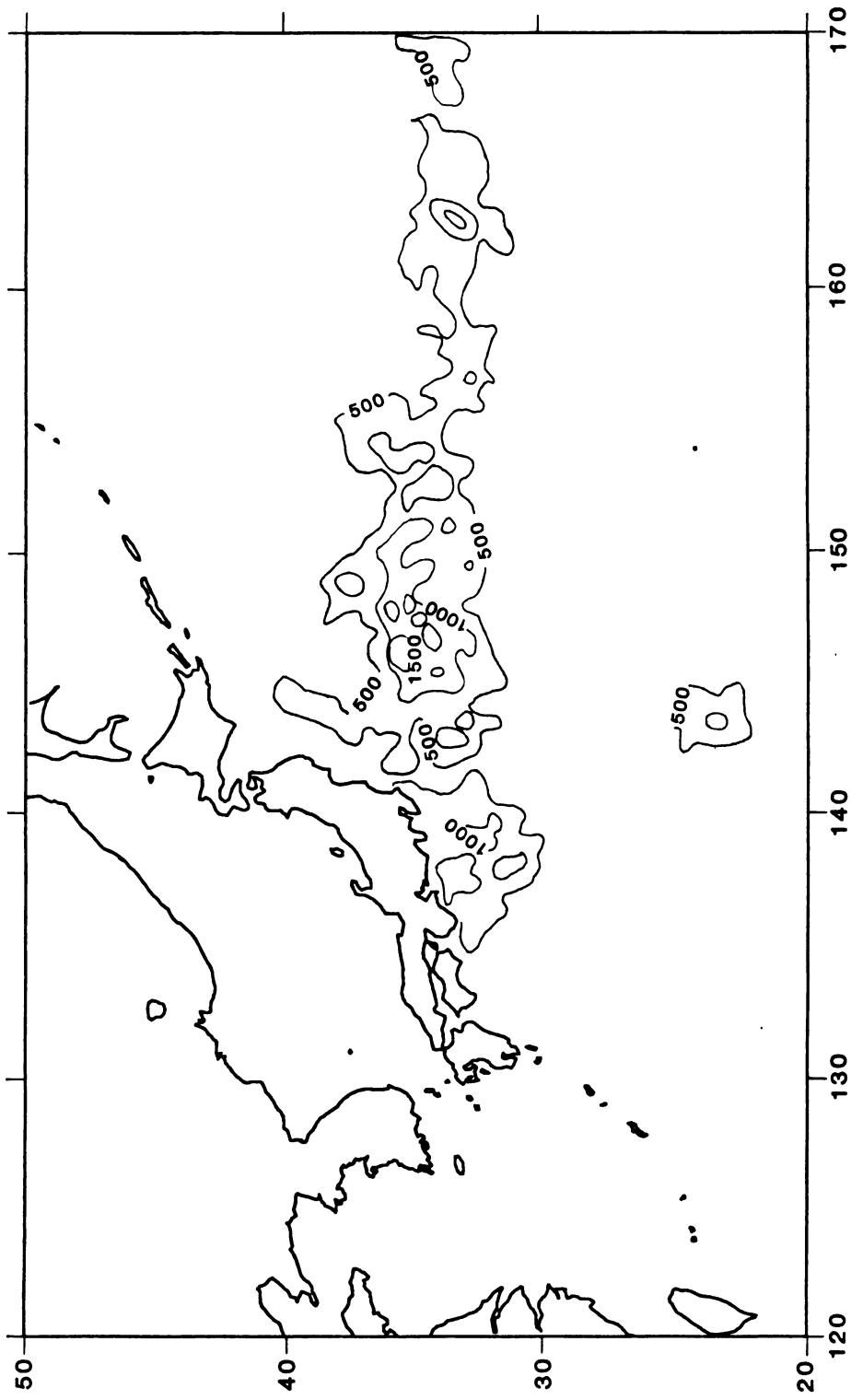


Figure 5.2 Eddy kinetic energy (cm<sup>2</sup>/s<sup>2</sup>) from Geosat, Northwest Atlantic

# Eddy Kinetic Energy, Northwest Atlantic

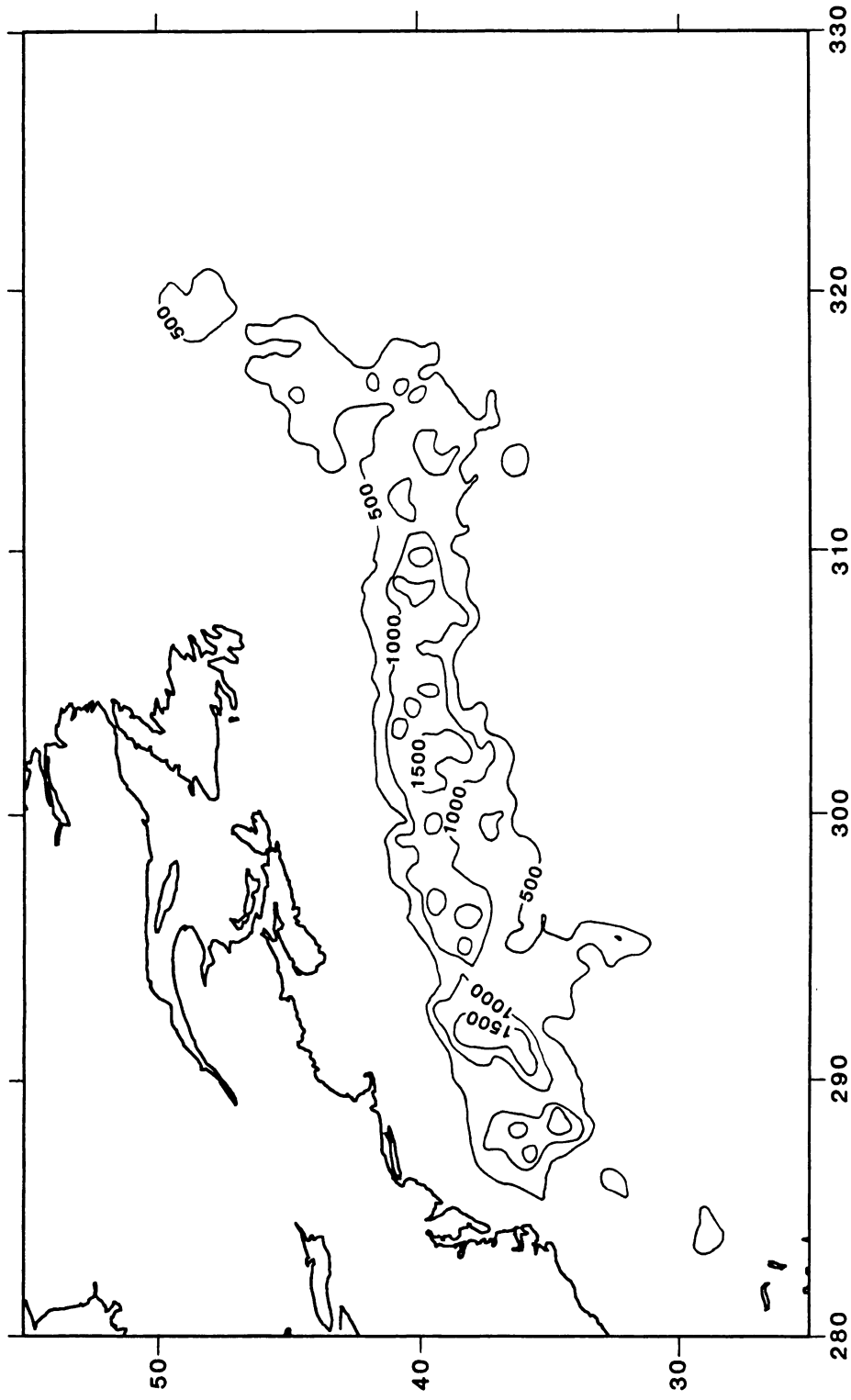


Figure 5.3 Eddy kinetic energy (cm<sup>2</sup>/s<sup>2</sup>) from Geosat, Northwest Pacific

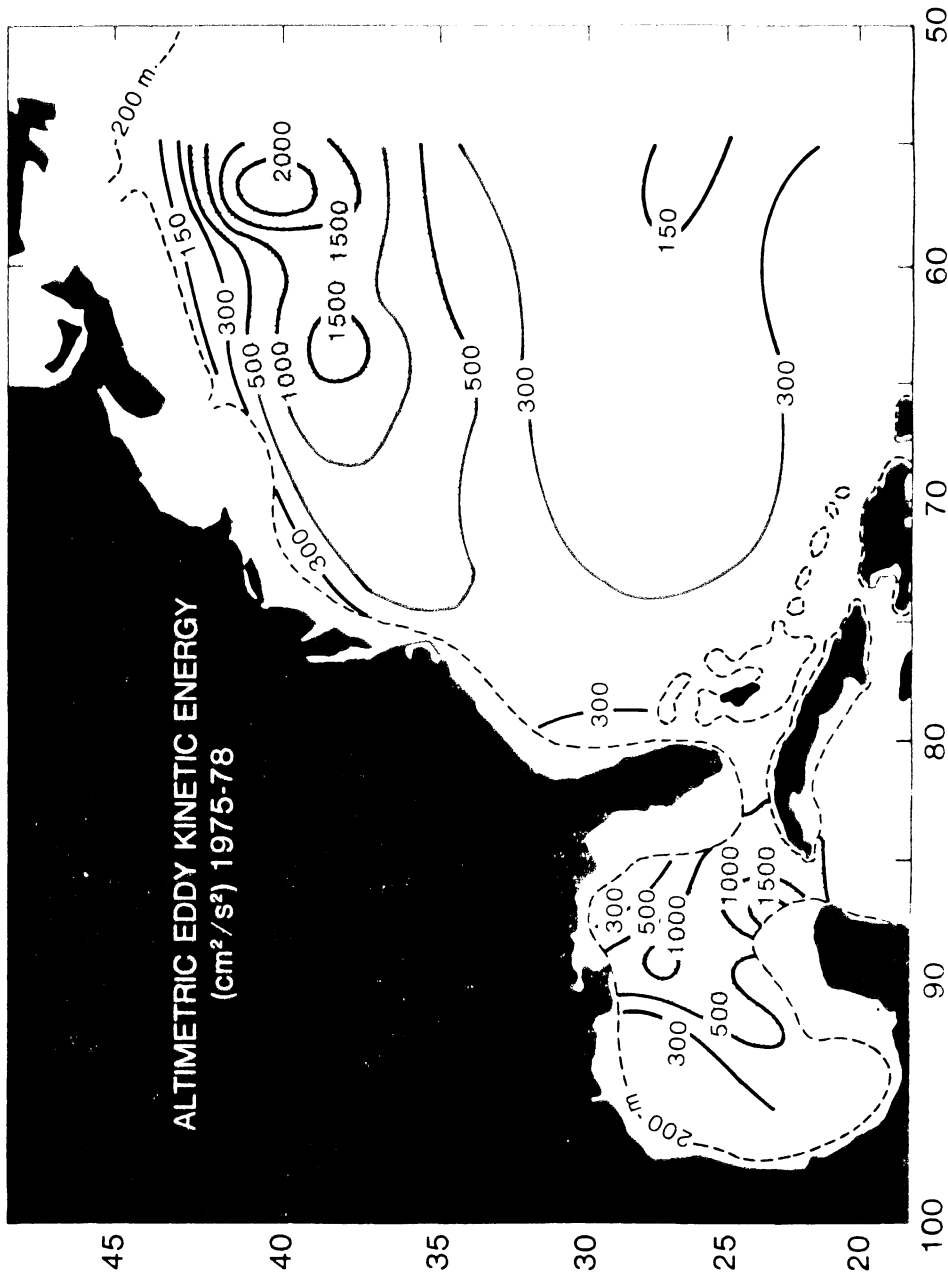


Figure 5.4 Eddy kinetic energy from Geos-3, Northwest Atlantic [Douglas, 1983]



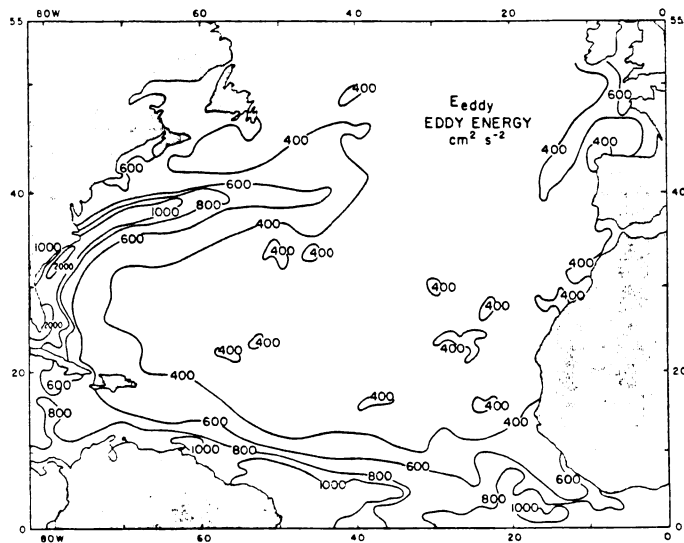


Figure 5.5 Ship drift-derived eddy kinetic energy [Wyrki, 1976]

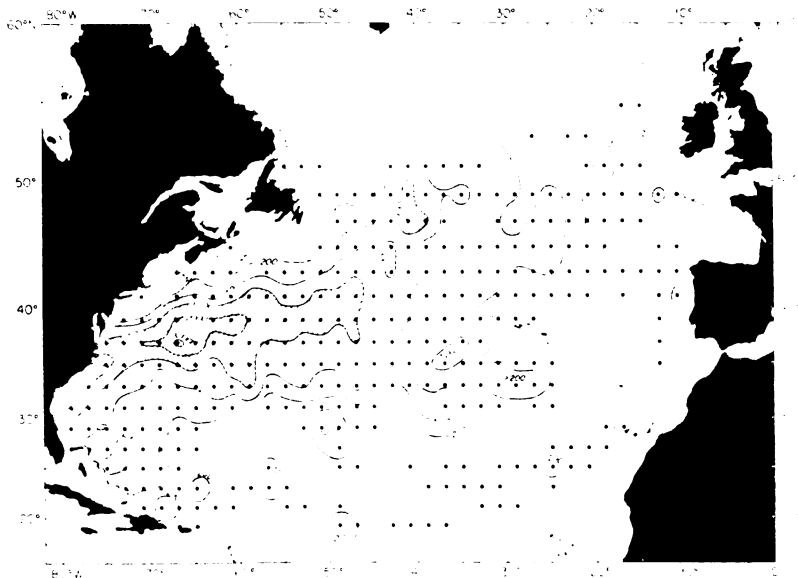


Figure 5.6 Eddy kinetic energy based on surface drifter velocities [Richardson, 1983]

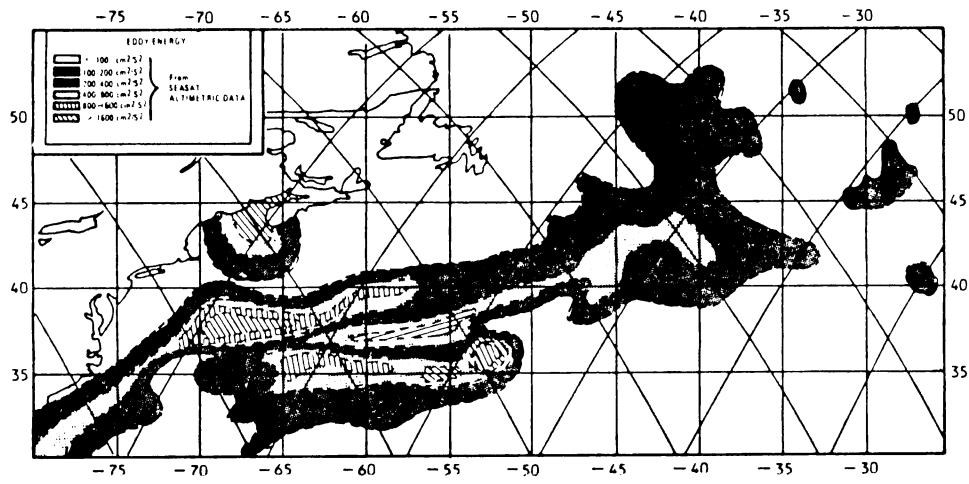


Figure 5.7a Eddy kinetic energy from Seasat, Northwest Atlantic [Menard, 1983]

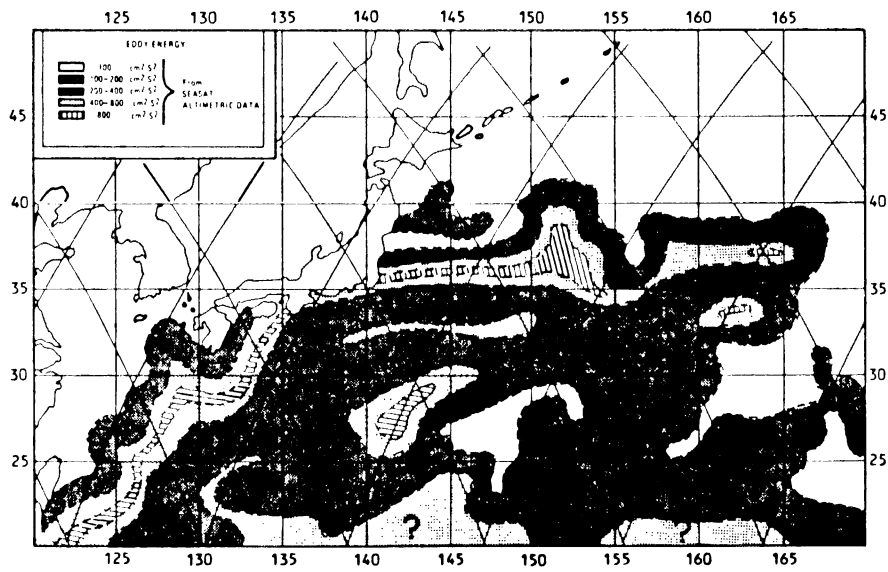


Figure 5.7b Eddy kinetic energy from Seasat, Northwest Pacific [Menard, 1983]

## Chapter 6

### Conclusions

An efficient and generalized single and dual satellite crossovers computation software system has been developed. Analytical theory and numerical experiments showed that the zonal geopotential coefficients which are unobservable using single satellite crossovers are sensitive to the dual satellite crossovers. The inclusion of Seasat crossover measurements has contributed significantly to the accuracy of the Earth's gravity field.

The large radial orbit error ( $\sim 4$  m crossover rms residuals) provided with the Geosat ERM GDR's limits the use of these data for large scale ocean circulation studies. This large radial orbit error is basically long-wavelength with the largest amplitude at frequency of one cycle per orbital revolution. The smaller relative radial orbit error (1 - 3 m) among the collinear altimeter profiles is primarily due to the gravity field mismodeling. In previous studies the tilt and bias method has been used to reduce the the long wavelength orbit error to extract mesoscale (100 - 1000 km) variations in dynamic topography. However large edge effects can occur near the ends of profiles where variability is high. Artificially high variability produced by the tilt and bias technique on the shallow continental shelves between the end of the profiles and the zone of high variability has been interpreted as tide model error or true variability. A simple derivative high-pass filter method has been developed in this investigation in order to suppress the long wavelength radial orbit error without producing edge artifacts. By subtracting the average profile, the differenced collinear slope profiles

were low-pass filtered to reduce the short wavelength ( $< 150$  km) altimeter noise. No geometric adjustments of the profiles are necessary. A spectral analysis of the repeat slope profiles reveals that the largest radial orbit error has an amplitude of  $0.14 \mu\text{rad}$  at wavelength of 40,000 km (once per orbital revolution). Since the mesoscale slope variability is almost always greater than  $0.2 \mu\text{rad}$ , the simple differentiation procedure effectively suppresses the orbit error below the variability signal level.

The global rms slope variability map shows many previously unknown spatial details that are highly correlated with sea floor topography. At mid to high latitudes, areas of higher variability occur in deep water ( $> 3000$  m) adjacent to continental shelves, spreading ridges and oceanic plateaus. Variability is generally low in shallow areas ( $< 2000$  m). Along the ACC, the mesoscale variability is organized by the many shallow areas in its depth. However, over most areas, the rms variability is less than  $1 \mu\text{rad}$ .

The high correlation of mesoscale variability and the ocean depth indicates that the major western boundary currents and the ACC have large barotropic components. At high latitudes where there is little change in sea water density with depth, the major currents can extend to the sea floor. Thus a correlation of mesoscale variability and ocean depth is expected. One of the reasons that the deeper oceans associated with western boundary currents show more variability is possibly because the wind-driven momentum is not damped by the bottom friction as seriously as in the shallower areas.

Eddy kinetic energy maps of the Northwest Atlantic and Northwest Pacific have been constructed and showed good agreements with previously published altimeter results. The similarity between the recent altimeter derived eddy kinetic energy maps and the results based on historical shipboard measurements in terms of the magnitude

and spatial distribution may suggest that the eddy activity is preponderant and that it is concentrated with local areas where ocean circulation is strong [Menard, 1983].

## Appendix

### Derivative Filter and Gaussian Filter

#### Derivative High-Pass Filter:

The derivative of the sea surface topography is referred as the slope profile and is expressed as the following:

$$h'(x) = \frac{dh(x)}{dx} \quad (\text{A1})$$

In the Geosat altimeter data processing, the approximation to the alongtrack derivative of the sea surface topography,  $h'(x)$ , is computed numerically by:

$$h'(x_i) = \frac{h(x_i) - h(x_{i-1})}{x_i - x_{i-1}} \quad (\text{A2})$$

One microradian ( $1 \mu\text{rad}$ ) of slope corresponds to a one meter ocean surface elevation change over 1000 km in distance.

The Fourier transform of slope is given by:

$$F[h'(x)] = j(2\pi k)F[h(x)] \quad (\text{A3})$$

where  $j$  is the imaginary factor and  $k$  is the wave number which is the reciprocal of wavelength:

$$k = 1/\lambda \quad (\text{A4})$$

The transfer function of the derivative filter (Figure A.1) is given by:

$$D(k) = j(2\pi k) \quad (\text{A5})$$

#### Gaussian Low-Pass Filter:

The Gaussian function is given by:

$$g(x) = \frac{1}{\sqrt{2\pi}\sigma} e^{-\frac{x^2}{2\sigma^2}} \quad (\text{A6})$$

and its Fourier transform is:

$$G(k) = F[f(x)] = \int_{-\infty}^{\infty} f(x) e^{-j2\pi kx} dx = e^{-2\pi^2\sigma^2 k^2} \quad (\text{A7})$$

This function has been plotted in Figure A.2 with the Gaussian parameter  $\sigma = 33.15$  km. The foot print of a near earth satellite with a circular orbit (e.g. Geosat) travels at a velocity of 6.63 km/sec. That is one second of the Gaussian parameter  $\sigma$ , in the time domain, corresponds to 6.63 km in the spatial domain.

The half amplitude cutoff wavelength of a Gaussian low-pass filter is defined by the following condition:

$$|G(k)| = \frac{1}{2} \quad (\text{A8})$$

From Eqs. (A4), (A7) and (A8), we have:

$$\lambda = 5.336\sigma \quad (\text{A9})$$

Band-pass filter:

For the analysis of Geosat altimeter data, we first high-pass filtered the data by a derivative filter and then low-pass filtered the data by a Gaussian filter with 175 km half amplitude cutoff wavelength. These filtering procedures can be expressed in the spatial domain as following:

$$h'(x_0) = \frac{\int_{-\infty}^{\infty} h'(x) e^{-\frac{(x-x_0)^2}{2\sigma^2}} dx}{\int_{-\infty}^{\infty} e^{-\frac{(x-x_0)^2}{2\sigma^2}} dx} \quad (\text{A10})$$

In practice, the integral bounds in Eq. (A10) are limited by finite length, e.g.  $3\sigma$  to  $5\sigma$ . In the wavenumber domain, the total filter transfer function is the product of the derivative filter transfer function and the Gaussian filter transfer function:

$$T(k) = j (2 \pi k) e^{-2\pi^2 \sigma^2 k^2} \quad (\text{A11})$$

This function has been plotted in Figure A.3.



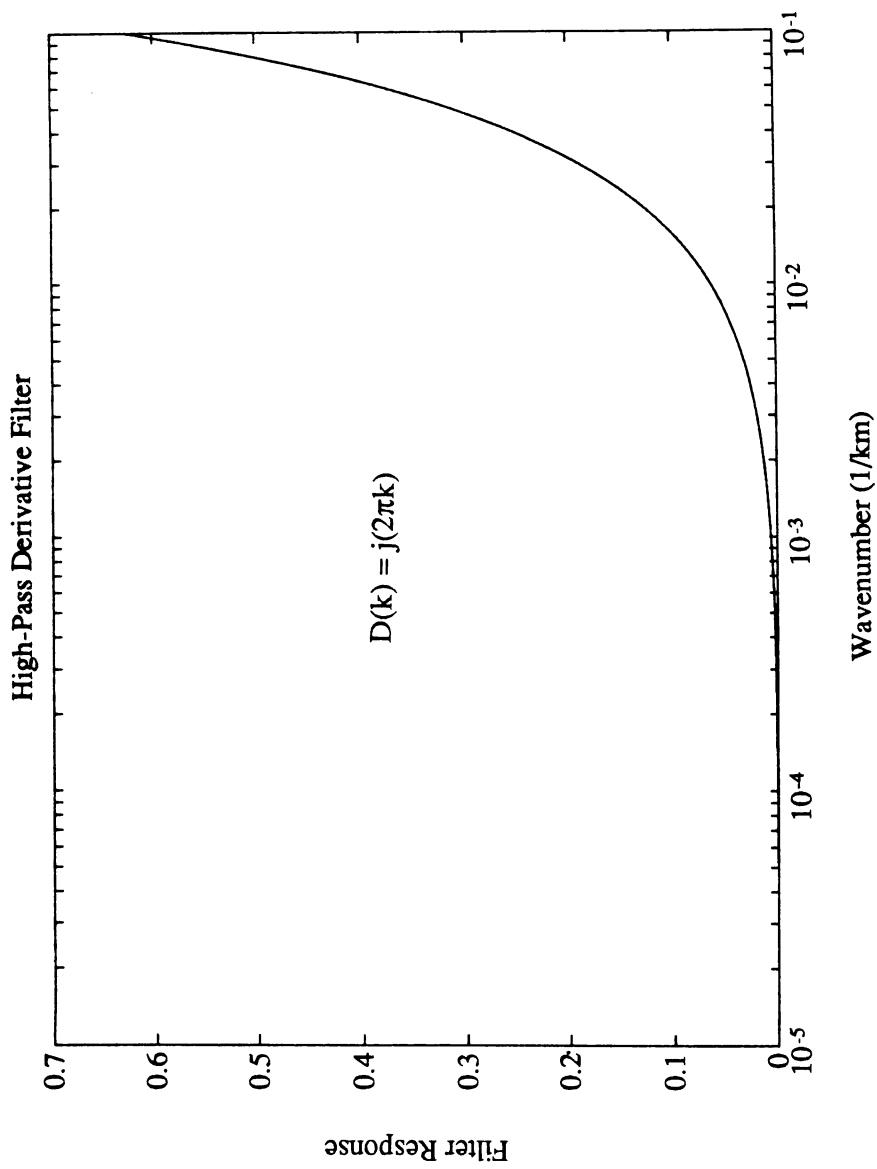


Figure A.1 Transfer function of high-pass derivative filter

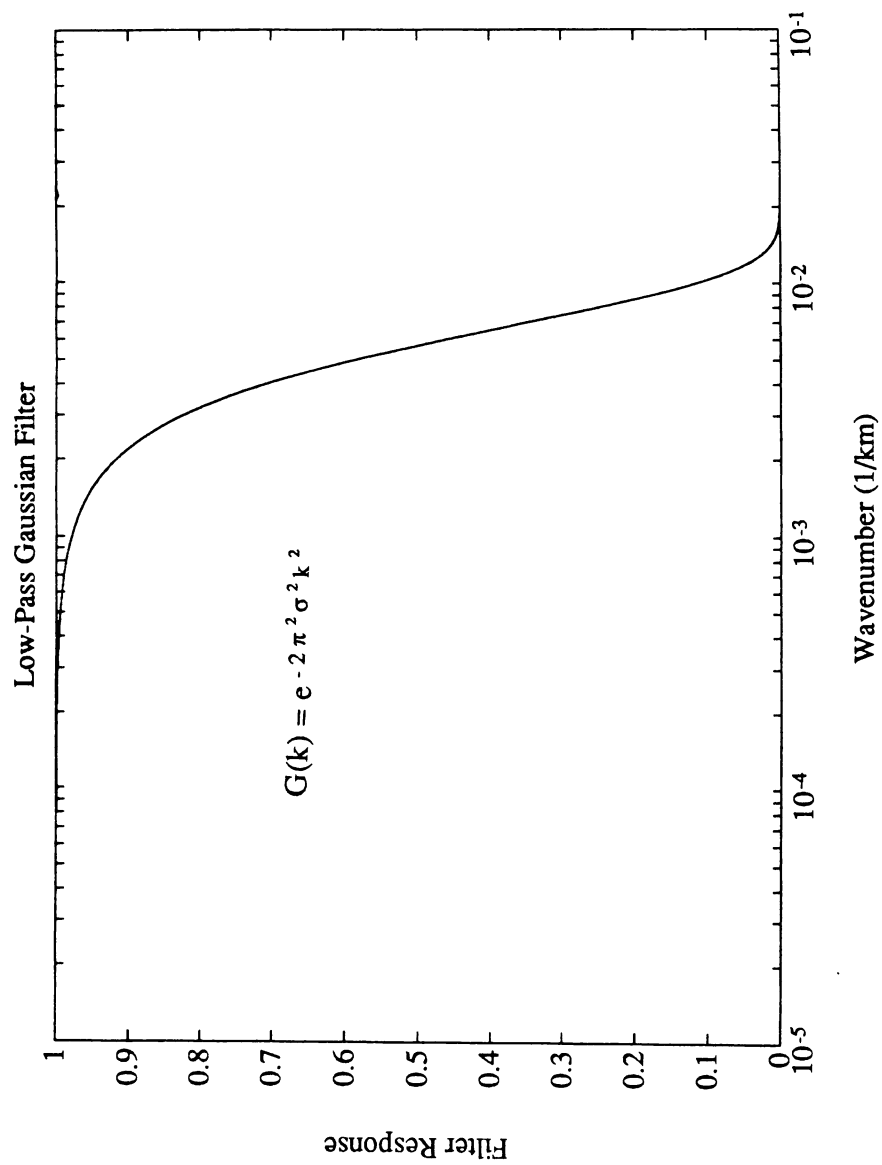


Figure A.2 Transfer function of low-pass Gaussian filter

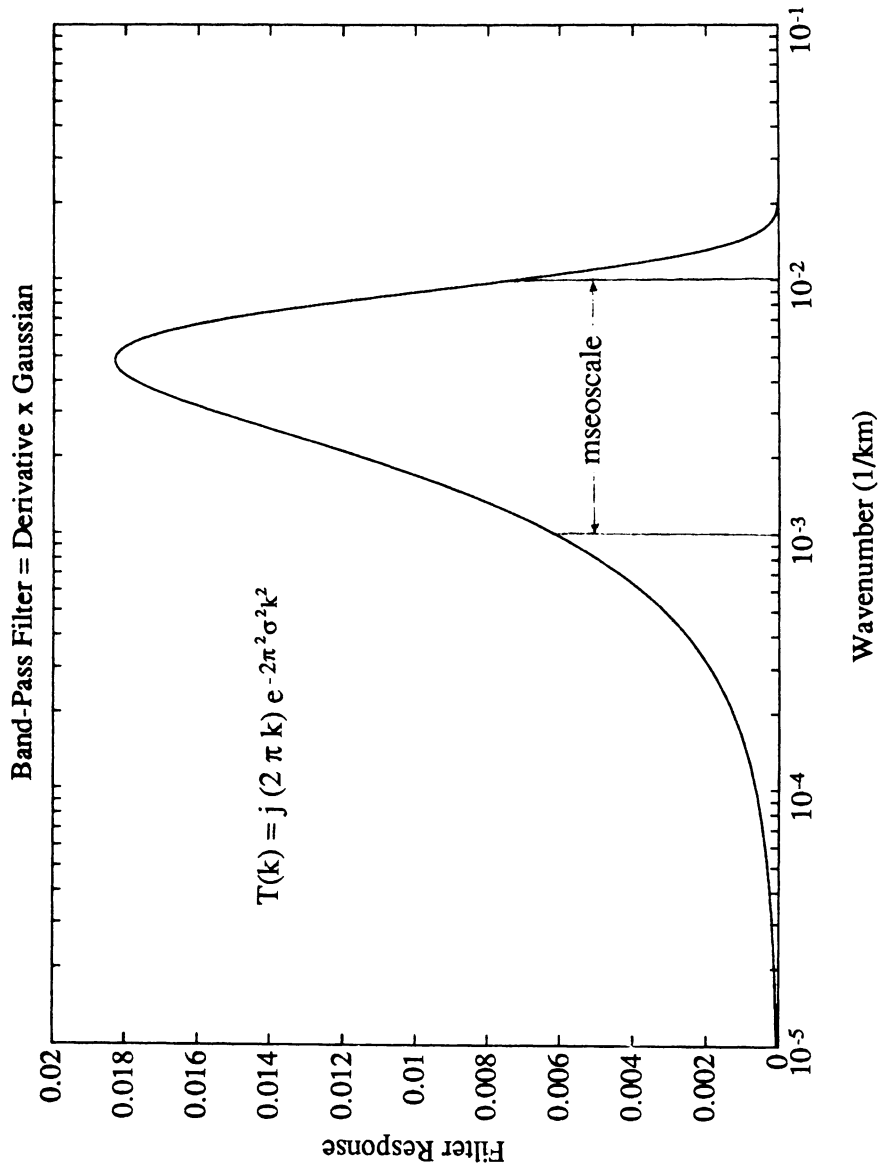


Figure A.3 Transfer function of band-pass filter

## Bibliography

- Born, G.H., D.B. Lame and J.L. Mitchell, A survey of Oceanographic Satellite Altimetric Missions, *Marine Geosedy*, Vol. 8, No. 1-4, 3-16, 1984a
- Born, G.H., C. Wunch, and C.A. Yamarone, TOPEX: Observing the Oceans From Space, *Eos Trans. AGU*, Vol. 65, No. 28, 433-434, July 10, 1984
- Born, G.H., B.D. Tapley, M.L. Santee, Orbit Determination Using Dual Crossing Arc Altimetry, *AAS/AIAA Astrodynamics Conference*, Vail, Colorado, August 12-15, 1985
- Born, G.H., F.G. Lemoine, and M.J. Crawford, Geosat ERM - Orbit Determination, *AAS/AIAA Astrodynamics Conference*, Kalispell, Montana, August 10-13, 1987
- Brown, R.D.,  $M_2$  Ocean Tide at Cobb Seamount from Seasat Altimeter Data, *J. Geophys. Res.*, Vol. 88, No. C3, 1637-1646, February 1983
- Calman, J., Introduction to Sea-Surface Topography From Satellite altimetry, *Johns Hopkins APL Technical Digest*, Vol. 8, No. 2, 1987
- Cheney, R.E., and J.G. Marsh, Oceanic Eddy Variability Measured by Geos-3 Altimeter Crossover Differences, *Eos Trans. AGU*, Vol. 62, No.45, 743-752, 1981a
- Cheney, R.E., and J.G. Marsh, Seasat Altimeter Observations of Dynamic Topography in the Gulf Stream Region, *J. Geophys. Res.*, Vol. 86, 473-483, 1981b
- Cheney, R.E., J.G. Marsh, and B.D. Beckley, Global Mesoscale Variability From

- Collinear Tracks of Seasat Altimeter Data, *J. Geophys. Res.*, Vol.88, No.C7, 4343-4354, May 20, 1983
- Cheney, R.E., B.C. Douglas, R.W. Agreen, L.L. Miller, D.L. Porter, and N.S. Doyle, Geosat Altimeter Geophysical Data Record User Handbook, *Technical Memorandum NOS NGS - 46*, 1987a
- Cheney, R.E., L. Miller, B.C. Douglas and R.W. Agreen, Monitoring Equatorial Pacific Sea Level with Geosat, *Johns Hopkins APL Technical Digest*, 1987b
- Cheney, R.E., B.C. Douglas, and L.L. Miller, Evaluation of Geosat Altimeter Data with Application to the Tropical Pacific Sea Level Variability, *J. Geophys. Res.*, in press, 1988
- Colton, M.T., and R.R.P. Chase, Interaction of the Antarctic Circumpolar Current with Bottom Topography: An Investigation Using Satellite Altimetry, *J. Geophys. Res.*, 88, 1825-1843, 1983
- Douglas, B.C., and P.D. Gaborski, Observations of Sea Surface Topography with Geos-3 Altimeter Data, *J. Geophys. Res.*, 84, 3893-3896, 1979
- Douglas, B.C., R.E. Cheney, and R.W. Agreen, Eddy Energy of the Northwest Atlantic and Gulf of Mexico Determined From GEOS 3 Altimetry, *J. Geophys. Res.*, Vol. 88, No. C14, 9595-9603, Nov. 1983
- Douglas, B.C., R.W. Agreen, and D.T. Sandwell, Observing Ocean Circulation with Seasat Altimeter Data, *Mar. Geod.*, 8, 67-83, 1984
- Douglas, B.C., D.T. McAdoo, and R.E. Cheney, Oceanographic and Geophysical Applications of Satellite Altimetry, *Reviews of Geophysics*, Vol. 25, No. 5, 875-880, June 1987
- Engelis, T., Analysis of Sea Surface Topography Using Seasat Altimeter Data,

*Report of OSU, 1983*

- Fu, L.L., Recent Progress in the Applications of Satellite Altimetry to Observing the Mesoscale Variability and General Circulation of the Oceans, *Review of Geophysics and Space Physics*, Vol.21, No.8, 1657-1666, November, 1983a
- Fu, L.L., On the Wave Number Spectrum of Oceanic Mesoscale Variability Observed by the Seasat Altimeter, *J. Geophys. Res.*, Vol. 88, No. C7, 4331-4341, May 20, 1983b
- Fu, L.L., J. Vazquez, and M.E. Parke, Seasonal Variability of the Gulf Stream From Satellite Altimetry, *J. Geophys. Res.*, Vol. 92, No. C1, 749-754, January 1987
- Gentleman, W.M., Least Square Computations By Givens Transformation Without Square Roots, *J. Inst. Math. Appl.* 12, 1973
- Goad, C.C., B.C. Douglas, and R.W. Agreen, On the Use of Satellite Altimeter Data for Radial Ephemeris Improvement, *The Journal of Astronautic Sciences*, Vol.28, No.4, 419-428, Oct.-Dec. 1980
- Hagar, H., and D.H. Boggs, Differential altimetry for Satellite Orbit Determination, presented at AAS/AIAA Astrodynamics Conference, Jackson Hole, Wyoming, September 1977
- IMSL, User's Manual, IMSL Library, Fortran Subroutines for Mathematics and Statistics, *IMSL, Inc.*, Vol. 2, Chapter L, 1984
- Lerch, F. J., S.M. Klosko, R.E. Laubscher, and C.A. Wanger, Gravity Model Improvement Using Geos 3(GEM9 and 10), *J. Geophys. Res.*, Vol.84,

No.B8, July 30, 1979

Lerch, F.J., B.H. Putney, C.A. Wagner, and S.M. Klosko, Goddard Earth Models for Oceanographic Applications (GEM 10B and 10C), *Marine Geodesy*, Vol. 5, No. 2, 145-187, 1981

Lerch, F.J., J.G. March, S.M. Klosko, and R.G. Williamson, Gravity Model Improvement for Seasat, *J. Geophys. Res.*, Vol. 87, No. C5, 3281-3296, April 30, 1982

Lerch, F.J., S.M. Klosko, C.A. Wanger, and G. Patel, On the Accuracy of Recent Goddard Gravity Models, *J. Geophys. Res.*, Vol.90, No.B11, 9312-9334, September 30,1985

MacArthur, J.L., P.C. Marth, and J.G. Wall, The Geosat Radar Altimeter, *Johns Hopkins APL Technical Digest*, Vol. 8, No. 2, 1987

McConathy, D.R., and C.C. Kilgus, The Navy Geosat Mission: An Review, *Johns Hopkins APL Technical Digest*, Vol. 8, No. 2, 1987

Marsh, J.G., R.E. Cheney, T.V. Martin, and J.J. McCarthy, Computation of A Precise Mean Sea Surface In the Eastern North Pacific Using Seasat Altimetry, *Eos Trans. AGU*, Vol. 63, 178-179, 1982

Marsh, J.G., and R.G. Williamson, Seasat Altimeter Timing Bias Estimation, *J. Geophys. Res.*, Vol. 87, No.C5, 3232-3238, April 1982a

Marsh, J.G., T.V. Martin, The Seasat Altimeter Mean Sea Surface Model, *J. Geophys. Res.*, Vol. 87, No. C5, 3269-3280, April, 1982b

Marsh, J.G., A.C. Bremmer, B.D. Beckley, and T.V. Martin, Global Mean Sea Surface Based Upon the Seasat Altimeter Data, *J. Geophys. Res.*, Vol. 91, No. B3, March 10, 1986

- Marsh, J.G. et al., A New Gravitational Model For The Earth From Satellite Tracking Data : GEM-T1, *J. Geophys. Res.*, Vol. 93, No. B6, 6169-6215, 1988
- Menard, Y., Observation of Eddy Fields in the Northwest Atlantic and Northwest Pacific by SEASAT Altimeter Data, *J. Geophys. Res.*, Vol. 88, No. C3, 1853-1866, Feb. 28, 1983
- Mooers, C.N.K., D.E. Barrick, R.E. Cheney, D.B. Lame, J.G. Marsh, The Potential of Satellite-Based Radar Altimeters, *Eos Trans. AGU*, Vol. 65, No.10, Pages 81,86,87, March 6, 1984
- Neumann, G, Ocean Currents, *Elsevier Publishing Co., Amsterdam*, 1968
- Parke, M.E., Detection of Tides on the Patagonian Shelf By the Seasat Radar Altimeter: An Initial Comparison, *Deep Sea Research*, 27, 297-300, 1980
- Rapp, R.H., The Determination of Geoid Undulations and Gravity Anomalies From Seasat Altimeter Data, *J. Geophys. Res.*, Vol.88, No.C3, 1552-1562, Feb. 28, 1983
- Reigber, C., G. Balmino, H. Muller, W. Bosch, B. Moynot, GRIM Gravity Model Improvement Using Lageos(GRIM3-L1), *J. Geophys. Res.*, Vol. 90, No. B11, 9285-9299, September 30, 1985
- Rosborough, G.W., Satellite Orbit Perturbations Due to the Geopotential, *CSR-86-1*, Center for Space Research, The University of Texas at Ausitn, January 1986
- Rummel, R., and R. Rapp, Undulation and Anomaly Estimation Using Geos-3 Altimeter Data Without Precise Satellite Orbits, *Bull., Geod.*, 51 (1), 73-88, 1987



- Sandwell, D.T., D.G. Milbert, and B.C. Douglas, Global Nondynamic Orbit Improvement for Altimetric Satellites, *J. Geophys. Res.*, Vol. 91, 9447-9451, 1986
- Santee, M.L., Orbit Correction Using Dual Satellite Crossing Arc Theory, *CSR-85-4*, Center for Space Research, The University of Texas at Austin, March 1986
- Schutz, B.E., and B.D. Tapley, UTOPIA: University of Texas Orbit Processor, TR 80-1, Center for Space Research, The University of Texas at Austin, 1980
- Schutz, B.E., et al., Orbit and Geodetic Parameter Estimation Using Satellite Altimeter Measurements, AAS/AIAA Astrodynamics Specialist Conference, August, 1981
- Schutz, B.E., B.D. Tapley, and C.K. Shum, Evaluation of the Seasat Altimeter Time Tag Bias, *J. Geophys. Res.*, Vol. 87, No. C5, 3239-3246, April 1982
- Shum, C.K., Altimeter Method for Satellite Geodesy, *CSR-83-2*, Center for Space Research, The University of Texas at Austin, 1983
- Shum, C.K., B.E. Schutz, B.D. Tapley, B.H. Zhang, and R.S. Nerem, Altimeter Crossover Methods for Precision Orbit Determination, *Eos Trans. AGU*, Vol. 67, No. 44, Nov. 1986a
- Shum, C.K., J.C. Ries, and B.D. Tapley, Atmospheric Drag Model for Precision Orbit Determination, *CSR-86-2*, The University of Texas at Austin, Center for Space Research, January, 1986b
- Shum, C.K., B.H. Zhang, B.D. Tapley, and B.E. Schutz, Altimeter Crossover Methods for Precision Orbit Determination, *Proc. AAA/AIAA Astrodynamics*

- Specialist Conference*, Paper AAS 87-407, Kalispell, Montana, August 10-13, 1987
- Smith, J.C., J.C. Ries, C.K. Shum, B.E. Schutz, and B.D. Tapley, Precision Orbit Determination for The Geosat Exact Repeat Mission, *Proceedings of the American Institute of Aeronautics and Astronautics*, in press, 1988
- Stanley, H.R., The Geos-3 Project, *J. Geophys. Res.*, Vol. 84, No. B8, 3779-3783, July 30, 1979
- Stewart, R.H., Methods of Satellite Oceanography, *University of California Press*, Berkeley and Los Angeles, California, 1985
- Stewart, R.H., L.L. Fu, and M. Lefebvre, Science Opportunities from the Topex/Poseidon Mission, *JPL Publication* 86-18, July 15, 1986
- Tai, C.K. , On Determining the Large Scale Ocean Circulation From Satellite Altimetry, *J. Geophys. Res.*, Vol.88, No. C14, 9553-9565, November 20, 1983
- Tai, C.K., and L.L. Fu, On Crossover Adjustment in Satellite Altimetry and Its Oceanographic Implications, *J. Geophys. Res.*, Vol, 91, No. C2, 2549-2554, February 15, 1986
- Tai, C.K., Geosat Crossover Analysis in the Tropical Pacific 1. Constrained Sinusoidal Crossover Adjustment, *J. Geophys. Res.*, *J. Geophys. Res.*, Vol. 93, No. C9, 10621-10629, September 15, 1988
- Tapley, B.D., G.H. Born, and M.E. Parke, The SEASAT Altimeter Data and its Accuracy Assessment, *J. Geophys. Res.*, Vol.87, No. C5, 3179-3188, April 30, 1982a

- Tapley, B.D., J.B. Lundberg, and G.H. Born, The Seasat altimeter Wet Tropospheric Range Correction, *J. Geophys. Res.*, Vol. 87, No. C5, 3213-3220, April 30, 1982b
- Tapley, B.D., B.E. Schutz, and R.J. Eanes, Station coordinates, Baseline, and Earth rotation from Lageos laser ranging: 1976-1984, *J. Geophys. Res.*, Vol. 90, No. B11, 9235-9248, 1985a
- Tapley, B.D., and G.W. Rosborough, Geographically Correlated Orbit Error and Its Effect on Satellite Altimeter Missions, *J. Geophys. Res.*, Vol. 90, No. C6, 11817-11831, November 20, 1985b
- Tapley, B.D. et al., An Improved Model for the Earth's Gravity Field, *Proc. IUGG 19th General Assembly*, Canada, August 1987
- Tapley, B.D., Topex Gravity Field Development: An Overview, Presented at the Ninth Topex Gravity Model Development Meeting, NASA Goddard Space Flight Center, March 9-10, 1988
- Topex Precision Orbit Determination Team, Analysis of Tranet Tracking Data for Topex/Poseidon Precision Orbit Determination, September, 1987
- Torge, W., Geodesy, *Walter de Gruyter & Co.*, Berlin, New York, 1980
- Wunch, C., and E.M. Gaposchkin, On Using Satellite Altimetry to Determine the General Circulation of the Oceans With Applications to Geoid Improvement, *Reviews of geophysics and Space physics*, Vol. 18, No. 4, 725-745, November 1980
- Wyrtki, K., L. Magaard, and J. Hager, Eddy Energy in the Oceans, *J. Geophys. Res.*, Vol. 81, No. 15, 2641-2646, May 20, 1976

## VITA

Bohai Zhang was born in Shandong, China, on December 3, 1948, the son of Jingfu Zhang and Xiaofeng Hu. He graduated from the No.4 High School, Beijing, China, in September, 1966. From 1968 to 1983, he had been working in farms and factories as a worker in Shanxi, China. He entered the Shanxi Insitute of Technology, Taiyuan, Shanxi, China, in September 1973. He received the degree of Bachelor of Science with a major in engineering in October, 1976. During the following years, he was employed as an Assistant Engineer by the No.1 Institute of Civil Engineering of the Ministry of Light Industry of the People's Republic of China, Beijing, China. In November 1978, he was employed as a Research Assistant by the Space Science and Technology Center, Academia Sinica, Beijing, China, and worked there until May, 1983. In January, 1984, he entered The Graduate School of The University of Texas at Austin and was employed as a half time Graduate Research Assistant by the Center for Space Research, The University of Texas at Austin. He married Yaqun Pei in 1979. They have a lovely daughter, Wanlin Zhang, age 6.

Permanent address: #9, Xi Huangchengen Nanjie  
Beijing, People's Republic of China

This dissertation was typed by Bohai Zhang